



**Dulce Isabel Meneses  
Nogueira**

**Flutuações de pressão na camada limite turbulenta  
de uma parede com e sem gradientes de pressão.**

**Turbulent boundary layer wall pressure fluctuations  
with and without pressure gradients.**





**Dulce Isabel Meneses  
Nogueira**

**Flutuações de pressão na camada limite turbulenta  
de uma parede com e sem gradientes de pressão.**

Relatório de Estágio apresentado à Universidade de Aveiro para cumprimento dos requisitos necessários à obtenção do grau Mestre em Engenharia do Ambiente, realizado sob a orientação científica do: Doutor Carlos Borrego, Professor Catedrático do Departamento de Ambiente e Ordenamento e Doutora Vera Rodrigues, Bolseira de Pós-Doutoramento do Departamento de Ambiente e Ordenamento.

Orientação científica e experimental no von Karman Institute for Fluid Dynamics por: Doutor Christophe Schram, Professor Associado no von Karman Institute for Fluid Dynamics; Doutor Nicolas Van de Wyer, Research Engineer no von Karman Institute for Fluid Dynamics.

## **o júri**

Presidente

Prof.<sup>a</sup> Doutora Maria Isabel Aparício Paulo Fernandes Capela  
Professora Associada, Universidade de Aveiro.

Vogal – Arguente Principal

Prof. Doutor António Manuel Gameiro Lopes  
Professor Auxiliar, Departamento de Engenharia Mecânica. Faculdade de Ciências e Tecnologia.  
Universidade de Coimbra.

Vogal - Orientador

Prof. Doutor Carlos Alberto Diogo Soares Borrego  
Professor Catedrático, Universidade de Aveiro.



## **acknowledgments**

During the master degree in Environmental Engineering, I had been in contact with different people, and I need to thank all of you that had contributed for my performance, including all the teachers from University of Aveiro, friends and colleagues.

A specially thank you, to my mother and family that had support me during this 5 years.

To my supervisor and advisor from University of Aveiro, Professor Carlos Borrego and Doctor Vera Rodrigues, for all the support and time they had spent with me. For all the wise advices and teaching.

To my supervisor and advisor from von Karman Institute for Fluid Dynamics, Professor Christophe Schram and Dr. Nicolas Van de Wyer for all the patience, knowledge and time they had gave me.

To the aeroacoustic group at von Karman Institute, for all the knowledge shared during this internship.

To Doctor Lilla Koloszár, from the aeroacoustic group, for all the support, kindness and wisdom shared.

To all the personnel and staff from von Karman Institute, for their kindness.

To Catarina Vilas Boas, for her friendship and support during this 5 years.



## palavras-chave

Camada limite turbulenta, gradientes de pressão favoráveis e adversos, espectros de pressão, anemômetro de fio quente, antena de microfones, PIV.

## resumo

A camada limite turbulenta (CLT) é uma significativa fonte de vibração e ruído em diferentes tipos de estruturas. Estas estruturas podem ser excitadas por flutuações de pressão, devido ao fluxo turbulento induzido pelo seu movimento. A fim de reduzir o ruído irradiado por estas estruturas, é importante entender como é que estas reagem à excitação da CLT. Assim, é necessário estudar esta camada sob diferentes condições de pressão. Uma vez que a CLT exhibe movimentos de fluido aleatórios, é conveniente descrevê-la em termos de espectros de pressão.

O trabalho realizado durante o estágio no von Karman Institute for Fluid Dynamics (VKI), foi integrado no projeto TUMULT (TURbulent flow noise Modelling for Under- and upper-body Load and Transmission analysis).

Um dos objetivos deste estágio, foi a investigação da CLT sob gradientes de pressão nulos, favoráveis e adversos, para duas velocidades de escoamento, 15 e 25 m.s<sup>-1</sup>. Neste sentido, as técnicas experimentais, anemômetro de fio quente e uma antena de microfones foram combinadas, para gerar uma base de dados com a finalidade de proceder à melhoria dos modelos de pressão aplicados a uma parede. Modelos estes que têm em consideração o efeito do número de Reynolds e os efeitos do gradiente de pressão. As técnicas experimentais utilizadas, foram aplicadas no túnel de vento denominado por WAABLIEF ("wind tunnel for aeroacoustics boundary layer including pressure gradient effect"), localizado nas instalações do VKI.

A caracterização da CLT utilizando o anemômetro de fio quente e a determinação dos espectros de pressão sobre uma parede para cada condição em estudo, com posterior validação, utilizando os resultados da antena de microfones, foram realizados com sucesso. Os modelos que foram aplicados para caracterizar os espectros de pressão sobre uma parede foram os modelos de Goody e de Rozenberg. Adicionalmente, também se realizou uma análise de incertezas para o anemômetro de fio quente.

Além dos objetivos diretamente relacionados com o projeto TUMULT, também foi aprendida a técnica experimental Velocimetria por Imagem de Partículas (PIV). Para obter experiência na aplicação desta técnica, foi realizado um estudo paramétrico. Este estudo permitiu determinar qual era a melhor combinação de parâmetros para realizar as medições com PIV. Esta combinação de parâmetros, serviu como suporte para o trabalho de investigação dos estudantes de doutoramento Gian Luca Gori e pós-graduação Simão Nóbrega, do VKI.

Finalmente, neste relatório também se inclui uma revisão bibliográfica sobre a camada limite atmosférica urbana. Esta secção tem como objetivo demonstrar a aplicação que pode ser dada aos conceitos e técnicas aprendidas durante o estágio, ao curso de Engenharia do Ambiente.





**Keywords**

Turbulent boundary layer, adverse and favourable pressure gradients, wall pressure spectrum, hot wire anemometer, microphone antenna, particle image velocimetry (PIV).

**Abstract**

Turbulent Boundary Layers (TBL) are a significant source of vibration and noise for different types of structures. These structures may be excited by pressure fluctuations due to the turbulent flow induced by their motions. To reduce the noise radiated from these structures is important to understand how the structure reacts to the TBL excitation. Therefore, it is necessary to study the TBL under different pressure conditions. TBL exhibit random-like fluid motion, so is convenient to describe it in terms of wall pressure spectrums.

The work performed during this internship at von Karman Institute for Fluid Dynamics (VKI), was integrated under the TUMULT project (TUrbulent flow noise Modelling for Under- and upper-body Load and Transmission analysis).

One of the objective of the internship was the investigation of the TBL under zero, favourable and adverse pressure gradients for two velocities, 15 and 25 m.s<sup>-1</sup>. For that purpose, experimental techniques, such as, hot wire anemometer and microphone antenna, were combined to generate a database allowing to validate and improve wall pressure models accounting for Reynolds number and pressure gradient effects. These experiments had taken place at the “wind tunnel for aeroacoustics boundary layer including pressure gradient effect” (WAABLIEF).

The characterization of the TBL was successfully accomplished using hot wire anemometer, and the wall pressure spectrums for each condition were calculated applying wall pressure models and using a microphone antenna for further validation. The models applied to characterize the wall pressure spectrums were Goody and Rozenberg models. An uncertainty analysis was also performed for hot wire anemometer.

The PIV technique was applied in the framework of this internship, besides the objectives of the TUMULT project. In order to get experience about the application of this technique, a parametric study was successfully accomplished to find out the best configuration for the PIV measurements for the research work of the PhD student Gian Luca Gori and the research master student Simão Nóbrega from VKI.

Finally, in this report it is also included a literature review about the urban atmospheric boundary layer. This section has the objective of demonstrate the type of application of the concepts and techniques learned during the internship to the field of environmental engineering.



## List of contents

LIST OF FIGURES.....	XIV
LIST OF TABLES .....	XV
LIST OF SYMBOLS.....	XVI
<b>SECTION 1 – INTRODUCTION .....</b>	<b>1</b>
SECTION 1.1 – FRAMEWORK AND OBJECTIVES OF THE INTERNSHIP .....	1
SECTION 1.2 – VON KARMAN INSTITUTE FOR FLUID DYNAMICS.....	2
SECTION 1.3 – METHODOLOGY .....	3
SECTION 1.4 – REPORT STRUCTURE.....	5
<b>SECTION 2 – TURBULENT BOUNDARY LAYERS.....</b>	<b>7</b>
SECTION 2.1 – BOUNDARY LAYER CHARACTERIZATION AND SPECTRAL ANALYSIS.....	8
SECTION 2.2 – TBL WALL PRESSURE SPECTRUM .....	12
SECTION 2.3 – WALL PRESSURE MODELS FOR TBL.....	14
<b>SECTION 3 – EXPERIMENTAL TECHNIQUES.....</b>	<b>17</b>
SECTION 3.1 – OVERVIEW OF THE WIND TUNNEL .....	17
SECTION 3.2 – HOT WIRE ANEMOMETER .....	19
<i>Section 3.2.1 - Theoretical background.....</i>	<i>19</i>
<i>Section 3.2.2 – Measurement chain and calibration procedure.....</i>	<i>21</i>
<i>Section 3.2.3 – Measurement of the distance between the hot wire and the bottom wall .....</i>	<i>25</i>
<i>Section 3.2.4 – Measurements procedure.....</i>	<i>26</i>
SECTION 3.3 – WALL PRESSURE MEASUREMENTS .....	29
<i>Section 3.3.1 – Theoretical background .....</i>	<i>29</i>
<i>Section 3.3.2 – Microphone antenna .....</i>	<i>30</i>
<i>Section 3.3.3 – Measurement chain and calibration procedure.....</i>	<i>31</i>
<i>Section 3.3.4 – Measurements procedure.....</i>	<i>33</i>
SECTION 3.4 – PARTICLE IMAGE VELOCIMETRY (PIV) .....	34
<i>Section 3.4.1 – Theoretical background .....</i>	<i>34</i>
<i>Section 3.4.2 – Description of the equipment .....</i>	<i>37</i>
<i>Section 3.4.3 – Measurements procedure.....</i>	<i>39</i>
<b>SECTION 4 – UNCERTAINTY ANALYSIS.....</b>	<b>42</b>
<b>SECTION 5 – RESULTS AND DISCUSSION.....</b>	<b>46</b>
SECTION 5.1 – HOT WIRE ANEMOMETER .....	46
SECTION 5.2 – POWER SPECTRAL DENSITY .....	54
SECTION 5.3 – PARTICLE IMAGE VELOCIMETRY.....	57
<b>SECTION 6 – URBAN ATMOSPHERIC BOUNDARY LAYER.....</b>	<b>62</b>
SECTION 6.1 – ATMOSPHERIC BOUNDARY LAYER .....	62
SECTION 6.2 – URBAN BOUNDARY LAYER.....	66
SECTION 6.3 – OUTDOOR PEDESTRIAN COMFORT .....	69
<b>SECTION 7 – CONCLUSIONS AND RECOMMENDATIONS.....</b>	<b>74</b>
SECTION 7.1 – CONCLUSIONS.....	74
SECTION 7.2 – RECOMMENDATIONS.....	76
<b>REFERENCES.....</b>	<b>77</b>

**APPENDIX I – UNCERTAINTY ANALYSIS RESULTS.....A**

**APPENDIX II – PIV SYSTEM SYNCHRONIZATION .....H**

**APPENDIX III – EFFECT OF TEMPERATURE CORRECTION ..... I**

**List of figures**

**FIGURE 2. 1 - BOUNDARY LAYER DEVELOPMENT OVER A FLAT PLATE (ZAPATA, 2017). ..... 8**

**FIGURE 2. 2 - RESCALE VELOCITY PROFILE OF A TURBULENT BOUNDARY LAYER (ADAPTED FROM ZAPATA, 2017). ..... 10**

**FIGURE 2. 3 - TYPICAL POINTWISE SPECTRUM  $\Phi_{PP}(\omega)$  FOR TBL (ZAPATA, 2018). ..... 13**

**FIGURE 2. 4 - GENERIC STRUCTURE OF TBL WAVENUMBER-FREQUENCY SPECTRA, PLOTTED FOR INCREASING FREQUENCIES FROM LEFT TO RIGHT. THE BLUE REGION CORRESPONDS TO AN ACOUSTIC DIFFUSE FIELD AND THE RED REGION CORRESPONDS TO THE CONVECTIVE RIDGE (SCHRAM AND VAN DE WYER, 2018). ..... 14**

**FIGURE 3. 1 - SCHEMATIC (UP) (ZAPATA, 2017) AND PICTURE (DOWN) OF THE WAABLIEF LOCATED ON THE VKI FACILITIES. . 18**

**FIGURE 3. 2 - PICTURE OF THE SAND ROUGHNESS ON THE ENTRANCE OF THE WAABLIEF (ZAPATA, 2017)..... 18**

**FIGURE 3. 3 - 2D PLAN OF THE WAABLIEF TEST SECTION (ZAPATA, 2017). ..... 19**

**FIGURE 3. 4 - TYPICAL HOT WIRE PROBE GEOMETRY (ANTHOINE ET AL., 2009). ..... 20**

**FIGURE 3. 5 - TYPICAL HOT WIRE MEASUREMENT CHAIN (ZAPATA, 2017). ..... 22**

**FIGURE 3. 6 - PICTURE OF THE OSCILLOSCOPE (UP) AND ANEMOMETER (DOWN) USED IN THE EXPERIMENTS..... 22**

**FIGURE 3. 7 - SCHEMATIC (A) AND PICTURE (B) OF THE HOT WIRE CALIBRATION NOZZLE (ZAPATA, 2017). ..... 23**

**FIGURE 3. 8 - THEODOLITE WILD-N3 (ZAPATA, 2017). ..... 25**

**FIGURE 3. 9 - VIEW IN THE THEODOLITE OPTICS (ZAPATA, 2017). ..... 26**

**FIGURE 3. 10 - WIND TUNNEL TEST SECTION IN PRESENCE OF THE TWO RAMP CONFIGURATIONS, RAMP 1 (TOP) AND RAMP 2 (BOTTOM) RESPECTIVELY (COURTESY OF THE VKI DESIGN OFFICE). ..... 28**

**FIGURE 3. 11 - DETAILED DESIGN OF THE BOTTOM PLATE OF THE WIND TUNNEL TEST SECTION FOR THE MICROPHONE ANTENNA AND HOT WIRE (COURTESY OF THE VKI DESIGN OFFICE). ..... 28**

**FIGURE 3. 12 - INSTALLATION OF THE MICROPHONES IN THE ANTENNA DISK (THE ELECTRET MICROPHONE IS NOT SHOWN BUT IS INSERTED TILL THE END OF THE 2.8 MM CYLINDRICAL CAVITY) (SCHRAM AND VAN DE WYER, 2018). ..... 30**

**FIGURE 3. 13 - SURFACE MAP OF THE LOCATION OF THE 64 MICROPHONES ON THE ANTENNA (ZAPATA, 2017). ..... 31**

**FIGURE 3. 14 - MEASUREMENT CHAIN OF THE WALL PRESSURE MEASUREMENTS (ZAPATA, 2017). ..... 31**

**FIGURE 3. 15 - WALL MICROPHONE CALIBRATOR (A) CAD VIEW (B) PLACED ON TOP OF THE REFERENCE MICROPHONE (VAN DE WYER ET AL., 2018). ..... 32**

**FIGURE 3. 16 - TYPICAL ARRANGEMENT OF A PIV SYSTEM IN A WIND TUNNEL (RAFFEL ET AL., 2007). ..... 36**

**FIGURE 3. 17 - CROSS-CORRELATION MAP OF TWO SINGLE EXPOSURE FRAMES (SCHRAM, 2003). ..... 36**

**FIGURE 3. 18 - DESIGN OF PLIF FACILITY (GORI, 2018). ..... 37**

**FIGURE 3. 19 - TWO POWER SUPPLY FOR THE BLUE LASER SYSTEM TYPE BSL200 CFR300 (ANTAL AND TAGADÓ, 2010). ..... 38**

**FIGURE 3. 20 - MOTIONPRO TIMING HUB SOFTWARE. .... 38**

**FIGURE 4. 1 - UNCERTAINTY ON JET MEAN VELOCITY PROFILE (SCHRAM, 2017). ..... 43**

**FIGURE 4. 2 - VELOCITY PROFILES FOR 15 AND 25 M.S<sup>-1</sup> FOR ZPG AT THE INLET POSITION, INCLUDING THE ESTIMATED UNCERTAINTY. .... 45**

**FIGURE 5. 1 - RESULTS FOR THE PRESSURE TRANSDUCER CALIBRATION. .... 46**

**FIGURE 5. 2 - HOT WIRE ANEMOMETER CALIBRATION RESULTS INCLUDING TEMPERATURE CORRECTION. .... 47**

**FIGURE 5. 3 - RESCALE VELOCITY PROFILES FOR ZPG AT INLET. .... 48**

**FIGURE 5. 4 - RESCALE VELOCITY PROFILES FOR ZPG AT STATION 1 (LEFT) AND AT STATION 2 (RIGHT) FOR 25 M.S<sup>-1</sup>. .... 49**

**FIGURE 5. 5 - RESCALE VELOCITY PROFILES FOR FPG AT STATION 1 FOR 15 AND 25 M.S<sup>-1</sup>. .... 49**

**FIGURE 5. 6 - RESCALE VELOCITY PROFILES FOR STATION 1 (LEFT) AND STATION 2 (RIGHT) WITH RAMP 2 FOR 15 AND 25 M.S<sup>-1</sup>. ..... 50**

**FIGURE 5. 7 - 1/7TH LAW PROFILE FOR 15 AND 25 M.S<sup>-1</sup> UNDER PRESSURE GRADIENTS. .... 51**

<b>FIGURE 5. 8</b> - SPALDING LAW FOR 15 AND 25 M.S <sup>-1</sup> UNDER PRESSURE GRADIENTS. ....	52
<b>FIGURE 5. 9</b> - TURBULENCE INTENSITY (%) FOR 15 AND 25 M.S <sup>-1</sup> UNDER PRESSURE GRADIENTS. ....	52
<b>FIGURE 5. 10</b> - TURBULENCE SPECTRA FOR 15 (LEFT) AND 25 (RIGHT) M.S <sup>-1</sup> UNDER PRESSURE GRADIENTS. ....	53
<b>FIGURE 5. 11</b> - COMPARISON BETWEEN THE GOODY MODEL AND ROZENBERG MODEL. ....	56
<b>FIGURE 5. 12</b> - COMPARISON OF THE RESULTS BETWEEN THE MICROPHONE ANTENNA RESULTS AND THE GOODY MODEL (BLACK) FOR ZPG AT STATION 1 (LEFT) AND STATION 2 (RIGHT) FOR 25 M.S <sup>-1</sup> .....	57
<b>FIGURE 5. 13</b> - DEFINITION OF PEAK RATIO ACCORDING TO DAVIS SOFTWARE MANUAL. ....	58
<b>FIGURE 5. 14</b> - IDENTIFICATION OF THE POINTS FROM THE CALIBRATION PLATE WITH DAVIS. ....	58
<b>FIGURE 5. 15</b> - RESULT FOR THE CALIBRATION PLATE. ....	59
<b>FIGURE 5. 16</b> - IMAGES OF THE PARTICLES CONCENTRATION FOR MEDIUM (LEFT) AND HIGH (RIGHT). ....	61
<b>FIGURE 6. 1</b> - SCHEMATIC REPRESENTATION OF THE TROPOSPHERE DIVISION INTO FREE ATMOSPHERE AND BOUNDARY LAYER (STULL, 1988).....	62
<b>FIGURE 6. 2</b> - WIND FLOW LAYERS IN THE URBAN BOUNDARY LAYER (UBL) (RICCIARDELLI AND POLIMENO, 2006). ....	66
<b>FIGURE 6. 3</b> - SCHEMATIC DIAGRAM OF ROUGHNESS SUBLAYER, INERTIAL SUBLAYER AND CANOPY LAYER. GREY ARROWS INDICATE STREAMLINES AND DASHED LINE INDICATES MEAN BUILDING HEIGHT, H (BARLOW, 2014). ....	68
<b>FIGURE AI. 1</b> - VELOCITY PROFILES FOR 25 M.S <sup>-1</sup> FOR ZPG AT THE STATION 1 AND 2 RESPECTIVELY, INCLUDING THE ESTIMATED UNCERTAINTY. ....	E
<b>FIGURE AI. 2</b> - VELOCITY PROFILES FOR 15 AND 25 M.S <sup>-1</sup> FOR FPG AT STATION 1, INCLUDING THE ESTIMATED UNCERTAINTY. ....	F
<b>FIGURE AI. 3</b> - VELOCITY PROFILES FOR 15 AND 25 M.S <sup>-1</sup> FOR APG AT STATION 2, INCLUDING THE ESTIMATED UNCERTAINTY. ...	G
<b>FIGURE AII. 1</b> - TIMING DIAGRAM FOR THE PIV SYNCHRONIZATION (ANTAL AND TAGADÓ, 2010). ....	H
<b>FIGURE AIII. 1</b> - EFFECT OF THE TEMPERATURE CORRECTION APPLIED TO THE MEASURED DATA WITH HOT WIRE ANEMOMETER. ....	I

## List of tables

<b>TABLE 3. 1</b> - DATA ACQUISITION OF THE HOT WIRE CALIBRATION. ....	23
<b>TABLE 3. 2</b> - SYNTHESIS OF THE MEASUREMENTS PERFORMED WITH HOT WIRE ANEMOMETER.....	27
<b>TABLE 3. 3</b> - SUMMARY OF THE MEASUREMENTS FOR THE MICROPHONE ANTENNA. ....	34
<b>TABLE 3. 4</b> - TECHNICAL DATA OF THE CAMERA (ANTAL AND TAGADÓ, 2010). ....	37
<b>TABLE 3. 5</b> - TECHNICAL INFORMATION FOR THE BLUE LASER SYSTEM (ANTAL AND TAGADÓ, 2010). ....	38
<b>TABLE 3. 6</b> - SYNCHRONIZATION TIMES FOR THE PIV SYSTEM.....	40
<b>TABLE 4. 1</b> - PARAMETERS USED FOR THE HOT WIRE MEASUREMENTS.....	44
<b>TABLE 5. 1</b> - DISTANCES MEASURED WITH THEODOLITE WILD-N3 FOR THE HOT WIRE POSITION. ....	47
<b>TABLE 5. 2</b> - BOUNDARY LAYER CHARACTERIZATION UNDER VELOCITY AND PRESSURE GRADIENTS.....	54
<b>TABLE 5. 3</b> - PEAK RATIO RESULTS FOR THE DIFFERENT PARAMETERS.....	59
<b>TABLE 6. 1</b> - SUMMARY OF WIND EFFECTS ACCORDING TO BEAUFORT SCALE (ARENS AND BALLANTI, 1977). ....	71
<b>TABLE AI. 1</b> - UNCERTAINTIES AND OTHER CONSTANTS. ....	D

## List of symbols

### Acronyms

ABL	Atmospheric Boundary Layer
APG	Adverse Pressure Gradient
BL	Boundary Layer
CFD	Computational Fluid Dynamics
CL	Canopy Layer
CT3	Isentropic Compression Tube High Speed Turbine
DNS	Direct Numerical Simulations
FPG	Favourable Pressure Gradient
LDV	Laser Doppler Velocimetry
LES	Large Eddy Simulations
NATO	North Atlantic Treaty Organization
OpenFoam	Open source Field Operation And Manipulation
PM	Particulate matter
PIV	Particle Image Velocimetry
PLIF	Planar Laser Induced Fluorescence
SL	Surface Layer
STA	Service Technique de l'Aéronautique
TBL	Turbulent Boundary Layer
TUMULT	TURbulent Flow noise Modeling for under-and upperbody Load and Transmission analysis
UBL	Urban Boundary Layer
VKI	von Karman Institute for Fluid Dynamics
WAABLIEF	Wind tunnel for AeroAcoustic Boundary Layer Including pressure gradient eEffect
WHO	World Health Organization
ZPG	Zero Pressure Gradient

## Symbols

$C_f$	Skin friction coefficient	-
$C^+$	Constant in the log law	-
$C_3$	Goody model constant	-
$E_{11}$	Turbulent energy density	$m^2 \cdot s^{-2}$
$f$	Frequency	Hz
$\mathcal{F}$	Fourier transform	-
$H$	Shape parameter	-
$j$	Complex number	-
$\kappa$	von Karman constant	-
$k$	Wavenumber	$m^{-1}$
$M$	Mach number	-
$p$	Pressure	$N \cdot m^{-2}$
$P_{atm}$	Atmospheric pressure	$N \cdot m^{-2}$
$P_{wr}$	Pressure in the wind tunnel	$N \cdot m^{-2}$
$R$	Auto/cross correlation	-
$R_T$	Ratio of the outer to inner BL time scale	-
$Re$	Reynolds number	-
$Re_\theta$	Reynolds number for momentum thickness	-
$R_s$	Specific ideal gas constant	$J \cdot kg^{-1} \cdot K^{-1}$
$T$	Temperature	K
$T_i$	Turbulence intensity	%
$TF$	Frequency-dependent transfer function	-
$u$	Mean x (longitudinal) component of velocity	$m \cdot s^{-1}$
$u_\tau$	Friction velocity	$m \cdot s^{-1}$



$x$	Longitudinal distance	m
$y$	Transversal distance	m
$y$	Height for the BL profile	m
$\omega$	Angular frequency	rad.s <sup>-1</sup>
$\delta$	Boundary layer thickness	m
$\beta c$	Clauser's parameter	-
$\Gamma$	Cross-coherence	-
$\rho$	Density	kg.m <sup>-3</sup>
$\delta^*$	Displacement thickness	m
$\phi$	Frequency-wavenumber spectrum	N.m <sup>-2</sup> .Hz <sup>-1</sup>
$\nu$	Kinematic viscosity	m <sup>2</sup> .s <sup>-1</sup>
$\theta$	Momentum thickness	m
$\tilde{\omega}$	Strouhal number based on external variables	-
$\tau_w$	Wall shear stress	N.m <sup>-2</sup>
$\Phi_{pp}(\omega)$	Wall pressure power spectral density	(N.m <sup>-2</sup> ) <sup>2</sup> .Hz <sup>-1</sup>
$\Pi$	Wake strength parameter	-

### Sub- and Superscripts

$x$	longitudinal
$+$	normalized in wall units
$*$	normalized in integral units
amb	referred to ambient
w	referred to the wall
wt	referred to wind tunnel
ref	referred to reference
$\infty$	referred to freestream
$y$	transversal

## **Section 1 – Introduction**

This Section is divided into four sub-sections, aiming to present a summary about the general aspects of this report and the curricular internship.

### **Section 1.1 – *Framework and objectives of the internship***

The curricular internship is framed within the integrated master in Environmental Engineering of University of Aveiro, and it was performed at von Karman Institute for Fluid Dynamics (VKI). The internship had a duration of 3 months and 19 days, with a starting date at 12 of February and was programmed to end at 31 of May. It had the financial support of an ERASMUS fellowship.

This internship at VKI was framed under the TUMULT project (TUrbulent flow noise Modelling for Under- and upper-body Load and Transmission analysis). The main goal of TUMULT project is to address the interactions between a flow and the structure of a transportation system and develop innovative test-based, numerical and hybrid techniques for modelling and analysing the aeroacoustic sources of noise and their transmission to the interior compartment.

The TUMULT project is Belgium-funded in cooperation with Siemens Industry Software NV and the Catholic University of Leuven. VKI was responsible to analyse the upperbody flow induced pressure loading. To perform this, there is a need to study the Turbulent Boundary Layer (TBL) under pressure gradients.

The spatio-temporal characterization of a TBL is a topic of interest in many engineering fields such as ABL (atmospheric boundary layer), air transportation, noise reduction, etc.

The objective of the internship was to perform a specific test rig for the detailed investigation of the velocity and wall pressure field of the TBL in null, with zero, favourable and adverse pressure gradients, for two velocities, 15 and 25 m.s<sup>-1</sup>. To this end, advanced diagnostics, such as, microphone antenna, hot wire anemometry and particle image velocimetry (PIV) are combined to generate a database allowing to validate and improve, when necessary, wall pressure models accounting for Reynolds number and pressure gradient effects.

These tests were performed on the “wind tunnel for aeroacoustic boundary layer including pressure gradient effect” (WAABLIEF), former L2-A wind tunnel.

In the context of the course in Environmental Engineering, the main objective of this internship is to get experience about the application of several advanced experimental techniques, although these techniques are applied in a different area of environmental engineering, e.g, aeroacoustics field. Therefore, besides the component directly related with the subject of the internship, in this report is also presented a literature review regarding the type environmental application, especially in the field of air quality.

Additionally, the following courses were accomplished at VKI: “Introduction to OpenFOAM – Theory and Exercise”, “OpenFOAM General programming” and “Large Eddy Simulation. Theory and Applications”. OpenFOAM (“Open source Field Operation And Manipulation”) is an open source CFD toolbox under the GNU General Public License, and it is build up from C++ modules. The topic regarding the Large Eddy Simulations is going to be further described.

## **Section 1.2 – *von Karman Institute for Fluid Dynamics***

The von Karman Institute (VKI) has been founded in October of 1956, and its first name was Service Technique de l’Aéronautique (STA). Theodore von Kármán was the Institute Chairman until his death in 1956, and after that, the name of the organization was changed in memory of its founder (VKI, 2016 and URL 1).

VKI is a non-profit international education and scientific organization, hosting three departments: Aeronautics and Aerospace; Environmental and Applied Fluid Dynamics; Turbomachinery and Propulsion. This Institution provides post-graduate education in fluid dynamics such as: research master in fluid dynamics (former “VKI Diploma Course”); doctoral program; short training program; lecture series and encourages “training in research through research” (URL 1).

Currently, in VKI, two different type of tools are being used, such as, experimental approaches and numerical modelling techniques. Furthermore, this Centre of Excellence operates about fifty different wind tunnels, turbomachinery and other specialized test facilities (VKI, 2016 and URL 1).

The internship took place in the Department of Environmental and Applied Fluid Dynamics and the type of education programme adopted for the internship was the “short training program”. This Department deals with all natural and industrial processes in which fluid dynamics plays an important role. The research in this department is associated to the fields of: aeroacoustics, environmental engineering (pollution dispersion, wind energy, wind loading, pedestrian wind comfort, atmospheric and urban flows, including sand, ice and droplet phenomena, vehicle aerodynamics, uncertainty quantification and optimization), industrial process and safety and liquid and solid propulsion (VKI, 2016).

In summary, the Environmental and Applied Fluid Dynamics Department has 40 years of expertise in experimental fluid dynamics at full-scale and model-scale, including design, construction and testing of dedicated experimental facilities and the development of traditional and advanced, laser-based and acoustic measurement techniques. In the last 20 years, numerical modelling has been performed using Computational Fluid Dynamics (CFD) models and includes the development of turbulent models (URL 1).

### **Section 1.3 – Methodology**

Within this section, it is presented a brief overview about the methodology and tasks adopted during the internship, including some constraints and notes about the work performed at VKI.

Summarily, the methodology of this work consisted in collecting the TBL characteristics for different velocities and pressure gradients (with hot wire anemometer) and inject the results in turbulent wall pressure models (Goody and Rozenberg models), to compare afterwards with the results obtained with microphone antenna. The PIV was used to check the results obtained with the other techniques.

The experiments had taken place on the WAABLIEF, located on the VKI facilities, where the hot wire anemometer, microphone antenna and PIV techniques were applied.

Therefore, to achieve the main objective of this work, previously described in Section 1.1, the tasks performed along the internship can follow the next steps:

1. Bibliography review;

2. To study of the principles of the techniques applied to achieve the goal, including calibration processes;
3. To Perform the calibration of pressure transducer and hot wire anemometer;
4. To Perform the measurements with hot wire anemometer. These measurements were performed for different heights of the wind tunnel, from the bottom (closest as possible – using a *Theodolite Wild-N3*) until 140 cm, for two velocities, 15 m.s<sup>-1</sup> and 25 m.s<sup>-1</sup> and for different pressure conditions, e.g. zero, adverse and favourable pressure gradients. To achieve the different conditions the upper plate of the wind tunnel can be replaced;
5. The post-processing of the data was performed using MATLAB, and the data from hot wire anemometer will allows us to obtain the velocity profiles and the boundary layer characteristics for each condition;
6. The data obtained from the previous point, was feed into wall pressure models (e.g. “The Goody model (2002) and “Rozenberg model (2012)”) to obtain the wall pressure power spectral density;
7. Calibration of the microphone antenna;
8. To Perform the measurements with microphone antenna, for almost all the conditions applied with hot wire anemometer;
9. To post-process the data obtained with microphone antenna to obtain the wall pressure power spectral density;
10. After the analysis of the results obtained with microphone antenna, it was observed inconsistencies with the result for the free stream velocity, e.g., the result for this variable was different from the centre of the antenna to the sides. To verify this situation, it was decided to apply the PIV technique (non-intrusive technique);
11. Mounting and synchronization of the PIV system;
12. Perform PIV measurements for the same conditions as the other techniques;
13. Post-processing of the PIV results;
14. Discuss all the results;
15. To write the final report along the tasks mentioned previously.

However, due to technical issues in the wind tunnel, it was not possible to perform PIV measurements under the TUMULT project in time of the report delivery (from point 10 to 14).

To overcome this situation, and to get experience with PIV, I had assist the PhD student Gian Luca Gori and the Research Master student Simão Nóbrega with their research.

The work of Gian Gori is about: “LIF Temperature field Measurement for Internal Forced Convection Blade Cooling” and the work of Simão Nóbrega is about: “Determination of Gas Temperature in a cooling channel using LIF”. Beside the application of LIF (Laser-Induced Fluorescence) technique, they also had applied the PIV technique.

Regarding, the application of the Rozenberg model, the wind tunnel did not had a system to measure the pressure gradient, something that we add almost at the end of the internship. Therefore, the pressure gradient was calculated using the dimensions of the wind tunnel and wind tunnel velocity.

The post-processing of the data obtained with the microphone antenna, was performed by Dr. Christophe Schram (Associate professor at VKI).

On Section 3, for each experimental technique it is presented in more detail, how all the measurements were performed, including calibration procedures, description of the facilities, etc.

### **Section 1.4 – Report Structure**

This report is divided in two main parts. The first part, since Section 2 until Section 5 is directly related with the internship. The second part (Section 6) has the objective to give an example of a field of research, where the concepts and techniques learned during the internship can be applied. To achieve this, a bibliographic review about the type of application that we can have, is performed.

Therefore, it follows the organization of this report:

- **Section 1 – Introduction:** aims to present the subject, including the objectives and the framework of the internship;
- **Section 2 – Turbulent boundary layers:** the theoretical component necessary for the post-processing of the experimental results with hot wire anemometer and microphone antenna are described;

- **Section 3 – Experimental techniques:** the facility, experimental techniques, calibration and measurement procedures are described;
- **Section 4 – Uncertainty analysis:** the uncertainty analysis for hot wire anemometer is described and quantified;
- **Section 5 – Results and discussion:** this section aims to present the main results followed by a discussion;
- **Section 6 – Urban atmospheric boundary layer:** this section has the objective of performing a bibliographic review, demonstrating the type of environmental application of the concepts and techniques learned during the internship;
- **Section 7 – Conclusions and recommendations:** the conclusions about the experimental work and internship are presented, followed by some recommendations for future work.

## Section 2 – Turbulent boundary layers

The boundary layer (BL) is a very thin region usually originated under surfaces, where the viscosity effect prevails. The BL can be distinguished between two types: laminar or turbulent. The main difference between them is related with the Reynolds number. The general characterization of the BL can be found in any book related with fluid dynamics (Oliveira and Lopes, 2016). In this report, only the turbulent boundary layer (TBL) is going to be analysed.

The TBL is a significant source of vibration and noise for different type of structures, like cars, airplanes, trains, submarines, and others. These structures may be excited by pressure fluctuations due to the turbulent flow induced by their motions.

According to Maxit et al. (2015), to reduce the noise radiated from these structures is important to understand at the design stage how the structure reacts to the TBL excitation. Therefore, it is important to develop numerical tools allowing predicting the vibration or the radiated pressure from the structure excited by the turbulent flow.

Usually, the calculation process can be decomposed in three main steps:

- A stationary hydrodynamic model is used for the estimation of the TBL parameters over the surface of the structure from its geometry and the flow conditions;
- The spectrum of the wall pressure fluctuations is evaluated from the TBL parameters estimated in the previous step and by using one of the models proposed in literature. For more information, Schram (2018) gives a literature review about TBL models;
- The last step consists in using vibro-acoustic model to estimate the response of the structure to the pressure fluctuations, where the choice of the model depends on the frequency range of interest.



### Section 2.1 – Boundary layer characterization and spectral analysis

In a flat plate, the flow regime that was analysed corresponds to a subsonic regime with a Mach number inferior to 0.8. With this type of regime and a complete turbulent flow, the boundary layer velocity profile can be estimated by using the  $(1/7)^{\text{th}}$  power velocity profile law (Schram, 2018):

$$u = u_{\infty} \left( \frac{y}{\delta} \right)^{1/7} \quad (2.1)$$

where,  $u$  is the mean streamwise velocity,  $u_{\infty}$  is the free-stream velocity,  $y$  is the distance from the wall and  $\delta$  is the boundary layer thickness at which 99% of the free stream velocity is reached (Zapata, 2017 and Schram, 2018), Figure 2.1.

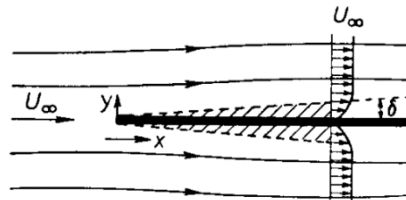


Figure 2. 1 - Boundary layer development over a flat plate (Zapata, 2017).

To calculate the free stream velocity, first the wind tunnel velocity,  $u_{wt}$ , (Equation 2.2) and a rescale velocity must be calculated, where  $P_{wt}$  is the wind tunnel pressure at the inlet.

$$u_{wt} = 12.26 \sqrt{P_{wt}} \quad (2.2)$$

The rescale velocity is calculated dividing the velocity measured with the hot wire by the wind tunnel velocity and multiplying this ratio by the velocity in study, 15 or 25  $\text{m}\cdot\text{s}^{-1}$ . The constant 12.26 from Equation 2.2 was determined previously to this internship, and it is calculated through the calibration of the wind tunnel (Zapata, 2017).

Afterwards,  $u_{\infty}$  was calculated making the average of the last seven points of the velocity profiles, that correspond to the heights,  $y$ , from the bottom plate: 140, 120, 100, 80, 70, 60 and 50 mm. This approach was used, because the standard deviation between these points was small.

The definition described on the first paragraph, can still lead to relatively inaccurate results, and integral quantities have been proposed, providing better accuracy and having distinct physical meanings. One defines the displacement thickness  $\delta^*$  (Equation 2.3) and other the

momentum thickness  $\theta$  (Equation 2.4). The displacement thickness represents the deviation of the potential flow streamlines, due to the fluid elements lag induced by the BL action. The momentum thickness defines the lost, exclusively in terms of potential flow (Oliveira and Lopes, 2016).

$$\delta^* = \int_0^\delta \left(1 - \frac{u(y)}{u_\infty}\right) dy \quad (2.3)$$

$$\theta = \int_0^\delta \frac{u(y)}{u_\infty} \left(1 - \frac{u(y)}{u_\infty}\right) dy \quad (2.4)$$

The shape factor  $H$  (Equation 2.5) allows to identify interesting flow regimes. It has a value of 2.6 for a laminar BL, about 1.4 for a TBL and should be equal to  $2.76 \pm 0.23$  when the BL is about to separate (Schram, 2018).

$$H = \frac{\delta^*}{\theta} \quad (2.5)$$

The Reynolds number for the momentum thickness,  $Re_\theta$ , was calculated using Equation 2.6, where  $\nu$  is the kinematic viscosity.

$$Re_\theta = \frac{\theta u_\infty}{\nu} \quad (2.6)$$

For the skin friction coefficient determination,  $C_f$ , it was used the Bradshaw method. The wall shear stress,  $\tau_w$ , and the friction velocity,  $u_\tau$ , are calculated using the following equations.

$$\tau_w = 0.5 \frac{P_{atm}}{287 T_{ref}} u_\infty^2 C_f \quad (2.7)$$

$$u_\tau = u_\infty \sqrt{\frac{C_f}{2}} \quad (2.8)$$

To obtain non-dimensional velocity profiles the following equations are used.

$$u^+ = \frac{u}{u_\tau} \quad (2.9)$$

$$y^+ = \frac{y u_\tau}{\nu} \quad (2.10)$$

Using the reduced variables (Equations 2.9 and 2.10), the canonical velocity profile of a turbulent boundary appears (Figure 2.2).

Close to the wall, a viscous sublayer is present, where  $y^+ < 5$  corresponding to a laminar flow. In this region, the mean velocity profile is proportional to the distance to the wall (Equation 2.11).

$$u^+ = y^+ \quad (2.11)$$

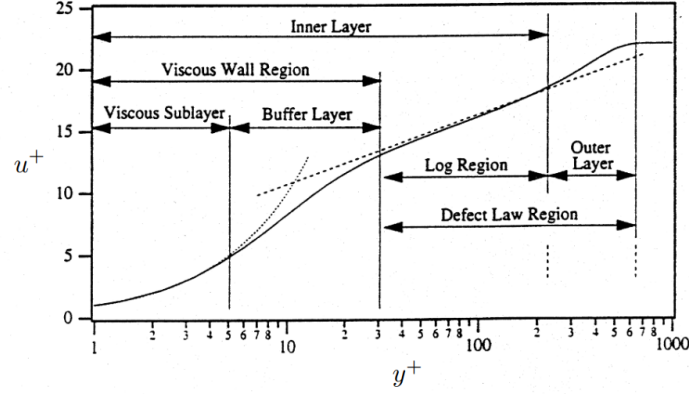


**Figure 2.2** - Rescale velocity profile of a turbulent boundary layer (Adapted from Zapata, 2017).

For  $30 < y^+ < 300$ , the mean velocity profile follows a logarithmic law. The mean velocity profile of this region, also called inertial region, can be approximated by Equation 2.12, with  $\kappa = 0.41$  (von Karman constant) and  $C^+ = 5.1$  (Schram, 2018).

$$u^+ = \frac{1}{\kappa} \ln(y^+) + C^+ \quad (2.12)$$

The buffer layer,  $5 < y^+ < 30$ , ensures the transition between the two former ones. Several attempts were made to describe, with a unified formula, the three regions of the TBL. The following convenient closed-form solution (Equation 2.13) was proposed by Musker (1979).

$$u^+ = 5.424 \times \arctan\left(\frac{2y^+ - 8.15}{16.7}\right) + \log_{10}\left[\frac{(y^+ + 10.6)^{9.6}}{(y^{+2} - 8.15y^+ + 86)^2}\right] - 3.52 + \\ + 2.44 \times \left\{ \Pi \left[ 6 \times \left(\frac{y}{\delta}\right)^2 - 4 \times \left(\frac{y}{\delta}\right)^3 \right] + \left(\frac{y}{\delta}\right)^2 \times \left(1 - \frac{y}{\delta}\right) \right\} \quad (2.13)$$

where,  $\Pi$  is the Cole's parameter that can be obtained by resolving the following transcendental equation (Equation 2.14).

$$2\Pi - \ln(1 + \Pi) = \frac{\kappa u_\infty}{u_\tau} - \ln\left(\frac{\delta^* u_\infty}{\nu}\right) - \kappa C^+ - \ln \kappa \quad (2.14)$$

For fully turbulent flows,  $\delta$ ,  $\delta^*$  and the friction coefficient,  $C_f$ , can be calculated analytically by using the following correlations (Equation 2.15, 2.16 and 2.17) over a flat plate. Where,  $Re_x$  is the local Reynolds number (Equation 2.18).

$$\delta = 0.38Re_x^{-0.2} \quad (2.15)$$

$$\delta^* = \frac{\delta}{8} \quad (2.16)$$

$$C_f = 0.0594Re_x^{-0.2} \quad (2.17)$$

$$Re_x = \frac{u_\infty x}{\nu} \quad (2.18)$$

The determination of the variables defined previously are important once they are going to be used as an input of the TBL models to estimate the spectral characteristics of the wall pressure fluctuations (Schram, 2018a).

The spectral analysis allows to know how the energy of turbulent structures spreads over frequencies or wavenumbers. The hypothesis used in this work is the Taylor frozen turbulence hypothesis. The Meteorology Glossary of American Society defines this hypothesis as: “An assumption that states that advection contributed by turbulent circulations themselves is small and that therefore the advection of a field of turbulence past a fixed point can be taken to be entirely due to the mean flow” (Zapata, 2017).

This assumption is valid if the velocity fluctuations of the flow are small regarding the mean velocity. Thus, if the low turbulence intensity is less than 10%, this hypothesis can be applied.

The spectral function for streamwise velocity fluctuations,  $E_{11}(k)$ , that contains the turbulent energy per frequency or wavenumber can be calculated using Equation 2.19, where  $k$  is the wavenumber,  $u$  is the mean velocity and  $\phi_{11}(f)$  is the Fourier transform of the temporal autocorrelation of instantaneous velocity signal (Equation 2.20).

$$E_{11}(k) = \frac{u}{2\pi} \phi_{11}(f) \quad (2.19)$$

$$\phi_{11}(f) = 2 \int_{-\infty}^{\infty} R_{11}(t) e^{-2j\pi ft} dt \quad (2.20)$$

## Section 2.2 – TBL wall pressure spectrum

According to Chevalier and Audoly (2015), the first difficulty in calculating flow noise phenomena induced by TBL is to extract the wall pressure fluctuation created by the TBL which excites the radiating structure. Usually, the methods used to well describe the turbulent structures appearing in the BL are DNS (Direct Numerical Simulation) and LES (Large Eddy Simulations), but these are very time consuming and expensive because of the required accuracy of spatial and temporal discretization. Therefore, these methods cannot be used for industrial applications. Methods such as statistical, empirical or semi-empirical approaches can be applied, besides using DNS and LES (Juvé et al., 2015).

The wall pressure characterizes the excitation source to be applied into the vibroacoustic model. Fluctuations only appear when the BL is no more laminar because they are originated from the TBL vortex formation.

Since the wall pressure has a random behaviour, its determination requires a spectral analysis. The spectral analysis is characterized in the frequency domain by a cross-spectrum density, which can be written in the physical space as well as in the wave number space (Chevalier and Audoly, 2015).

These spectral characteristics of the surface pressure fluctuations can be modelled by using time and space Fourier transforms of the pressure signals measured. The time-Fourier transform of the wall pressure field at the coordinate  $x$  defines the exponent sign convention as it follows (Equation 2.21), where,  $\omega$  is the angular frequency ( $\text{rad.s}^{-1}$ ).

$$P(x, \omega) = \frac{1}{2\pi} \int_{-\infty}^{\infty} p(x, t) e^{-i\omega t} dt \quad (2.21)$$

from which the pressure cross-spectrum can be computed with (Equation 2.23), where  $\mathbf{r}$  is spatial separation:

$$S_{pp}(x, \mathbf{r}, \omega) = \lim_{T \rightarrow \infty} \frac{2\pi}{T} E[P(x, \omega) P^*(x + \mathbf{r}, \omega)] \quad (2.22)$$

It also can be expressed using the following equation (2.23):

$$S_{pp}(\mathbf{r}, \omega) = \Phi_{pp}(\omega) \Gamma(\mathbf{r}, \omega) \quad (2.23)$$

$$\Gamma(r_x, r_y, \omega) = e^{-\alpha k_c |r_x|} e^{-\beta k_c |r_y|} e^{i k_c r_x} \quad (2.24)$$

where  $\Phi_{pp}(\omega)$  is the wall pressure power spectral density and  $\Gamma(\mathbf{r}, \omega) = \Gamma(r_x, r_y, \omega)$  is the cross-coherence between two points separated by a longitudinal  $r_x$  and by a transversal distance  $r_y$  (Equation 2.24), with  $k_c = \omega/U_c$ ,  $\alpha$  and  $\beta$  being related to the streamwise and spanwise correlation lengths. Recommended values for:  $\alpha = 0.116$  for smooth walls,  $\alpha = 0.32$  for rough walls and  $\beta = 0.7$  for smooth and rough walls. The dependency with respect to the position  $x$  have been omitted assuming statistical spatial homogeneity.

In Figure 2.3, a typical pointwise spectrum for TBL is represented (Zapata, 2017). It is possible to observe a typical behaviour from low frequencies to high frequencies, where the  $\Phi_{pp}(\omega)$  is higher for medium frequencies. Besides the typical behaviour for the spectrum, it is possible to analyse from Figure 2.3, different slopes that are associated with the frequency region.

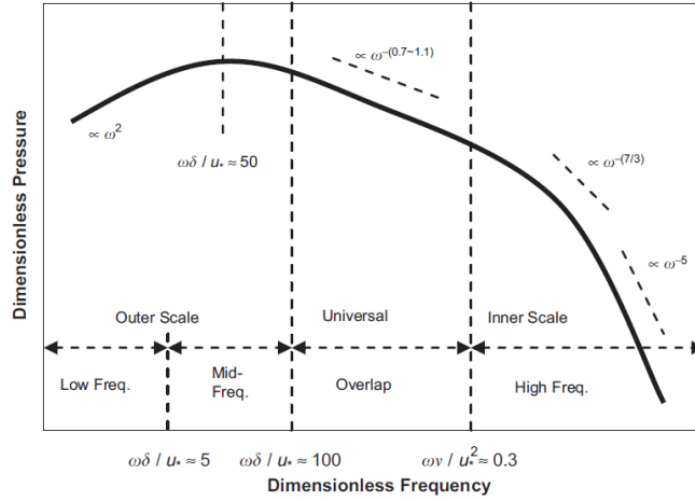


**Figure 2.3** - Typical pointwise spectrum  $\Phi_{pp}(\omega)$  for TBL (Zapata, 2018).

Consistently with the definition of the time-Fourier transform, the two-dimensional space-Fourier transform of the pressure cross-spectrum gives the representation of the pressure field in the frequency-wavenumber space (Schram and Van de Wyer, 2018):

$$\phi_{pp}(k, \omega) = \frac{1}{(2\pi)^2} \iint_{-\infty}^{\infty} S_{pp}(\mathbf{r}, \omega) e^{i\mathbf{k}\mathbf{r}} d^2\mathbf{r} \quad (2.25)$$

According to Schram and Van de Wyer (2018), the generic shape of the wavenumber-frequency TBL spectrum (Figure 2.4) comprises two components:

- the contribution of the turbulent pressure fluctuations (in red), with a  $(k_x, k_y)$  boundary elongated due to the smaller correlation in the spanwise direction than in

the streamwise direction and center around the wavenumber  $k_x = k_c = \omega/U_c$ , where  $U_c$  is the convection velocity;

- the part associated with the acoustic field, center around the origin and isotropic for a diffuse field, bounded by the acoustic wavenumber  $k_0 = \omega/c_0$ .

The sizes of both regions are increasing with frequency (Figure 2.4), and the region comprised between the acoustic and the convective components ( $k_0 < k < k_c$ ) is called the sub-convective zone.

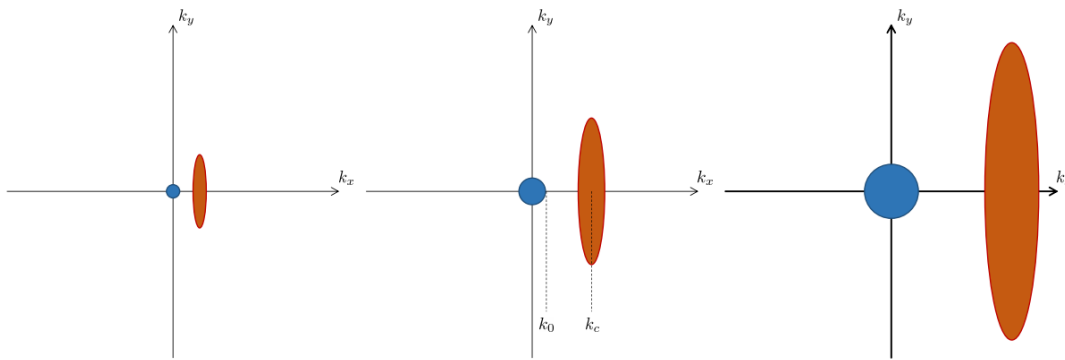


**Figure 2.4** - Generic structure of TBL wavenumber-frequency spectra, plotted for increasing frequencies from left to right. The blue region corresponds to an acoustic diffuse field and the red region corresponds to the convective ridge (Schram and Van de Weyer, 2018).

### Section 2.3 – Wall pressure models for TBL

In literature, several models exist to represent the wall pressure generated by the TBL excitation, however, most of the studies are restricted to zero pressure gradient (ZPG) boundary layer. In this work, the measurements were accomplished for three different conditions, ZPG, adverse pressure gradient (APG) and favourable pressure gradient (FPG). For each measurement it is going to be applied the best model according to the pressure gradient. Therefore, to calculate the pointwise wall pressure spectrum, two semi-empirical models can be applied: “Goody model (2002)” and “Rozenberg model (2012)”.

The Goody model is considered to be the one that reproduce in the best way the experimental data, but only for BL without any external pressure gradient, while the Rozenberg model takes into consideration the pressure gradients effect (Juvé et al., 2015).

Goody's objective was to consider the effects of the Reynolds number using an empirical approach. It was based on the Chase-Howe's model and experimental results. The Goody model was formulated with the boundary layer thickness,  $\delta$ . This variable is preferred to  $\delta^*$ , because the largest coherent structures are of the order of  $\delta$  (Goody, 2002). The final form of the Goody model is (Equation 2.26) (Goody, 2002):

$$\frac{\Phi_{pp}(\omega) u_\infty}{\tau_w^2 \delta} = \frac{3.0 \left(\frac{\omega \delta}{u_\infty}\right)^2}{\left[\left(\frac{\omega \delta}{u_\infty}\right)^{0.75} + 0.5\right]^{3.7} + [C_3 \left(\frac{\omega \delta}{u_\infty}\right)]^7} \quad (2.26)$$

where  $C_3$  can be calculated using Equation 2.27, and the ratio of the outer to inner BL time scale  $R_T$  is calculated using Equation 2.28.

$$C_3 = 1.1 R_T^{-0.57} \quad (2.27)$$

$$R_T = \frac{u_\tau \delta}{v} \sqrt{\frac{C_f}{2}} \quad (2.28)$$

The Rozenberg model (Rozenberg and Robert, 2012) is based on the Goody model, however it considers the pressure gradient effect on the wall pressure fluctuations spectrum. According to Schram (2018), two main effects of the pressure gradient are observed in experimental spectra: (i) a global broadband increase of the levels and (ii) an increase of the slope of the intermediate frequency range decay.

The final proposed model by Rozenberg and Robert (2012) is fully determined by (Equation 2.29):

$$\frac{\Phi_{pp}(\omega) u_\infty}{\tau_{max}^2 \delta^*} = \frac{[2.82 \Delta^2 (6.13 \Delta^{-0.75} + F_1)^{A_1}] [4.2 (\Pi/\Delta) + 1] \tilde{\omega}^2}{[4.76 \tilde{\omega}^{0.75} + F_1]^{A_1} + [C'_3 \tilde{\omega}]^{A_2}} \quad (2.29)$$

where, the Cole's parameter, is calculated using Equation 2.14,  $\tilde{\omega}$ , the Strouhal number based on external variables, is calculated using Equation 2.30. The other parameters are also presented in the following equations.

$$\tilde{\omega} = \frac{\omega \delta^*}{u_\infty} \quad (2.30)$$

$$\Delta = \delta / \delta^* \quad (2.31)$$

$$A_1 = 3.7 + 1.5 \beta_C \quad (2.32)$$

$$\beta_C = \frac{\theta}{\tau_w} \frac{dp}{dx} \quad (2.33)$$



$$A_2 = \min\left(3, \frac{19}{\sqrt{R_T}}\right) + 7 \quad (2.34)$$

$$F_1 = 4.76 \left(\frac{1.4}{\Delta}\right)^{0.75} [0.375A_1 - 1] \quad (2.35)$$

$$C'_3 = 8.8R_T^{-0.57} \quad (2.36)$$

$$\tau_{max} = \max\left[\mu \left(\frac{du}{dy}\right)\right] \quad (2.37)$$

## **Section 3 – Experimental techniques**

This section includes the theoretical principle of the hot wire anemometer, microphone antenna and particle image velocimetry (PIV). It also includes the calibration procedure and the description of the measurements performed. In Section 3.1, it is also included an overview of the wind tunnel, where the experiments were performed.

### **Section 3.1 – Overview of the wind tunnel**

The experiments were conducted on the “wind tunnel for aeroacoustic boundary layer including pressure gradient effect” (WAABLIEF), former L2-A wind tunnel, located on the VKI facilities. In Figure 3.1 the scheme and a picture of the WAABLIEF is presented, followed by a brief description.

This wind tunnel has the capacity to achieve a maximum velocity of  $35 \text{ m}\cdot\text{s}^{-1}$ . The air enters from the right side and goes through a honeycomb grid, with the aim of creating isotropic turbulence. It goes into the settling chamber that contains meshes and is contracted afterwards, increasing the velocity. It follows the test section, that starts with a set of three sand bands of 1 mm wide separated by 1 mm that generates the BL and bypass the transition process to get a fully TBL (Figure 3.2).

The test section has the following dimensions:  $2.15 \text{ m} \times 0.25 \text{ m} \times 0.25 \text{ m}$  (L×W×H) from the TBL sand trigger. This section (Figure 3.1) is inside of an anechoic chamber, acoustically insulated with 20 cm of acoustic foam and 1 cm of plywood. Afterwards, the air goes into the main silencer that avoids the sound emitted by downstream fan to go backwards and pollute the acoustic measurements. Then, the axial fan is driven with an external electric motor, where its rotational speed is adjusted manually with a potentiometer. At the end, the air is pulled out from the wind tunnel through a second silencer. Figure 3.3, presents in more detail a 2D plan of the test section of the WAABLIEF, including the measurement locations (“Station 0” or “Inlet”, “Station 1” and “Station 2”). The calibration of the wind tunnel was

performed previously to this work. On Zapata (2017) it is explained in detail how this calibration was performed.

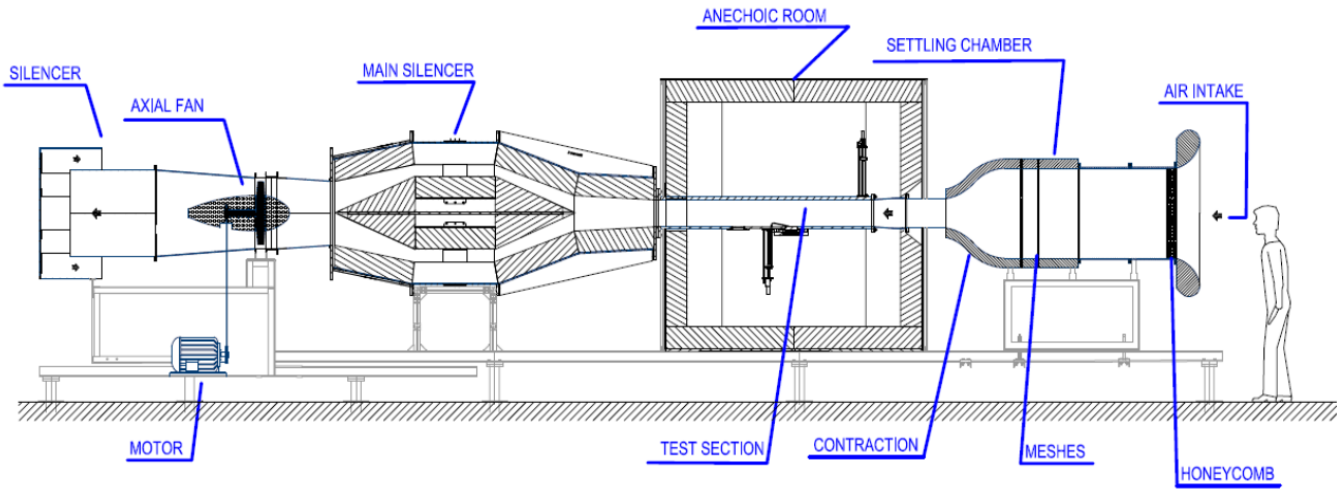


**Figure 3. 1** - Schematic (up) (Zapata, 2017) and picture (down) of the WAABLIEF located on the VKI facilities.



**Figure 3. 2** - Picture of the sand roughness on the entrance of the WAABLIEF (Zapata, 2017).

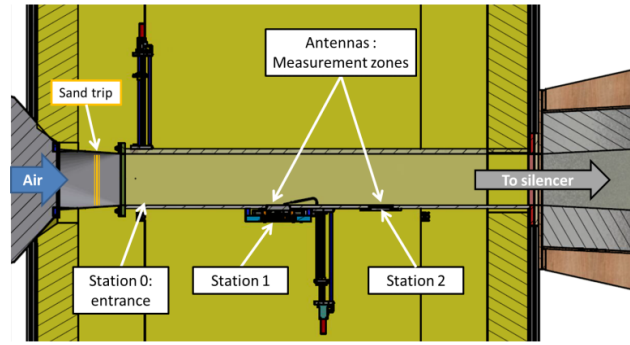


**Figure 3.3** - 2D plan of the WAABLIEF test section (Zapata, 2017).

### **Section 3.2 – Hot wire anemometer**

The hot wire anemometer has been used for many years, as a research tool/ measurement technique in fluid dynamics (Anthoine et al., 2009), once it is a significant instrument for measurements in laminar, transitional and turbulent flows, due to its accurate interpretation of the signal and simplicity in use (Özahi et al., 2010). The hot wire anemometer is still the only instrument delivering at the output, a truly analogue representation of the velocity up to high frequencies fluctuations (Anthoine et al., 2009).

#### **Section 3.2.1 - Theoretical background**

According to Anthoine et al. (2009), the hot wire anemometer consists of a sensor, a small electrically heated wire exposed to the fluid flow and of an electronic equipment, which performs the transformation of the sensor output into an electric signal. Contrary to most measuring instruments, the electronic circuitry forms an integral part of the anemometric system and has a direct influence on the probe characteristics.

The basic principle of the system operation is the heat transfer from the heated wire to the cold surrounding fluid, where the heat transfer is function of the fluid velocity. Thus, a relationship between the fluid velocity and the electrical output can be established. The purpose of the electronic circuit is to provide to the wire a controlled amount of electrical current (Anthoine et al. 2009).

The hot wire probes can be distinguished between four types of probes: single-wire, double-wire, triple-wire and multiple-wire. In Figure 3.4 a single-wire probe can be observed, which is the type used on the experiments. The material most commonly used for hot wire sensors

are tungsten, platinum and platinum-iridium alloys (Anthoine et al., 2009). When choosing a material for the sensor, some properties must be considered, such as:

- A high value of the temperature coefficient of resistance, to increase its sensitivity to velocity variations;
- An electrical resistance such that it can be easily heated with an electrical current at practical voltage and current levels;
- A high enough tensile strength to withstand the aerodynamic stresses at high flow velocities.

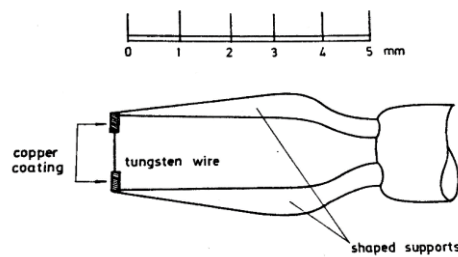


**Figure 3. 4** - Typical hot wire probe geometry (Anthoine et al., 2009).

The physical principle applied to the hot wire anemometer is the steady state energy balance (Equation 3.1), where  $I$  is the heating current flowing in the wire,  $R_w$  is the resistance at operating temperature  $T_w$ ,  $D$  and  $\ell$  it is the diameter and length,  $T_{amb}$  is the ambient temperature of the fluid and  $h$  is the heat transfer coefficient related to the other thermodynamic properties to the fluid in the Nusselt number,  $Nu$  (Equation 3.2).

$$I^2 R_w = \pi D \ell h (T_w - T_{amb}) \quad (3.1)$$

$$Nu = \frac{hD}{k} \quad (3.2)$$

where,  $k$  is the thermal conductivity coefficient for the fluid. The Nusselt number is a function of the Reynolds and Prandtl number. The problem that arises is to obtain a relation between the Nusselt number and the other thermodynamic properties of the fluid and the characteristics of the flow around the thin wire. According to Anthoine et al. (2009), the energy balance equation can be rewritten as (Equation 3.3):

$$I^2 R_w = |A + BU^n|(T_w - T_a) = H(U) (T_w - T_a) \quad (3.3)$$

where,  $A$  represents the natural convection term and  $BU^n$  the forced convection term (Anthoine et al., 2009).

The operating mode to be applied, can be the constant current or temperature. In this experiment the operating mode used was the constant temperature. It consists in a system in which the output from the bridge is amplified and used to control the supply voltage such as to maintain the wire temperature constant. The amplifier output required to maintain the wire at a constant temperature is a function of the flow velocity. The wire temperature is again fixed by the choice of the resistance of the bridge.

Another aspect to take in consideration is the incoming flow direction and orientation, once the output of a hot wire anemometer is also a function of this variables. For a more detailed description, Anthoine et al. (2009) gives all the numerical and theoretical component, including the measurement of turbulence, that is accomplished, by resolving the fluctuating components of the velocity field exploiting the directional sensitivity of the hot wire.

### ***Section 3.2.2 – Measurement chain and calibration procedure***

The measurement chain of the hot wire anemometer is shown in Figure 3.5. The hot wire used had a diameter of 9  $\mu\text{m}$ , and it was plugged in an anemometer unit, “92 series servoloop” (Figure 3.6), on the “direct output” with a coaxial cable of 4 m length. The output signal that goes out from the anemometer is fed into the National Instruments acquisition card that is a  $\pm 5$  V card with an anti-aliasing filter integrated. The card sends the digitally converted data to the computer that saves the data files, with the support of the LabView program (Zapata, 2017).

Proceeding to the calibration, the hot wire is plugged and mounted on a calibration nozzle, and the pressure tap of the nozzle is connected to the pressure transducer (Figure 3.7). The hot wire is placed close to the outlet of the nozzle in such a way that it is in the potential core of the jet. Only a static pressure tap is connected to the settling chamber, because the velocity in the settling chamber of the nozzle can be negligible because the static pressure is about 99,3% of the total pressure (Zapata, 2017).

Before the calibration of the hot wire anemometer, the pressure transducer must be calibrated (amplifier for six pressure sensors AMSYS Type AMS 5812). The calibration is performed using a water manometer (range of 0 mbar  $\pm$  10 mbar) and the LabView programme, which

gives an output of the pressure in volt. The calibration curve has a linear behaviour and there is no need to perform another calibration if the system is kept on.

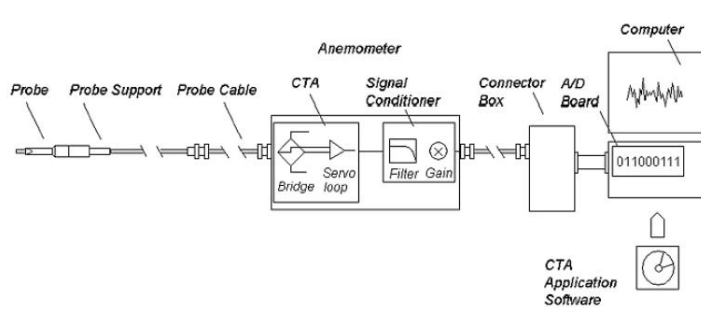


**Figure 3.5** - Typical hot wire measurement chain (Zapata, 2017).

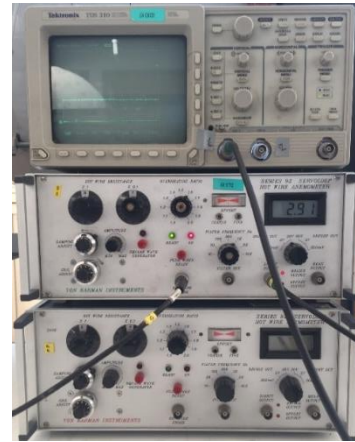


**Figure 3.6** - Picture of the oscilloscope (up) and anemometer (down) used in the experiments.

The anemometer unit must be adjusted with the proper hot wire resistance and overheat ratio of 1.6 ( $R_w/R_{amb}$ , where  $R_{amb}$  is the resistance at the air temperature,  $T_{amb}$ ). The square wave test was performed for  $0 \text{ m.s}^{-1}$  and  $30 \text{ m.s}^{-1}$  with an oscilloscope (Figure 3.6). For this test, frequency values of 6.7 kHz and 13 kHz were obtained for  $0 \text{ m.s}^{-1}$  and  $30 \text{ m.s}^{-1}$ , respectively.

Once the anemometer is ready, the calibration can be initiate. Since the measurements were performed for  $15 \text{ m.s}^{-1}$  and  $25 \text{ m.s}^{-1}$ , the velocities used in the calibration, range from  $0 \text{ m.s}^{-1}$  (hot wire with a cape) to  $30 \text{ m.s}^{-1}$ . The LabView program records for each velocity the following variables: fluid temperature, atmospheric pressure and pressure (volt).

In Table 3.1 the parameters for the data acquisition of the hot wire calibration are presented. The original acquisition time was 3 seconds, but in the post-processing of the data it was used only 1 second.

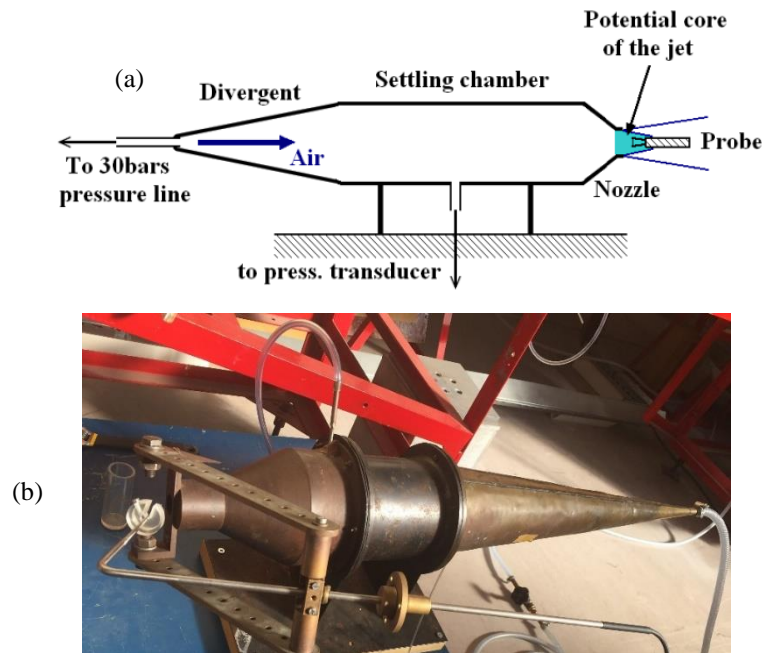


**Figure 3. 7** - Schematic (a) and picture (b) of the hot wire calibration nozzle (Zapata, 2017).

**Table 3. 1** - Data acquisition of the hot wire calibration.

<b>Acquisition time</b>	1 second
<b>Acquisition frequency for hot wire</b>	51,200 Hz
<b>Acquisition frequency for pressure and temperature</b>	1 kHz

During the calibration and measurements with hot wire anemometer, it was verified that the ambient temperature of the laboratory ranged substantially during the day. Therefore, when performing the post-processing of the data there is a need to include a temperature correction to the voltages measured. To do that first the hot wire temperature must be determined.

To determine the hot wire temperature, two calibration measurements were accomplished. First the output energy is measured for 16 points ranging from 0 m.s<sup>-1</sup> to 30 m.s<sup>-1</sup>. After 30 m.s<sup>-1</sup> be achieved, the jet flow must keep this velocity for some time.

The 16th point (30 m.s<sup>-1</sup> with an output energy,  $E_1^2$ ) corresponds to a certain jet flow temperature,  $T_1$ . If we leave the jet flow at that velocity, the temperature will decrease. When the temperature difference between the last acquisition and the current moment is enough,



the 17th point is taken for 30 m.s<sup>-1</sup> ( $E_2^2$  and  $T_2$ ). Then, the acquisition keeps going until achieve 0 m.s<sup>-1</sup> (hot wire with the cape).

This way it is possible to interpolate the hot wire temperature (Equation 3.4) for a reference velocity (30 m.s<sup>-1</sup>), since the output energy and temperature for the same velocity are different.

$$T_w = \frac{E_1^2 \times T_2 - E_2^2 \times T_1}{E_2^2 - E_1^2} \quad (3.4)$$

Afterwards, it is necessary to perform a temperature correction of all the energies from the calibration ( $E_{output,i}$ ), where each one of it have a temperature ( $T_{output,i}$ ) to obtain the energy correction for each point ( $E_{correction,i}$ ). All the calculations need to have the same reference temperature ( $T_{reference}$ ), 16°C in these experiments, once the temperatures measured during the calibration and measurements ranged from 11 to 20 °C (Equation 3.5).

$$E_{correction,i} = E_{output,i} \times \sqrt{\frac{T_w - T_{reference}}{T_w - T_{output,i}}} \quad (3.5)$$

The linearization of the hot wire signal can be performed in two ways, using an analog on-line instrument, denominated “analog linearizer”, or by performing a “numerical linearization”, using a computer-based data acquisition system to sample and digitize the signal, and then to recalculate instantaneous velocities (Anthoine et al., 2009).

In the current experiment, the transfer function for the calibration was obtained using the numerical linearization, by a 4rd order polynomial function (Equation 3.6), with the anemometer output (Pressure [V]) on x-axis and the velocity (output from the pressure transducer with application of the Bernoulli’s principle) on the y-axis.

$$U(V) = a_0 + a_1V + a_2V^2 + a_3V^3 + a_4V^4 \quad (3.6)$$

The hot wire anemometer must be always calibrated before an experiment, since it is influenced by the fluid conditions (pressure and temperature).

### *Section 3.2.3 – Measurement of the distance between the hot wire and the bottom wall*

To position the hot wire closest as possible to the wall, to be located in the viscous wall region of the TBL, it is used a theodolite WILD-N3 (Figure 3.8) and a Johnson block of 3 mm (distance calibration device). The theodolite is a precise optical measurement tool, with the possibility to measure distances with a precision of  $\pm 10 \mu\text{m}$ . According to Zapata (2017), it has a minimum focal distance of 2.15 m and a magnification factor of  $\times 42$ . The precise measurement of this distance is important because of the computation of the boundary layer characteristics, particularly the skin friction (Zapata, 2017).



**Figure 3. 8** - Theodolite Wild-N3 (Zapata, 2017).

**1:** External aiming reticle, **2:** Vertical adjustment screws, **3:** Focus screw, **4:** User's optics and **5:** Micrometer screw

The Johnson block is placed in the measurement test sections, and with the theodolite and a mirror, the measurement of the distance between the hot wire and the test section is performed. The use of the theodolite can be following by these steps (Zapata, 2017):

1. The theodolite must be screwed on a tripod which has to stand on a stable floor;
2. The user must aim roughly at the target with the reticle (1) to perform after the adjustment of the height with the vertical screws (2);
3. Once the target is seen as blurry in the optics (4), the user adjusts the sharpness of the image with the focus screw (3).
4. The distance corresponding to a certain number of graduations on the micrometre screw (5) can be measured by placing next to the target an object that the height is known.

Since the graduation on the micrometre screw that defines the height of the Johnson block is known, the distance between the hot wire and its reflection ( $d$ ) can be measured (Figure 3.9).

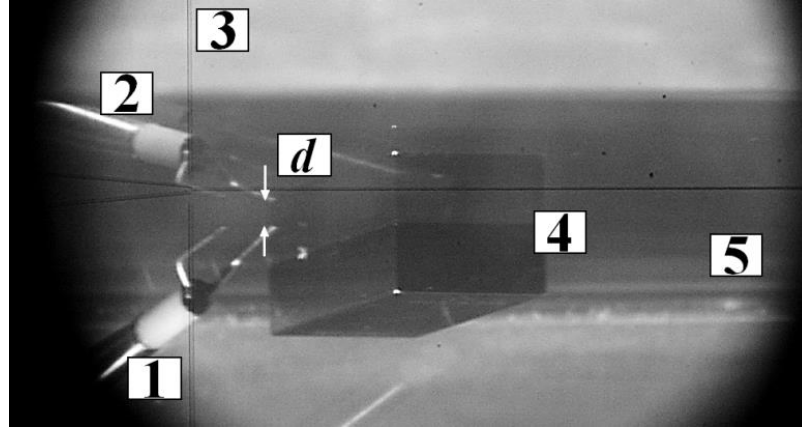


**Figure 3. 9** - View in the theodolite optics (Zapata, 2017).

**1:** Hot wire, **2:** Reflection of the hot wire on the wall's test section, **3:** Internal reticle of the theodolite, **4:** Johnson block and its reflection, **5:** Wall's test section, **d:** distance between the hot wire and its reflection.

### *Section 3.2.4 – Measurements procedure*

The measurements with hot wire anemometer were performed to obtain the velocity profiles and the characteristics of the turbulent boundary layer (TBL) with height, e.g. from the bottom (the position of the wire closest to the bottom wall as possible, as described in Section 3.2.3) until 140 mm from the initial height of the wind tunnel.

Three types of pressure conditions were performed: zero pressure gradient (ZPG), favourable pressure gradient (FPG) and adverse pressure gradient (APG). To obtain these conditions, the upper plate of the wind tunnel can be replaced (Figure 3.3), to represent the desired conditions. Table 3.2 presents a summary of the measurements performed with hot wire anemometer, in presence of velocity and pressure gradients. The measurements were performed in three locations of the wind tunnel: “Inlet”, “Station 1” and “Station 2”; for different velocities: 15 and 25 m.s<sup>-1</sup>.

In the Figure 3.10, it follows the design of the wind tunnel test section with the two Ramp configurations, Ramp 1 (top) and Ramp 2 (bottom), respectively. With Ramp 1: the Station 1 is characterized with a FPG; while with Ramp 2: the Station 1 is characterized with a variable pressure gradient and Station 2 with an APG. The data acquisition for the

measurements had the same characteristics as presented in Table 3.1, with exception of the acquisition time, that was 60 seconds.

The bottom plate of the wind tunnel test section can be observed in detail in Figure 3.11, with the location for the antenna and hot wire placements.

**Table 3. 2** - Synthesis of the measurements performed with hot wire anemometer.

Measurement location/Type of plate	Inlet	Station 1	Station 2
<b>Flat Plate</b> (ZPG)	15 m.s <sup>-1</sup>	-	-
	25 m.s <sup>-1</sup>	25 m.s <sup>-1</sup>	25 m.s <sup>-1</sup>
<b>Ramp 1</b> (FPG at Station 1)	-	15 m.s <sup>-1</sup>	-
	-	25 m.s <sup>-1</sup>	-
<b>Ramp 2</b> (variable PG for Station 1 and APG for Station 2)	-	15 m.s <sup>-1</sup>	15 m.s <sup>-1</sup>
	-	25 m.s <sup>-1</sup>	25 m.s <sup>-1</sup>

For flat plate, Station 1 and Station 2, the measurements for 15 m.s<sup>-1</sup> were not accomplished because it was performed before by Zapata (2017). The Inlet measurements for the two Ramp configurations were not done due to technical issues, and for Station 2 with Ramp 2 it was only performed as additional information.

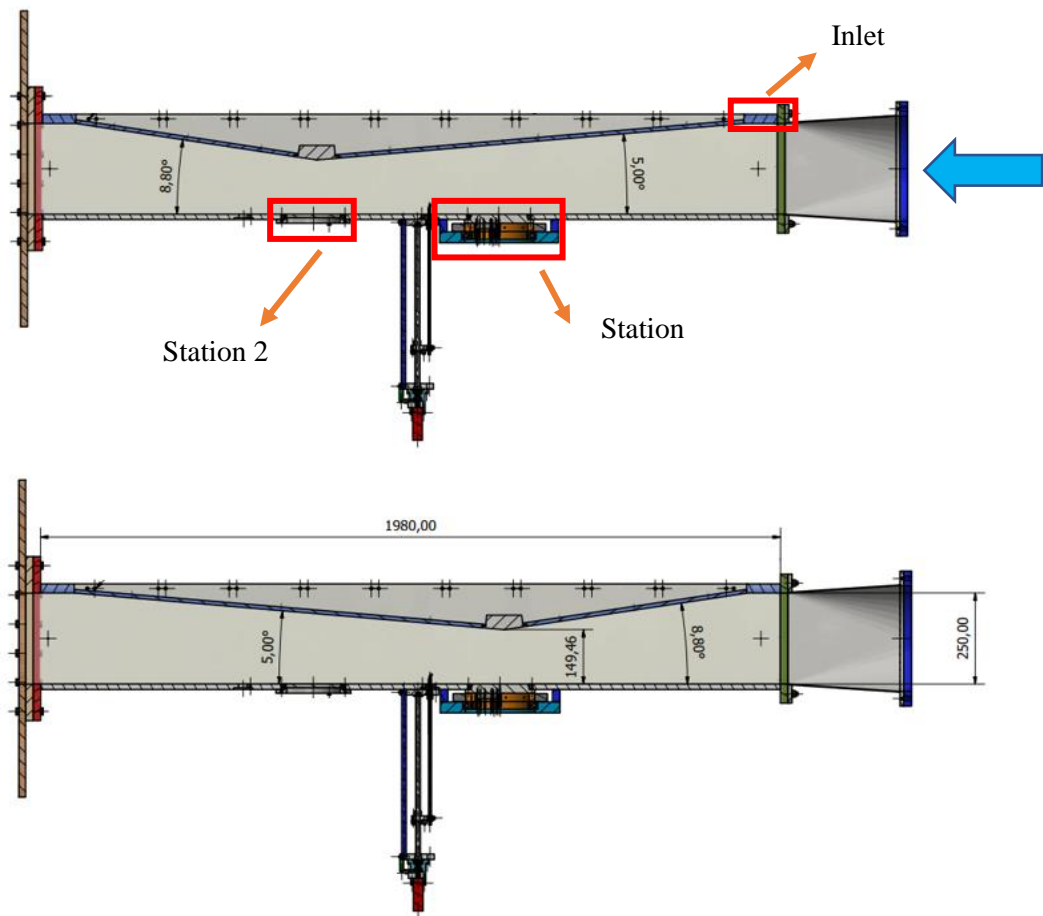


**Figure 3. 10** - Wind tunnel test section in presence of the two Ramp configurations, Ramp 1 (top) and Ramp 2 (bottom) respectively (Courtesy of the VKI design office).

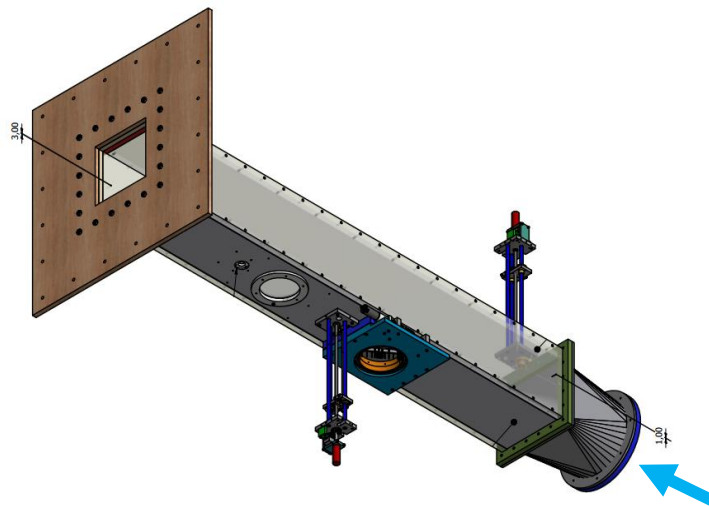


**Figure 3. 11** - Detailed design of the bottom plate of the wind tunnel test section for the microphone antenna and hot wire (Courtesy of the VKI design office).

### **Section 3.3 – Wall pressure measurements**

The evaluation of pressure and velocity field is an essential part of experimental fluid dynamics. Total and static pressure must be measured over a wide range of Mach and Reynolds numbers to define the forces on bodies or walls and the local magnitude and direction of the fluid velocity (Anthoine et al., 2009).

#### ***Section 3.3.1 – Theoretical background***

Quite often, the measurement of pressures must be accomplished in unsteady conditions, such as, measurement of time-varying pressure (with periodic oscillations or step changes) or pneumatic scanning, using a single pressure transducer or several different steady-state pressures. In cases like this, phenomena like the time or frequency response of the pressure measuring system (pressure tap or probe, pressure line, valves or transducer) and the effect of various parameters of the measuring system must be considered. This is necessary to avoid measuring errors, and in case an important number of pressures must be measured, to allow minimization of the total measuring time (Anthoine et al., 2009).

The wall pressure measurement performed in this work, consists in using a microphone antenna with 64 electret microphones (see Section 3.3.2).

An electret microphone is a device that uses two conducting plates to capture sound waves and translate them into electrical waves. This type of microphone is omnidirectional, which means that can capture sound from all directions. It is good in performance and not too expensive (URL 3).

It uses two conducting plates, where one is fixed while the other is a vibrating diaphragm. They work by letting the incoming sound waves from a source of sound from any direction to change the capacitance between two conducting plates. The diaphragm is the conducting plate that receives the sound waves and it causes the change in capacitance. This change produces variance in voltage on the back plate and this, in turn, sends electrical signals to output devices like speakers and sound systems (URL 3).

### Section 3.3.2 – Microphone antenna

The measurements of unsteady wall pressure beneath a TBL were performed by using a rotating microphone antenna with 64 electret microphones deposited from the surface of the antenna (Figure 3.12).

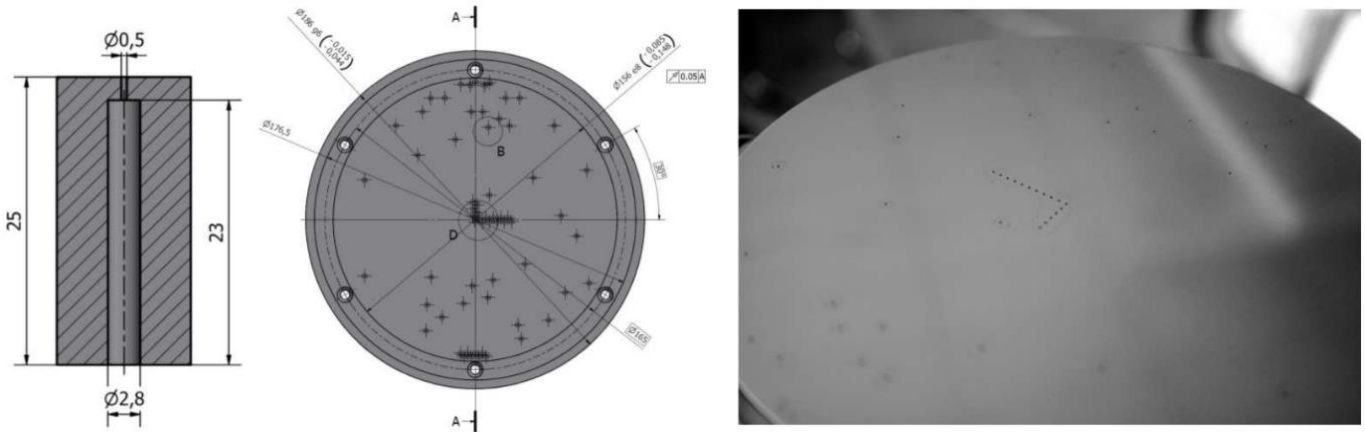


**Figure 3.12** - Installation of the microphones in the antenna disk (the electret microphone is not shown but is inserted till the end of the 2.8 mm cylindrical cavity) (Schram and Van de Weyer, 2018).

The microphones are deposited from the surface. According to Schram and Van de Weyer (2018), the microphone array is installed within a 0.186 m diameter circular plate made of steel with a thickness of 0.025 m, having its upper face flush with the lower surface of the square test section. The antenna is fitted with a rotating mechanism controlled by a step motor, and the maximum usable area for placing the unsteady pressure sensors is 0.15 m ( $D_{ant}$ ).

The model of the 64 electret microphones are “Knowles model FG-23329-C05”, having a small size and providing a flat frequency response up to 10 kHz, where the sensing head of the microphone is about 0.0026 m diameter. The microphones are connected to the upper surface of the antenna by a line-cavity arrangement (Figure 3.12). This arrangement requires an in-situ calibration to correct for the amplitude and phase lag of the line-cavity system (Schram and Van de Weyer, 2018).

For the optimum location of the pin holes of the microphones on the antenna, an algorithm was created by Schram and Van de Weyer (2018). This paper presents a detailed description about the optimization process. The result of the design (Figure 3.13) gave the best position of the microphones to have the biggest population of distances between microphones, that

allows in Fourier domain to have a high population of different wavenumber, which is advantageous for the measurement of wavenumber-frequency cross-spectra (Zapata, 2017).

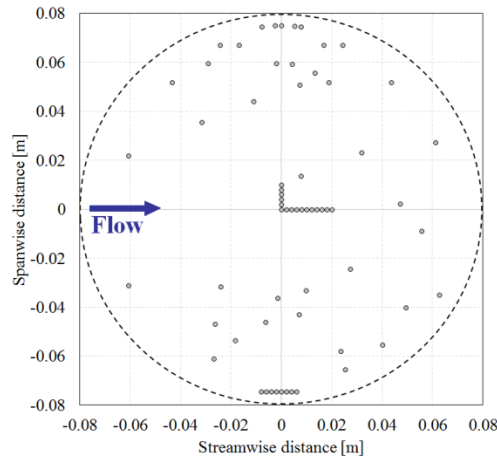


**Figure 3.13** - Surface map of the location of the 64 microphones on the antenna (Zapata, 2017).

### *Section 3.3.3 – Measurement chain and calibration procedure*

Figure 3.14 represents the measurement chain of the wall pressure measurements. According to Van de Wyer et al. (2018), this antenna requires an in-situ calibration, due to the variability of the electrets response functions, and to correct for the amplitude modulation and phase lag of the line-cavity system.

The calibration can be achieved using a calibrator device (Figure 3.15). This device consists of a steel cylinder drilled to accommodate a channel guiding the waves emitted by the loudspeaker to the electret microphone nested in the antenna, and a sidebranch channel towards a calibrator microphone (Bruel & Kjaer model 4938 with pre-amplifier type 2670). The diameter of the central channel is 0.013 m, ensuring plane wave propagation up to 15,152 Hz Van de Wyer et al. (2018)

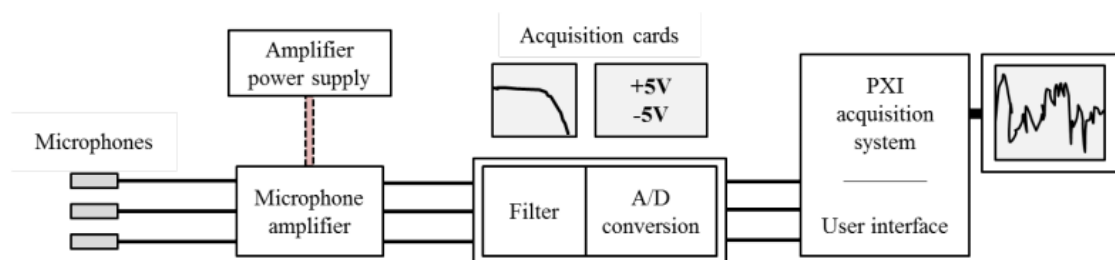


**Figure 3.14** - Measurement chain of the wall pressure measurements (Zapata, 2017).



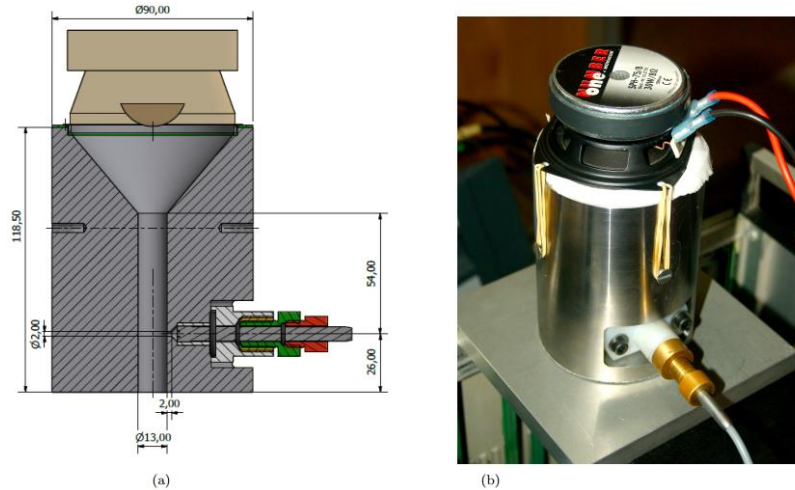


**Figure 3.15** - Wall microphone calibrator (a) CAD view (b) Placed on top of the reference microphone (Van de Wyer et al., 2018).

According to Van de Wyer et al. (2018), the dynamic calibration of the microphone antenna is performed in two steps:

- the calibrator is placed on top of an auxiliary flat plate hosting a reference microphone (same model as the calibrator microphone) having its membrane levelled flush with the plate upper surface; the measurements of the sound field emitted by the loudspeaker provide the frequency-dependent transfer function,  $TF$ , between the reference microphone and the calibrator microphone (Equation 3.7), which links the voltage of the electret microphones to the wall pressure;
- the calibrator is then placed over the antenna, with its central channel aligned with the pinhole of the electret to calibrate; this provides the transfer function,  $TF$ , between the calibrator microphone and the electret microphone including its line-cavity system (Equation 3.8).

$$TF_{cal-ref} = \frac{\mathcal{F}(p'_{ref})}{\mathcal{F}(p'_{cal})} \quad (3.7)$$

$$TF_{ele-cal} = \frac{\mathcal{F}(p'_{cal})}{\mathcal{F}(p'_{ele})} \quad (3.8)$$

where,  $\mathcal{F}$  is the Fourier transform. In practise, the transfer function is obtained with the Welch periodogram spectral averaging procedure using the Matlab function *tfestimate*.

An Agilent model 33120A signal generator fed through a power amplifier to the loudspeaker (Monacor model SPH-75/8) produces a linear chirp signal spanning from 100 Hz to 15 kHz over a period of 1 s. The acquisition time is 60 s with a sampling rate of 51,200 Hz.

The Bruel & Kjaer microphones are connected to a Bruel & Kjaer Nexus type 2692-C charge amplifier, hosting a low pass anti-aliasing filter with cut-off frequency set to 25,600 Hz (Van de Wyer et al., 2018).

The transfer function between the electret microphone and the reference microphone can be obtained by multiplying equations 3.7 and 3.8, as it follows (Equation 3.9).

$$TF_{ele-ref} = \frac{\mathcal{F}(p'_{ref})}{\mathcal{F}(p'_{cal})} \times \frac{\mathcal{F}(p'_{cal})}{\mathcal{F}(p'_{ele})} = \frac{\mathcal{F}(p'_{ref})}{\mathcal{F}(p'_{ele})} \quad (3.9)$$

In previous experiments it was observed that the Fourier transform for the “cal” on equation 3.7 and 3.8 did not had the same value. The solution for this problem, since we are working with ratios on the equations, instead of using pressure levels, it is possible to apply the voltage values.

After calculating the transfer function between the electret microphones and the reference microphone (Equation 3.9), to finish the calibration application the following steps were applied:

1. Application of the Fourier transform (FFT) of the electrical signals from the electret microphones ( $p_{uncal}$ );
2. Multiplication of  $TF_{ele-ref}$  by the  $FFT(p_{uncal})$ ;
3. Perform the inverse Fourier transform (IFFT) of the result given by the previous step;
4. Computation of the cross-power-spectral-densities of the wall pressure signals;
5. Comparison of the measurements to the models.

### ***Section 3.3.4 – Measurements procedure***

The measurements with the microphone antenna were performed for the velocities 15 and 25  $m \cdot s^{-1}$ . In Table 3.3 is shown the conditions of the measurements with the microphone.

For each condition, the microphone antenna was positioned in four different angles:  $0^\circ$ ,  $90^\circ$ ,  $180^\circ$  and  $270^\circ$ , and for each measurement, it was performed 16 acquisitions of 2,097,152

samples, where one acquisition takes approximately 40 seconds. The sampling rate was the same applied in the calibration (51,200 Hz).

**Table 3. 3** - Summary of the measurements for the microphone antenna.

Measurement location/Type of plate	Inlet	Station 1	Station 2
<b>Flat Plate (ZPG)</b>	-	15 m.s <sup>-1</sup>	15 m.s <sup>-1</sup>
	-	25 m.s <sup>-1</sup>	25 m.s <sup>-1</sup>
<b>Ramp 1 (FPG)</b>	-	15 m.s <sup>-1</sup>	-
	-	25 m.s <sup>-1</sup>	-
<b>Ramp 2 (APG)</b>	-	-	15 m.s <sup>-1</sup>
	-	-	25 m.s <sup>-1</sup>

Christophe Schram was the person responsible to perform the post-processing of the data for the calibration and measurements with microphone antenna. Therefore, in this report, the only results that are going to be presented is the power spectral density,  $\Phi_{pp}(\omega)$  for 0° angle to compare this variable with the one calculated with hot wire anemometer. For more details, see Section 5.

### **Section 3.4 – Particle image velocimetry (PIV)**

The particle image velocimetry (PIV) is a non-intrusive technique that benefited from the developments of laser doppler velocimetry (LDP) (Anthoine et al., 2009).

As mentioned before, in Section 1.3, due to technical issues it was not possible to implement PIV under the TUMULT project. Due to this reason, I had assist the PhD student Gian Luca Gori and the Research Master student Simão Nóbrega, with their research.

#### **Section 3.4.1 – Theoretical background**

PIV is based, like LDV, on the measurement of the velocity of tracer particles carried by the fluid. However, rather than concentrating light in a small probe volume as in LDV, a complete plane of the flow under investigation is illuminated (Anthoine et al., 2009).

According to Raffel et al. (2007), in most applications of PIV, tracer particles have to be added to the flow. These particles have to be illuminated in a plane of the flow at least twice within a short time interval. The light scattered by the particles must be recorded either on a single frame or on a sequence of frames. The displacement of the particle images between the light pulses must be determined through evaluation of the PIV recordings, where it is assumed that the tracer particles move with the local flow velocity between the two illuminations.

According to Anthoine et al. (2009) there are three types of image recording: light sheet technique, photographic technique and video technique. Afterwards, the image processing can be accomplished with one of these techniques: Young's fringe method; Full optical processing; Full digital processing; Hybrid processing. In the case of this work, it was used the photographic technique and full digital processing.

Usually, a PIV system consists in several components, such as camera, laser, synchroniser, seeding system, etc. (Antal and Tagadó, 2010). The typical setup for PIV recording in a wind tunnel is represented in Figure 3.16, where some components of the system can be observed.

When proceeding to the evaluation, PIV images are divided in small subareas called "interrogation areas". For each interrogation area, the local displacement vector for the images with tracer particles of the first and second illumination is determined using statistical methods, such as, auto- and cross-correlation (Raffel et al., 2007). According to this author, it is assumed that all particles within one interrogation area have moved homogeneously between the two illuminations. The projection of the vector of the local flow velocity into the plane of the light sheet, two-component velocity vector, is calculated taking into account the time delay between the two illuminations and the magnification at imaging. Then, the process of interrogation is repeated for all interrogation areas of the PIV records.

According to Schram (2003), a typical cross-correlation map can be illustrated as in Figure 3.17, where the distance of the displacement peak  $R_D$  to the origin gives the most probable displacement of the particles contained in the interrogation area. The noise present on the cross-correlation map is made of a mean component  $R_C$  that is due to the mean background intensity of the particle images, and a fluctuating component  $R_F$  that is mainly due to random matching of particles.

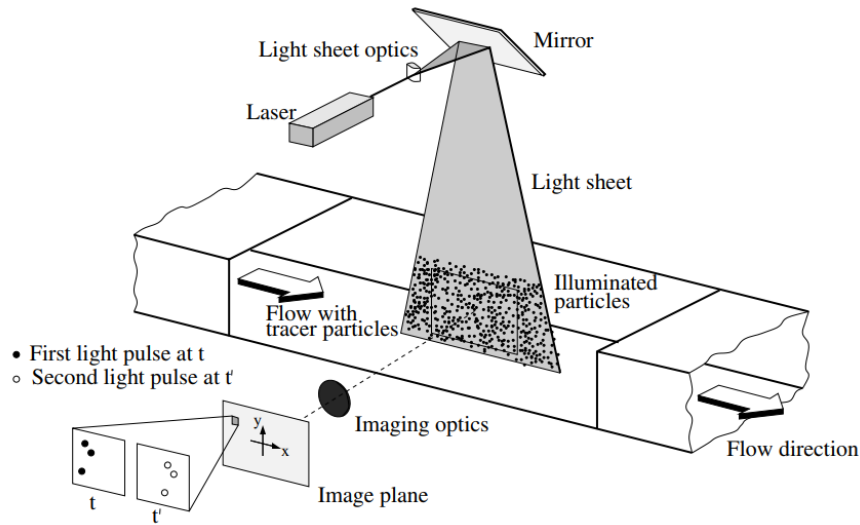


**Figure 3. 16** - Typical arrangement of a PIV system in a wind tunnel (Raffel et al., 2007).

The reliability of the measurement is mainly a function of the signal to noise ratio (SNR) of the correlation. This ratio is commonly defined as the ratio of the amplitude of the highest correlation peak by a typical noise amplitude. The noise amplitude can be defined as the amplitude of the second highest correlation peak (Schram, 2003).

The quality of the PIV measurements is essentially dependent on the seeding, the laser intensity and the camera aperture. When performing PIV measurements, it is important to eliminate all sources of reflection of the laser once it will influence the images recorded.

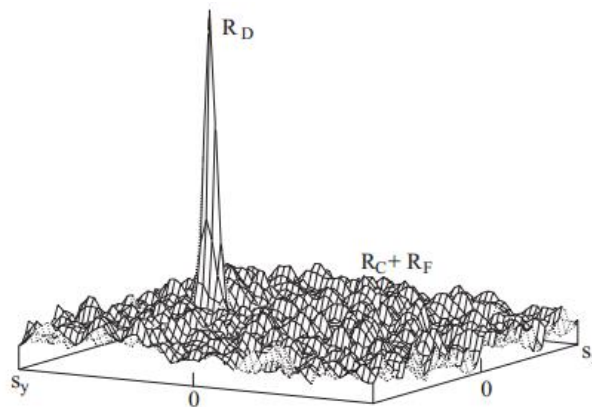


**Figure 3. 17** - Cross-correlation map of two single exposure frames (Schram, 2003).

The seeding is the first element that determines the quality of the PIV measurements (Schram, 2003). According to this author, a suitable seeding for PIV is:

- non-perturbing;
- a flow tracer with minimum velocity lag;
- homogeneously spread in the flow;
- efficient in scattering the light.

### Section 3.4.2 – Description of the equipment

The experiments were performed at the Planar Laser Induced Fluorescence (PLIF) facility, in the Turbomachinery and Propulsion Department at VKI. In Figure 3.18, the 3D design of this facility is represented. Regarding the camera used, in Table 3.4 is presented the technical data for the PCO Sensicam.

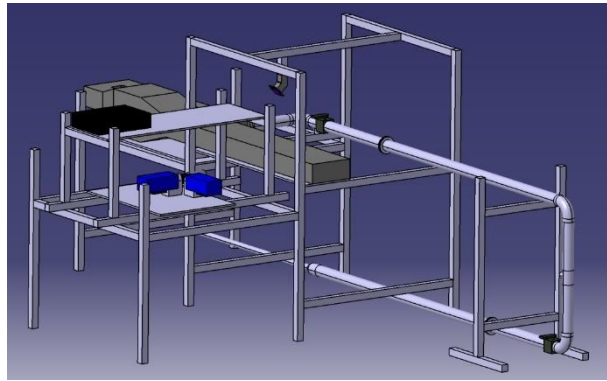


Figure 3. 18 - Design of PLIF facility (Gori, 2018).

Table 3. 4 - Technical data of the camera (Antal and Tagadó, 2010).

<b>Resolution</b>	1280 x 1024
<b>Frame-pair rate</b>	10 Hz
<b>Separation time</b>	200 ns – 1000 s
<b>CCD size</b>	2/3" (6.6 x 8.8mm)

The laser system used was the “Blue laser System” consisting on two lasers (see Figure 3.20). The type of the ICE control for this system is ICE450. The technical data for the laser can be observed in Table 3.5. The laser can be triggered both internally and externally. The intensity of the laser is changed by changing the Q-Switch delay.



**Figure 3. 19** - Two power supply for the blue laser system type BSL200 CFR300 (Antal and Tagadó, 2010).

**Table 3. 5** - Technical information for the Blue Laser System (Antal and Tagadó, 2010).

<b>Wave length</b>	532 nm
<b>Maximum frequency</b>	15 Hz
<b>Energy</b>	200 mJ
<b>Starting diameter</b>	6 mm
<b>Pulse duration</b>	8 ns

To carry out a successful PIV measurement it is important to synchronise the laser pulses with the camera integration times. The synchroniser used was a MotionPro Timing Hub. This synchroniser provides eight independent synchronization signals with 20 ns resolution, to integrate different devices. On Figure 3.20, it follows an image of the synchronization interface.

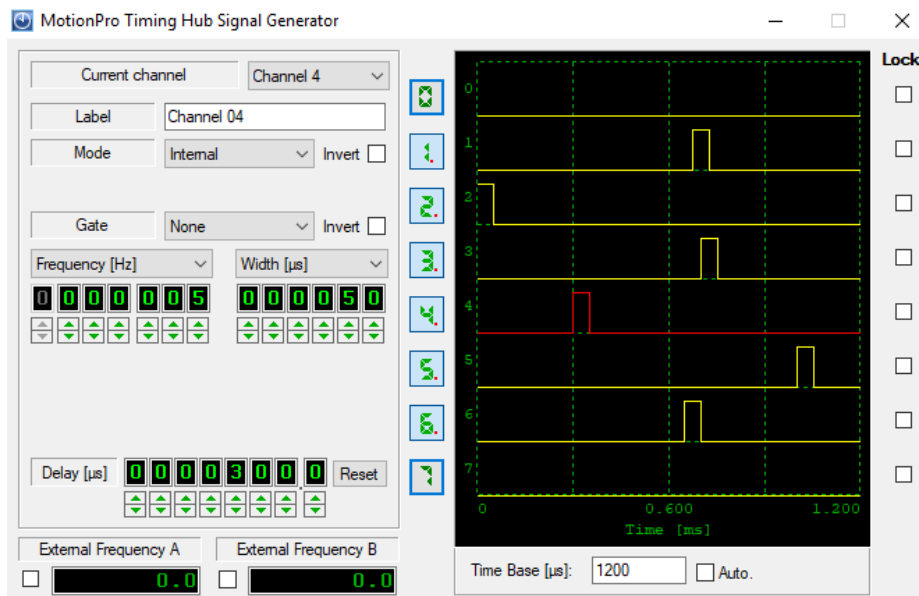


**Figure 3. 20** - MotionPro Timing Hub software.

To synchronise the PIV camera with the two lasers, a first approach of the separation time for PIV,  $\Delta t$ , must be calculated. The separation time can be calculated applying Equation

3.10, knowing the characteristic velocity of the wind tunnel,  $3 \text{ m.s}^{-1}$ , and the fact that 10 pixel of displacement is favourable for the cross correlation.

$$\Delta t = \frac{\Delta s}{u} = \frac{10M}{u} \quad (3.10)$$

$M$  is the magnification factor. This factor is calculated knowing how many meters we have per pixel. To determine this parameter, it was used a calibration plate. In the current experiments it was determined that 55 mm corresponds to 706.23 pixels. Knowing this, a first approach for the separation time of  $260 \mu\text{s}$  is obtained.

To support the description of the synchronization times procedure, in Appendix II is presented a timing diagram with the lasers and camera. The trigger for the flashlamp (laser 1) is set up for  $0 \mu\text{s}$  and it takes  $500 \mu\text{s}$  to activate. Then the Q-Switch can range between from  $170$  to  $370 \mu\text{s}$ , where  $170$  correspond to the maximum intensity of the laser. The intensity of the laser follows a gaussian curve. The peak of this curve corresponds to the minimum Q-Switch, and the maximum Q-Switch is in the right side of the gaussian curve that corresponds to a low intensity of the laser. The operation of the laser intensity must occur in the right side of the gaussian curve, e.g. between the minimum and maximum Q-Switch. The trigger for the flashlamp (laser 2) is the sum of the trigger for the flashlamp (laser 1) with the separation time. The total Q-Switch delay is the sum of flashlamp (laser 2) delay with the first Q-Switch delay. For the camera, knowing that the integration time of the first image is  $50 \mu\text{s}$ , the camera delay is the difference between the first Q-Switch delay and the integration time, divided by two.

Regarding the seeding, the system used was Aerosol Generator PivPart14 series feed with synthetic oil. To have particles that do not absorb UV (Ultraviolet) light, to not absorb the fluorescence, the oil used was DEHS oil, or, Bis(2-ethylhexyl) sebacate. The typical size of a particle is around  $1.0 \mu\text{m}$ .

### **Section 3.4.3 – *Measurements procedure***

My contribution for the work of Gian Gori and Simão Nóbrega, consisted in developing a parametric study to obtain the best combination of parameters for their PIV measurements. The objective of this test is to assess the influence of the different elements affecting the



quality of the measurements to choose the best combination. Therefore, the following parameters were analysed:

- particles concentration;
- laser intensity;
- aperture;
- separation time.

Before taking the acquisition for each parameter pointed previously, it was taken 50 images of a calibration plate and background image (without flow or particles) to remove the reflections and background light. For each test, the acquisition was of 200 images.

For the concentration, the following synchronization times (Table 3.6) were applied in the software. Three different concentration of particles were tested, and are identified as “low”, “medium” and “high”. These concentrations were set up by looking at the image. Some examples will be presented in Section 5. As it is observed in Table 3.6, is was used the maximum intensity of the laser, with a Q-Switch of 170  $\mu\text{s}$ , that correspond to 670  $\mu\text{s}$  of Q-Switch delay. The separation time,  $\Delta t$ , used was 260  $\mu\text{s}$ , and the aperture used was 4.

The laser intensity is controlled with the Q-Switch. Therefore, four different tests of Q-Switch delays, e.g., Q-Switch plus the activation time, were performed: 670, 700, 730 and 760  $\mu\text{s}$ . For this test  $\Delta t$  and aperture was the same as for the concentration test. As explained previously, changing the Q-Switch is going to influence the synchronization times in Table 3.6.

**Table 3. 6** - Synchronization times for the PIV system.

<b>Channel</b>	<b>Identification</b>	<b>Time delay <math>\mu\text{s}</math></b>
1	PIV camera	645
2	Flashlamp laser 1	0
3	Q-Switch delay 1	670
4	Flashlamp laser 2	260
5	Q-Switch delay 2	930

Different apertures of the camera were also tested: 2.8, 4, 5.6, 8 and 11. The condition for  $\Delta t$  was the same as before, and the Q-Switch delay was 670  $\mu\text{s}$ .

With the same conditions for concentration (reasonable concentration), the same Q-Switch,  $\Delta t$  and aperture, it was tested different separation times: 180, 220, 300 and 240  $\mu\text{s}$ .

## Section 4 – Uncertainty analysis

The quantification of the experimental uncertainty associated to a measurement allows the comparison under different circumstances.

It is important to distinguish the difference between the concepts of “error” and “uncertainty”. The error is associated to a single observation, where it is the difference between the “true” and the “measured” values. The uncertainty is determined for a number of experiments and represents the possible value that the error might have within a confidence interval (Anthoine et al., 2009).

In a metrology lab, measurements are carried out assuming that measurement instruments are unbiased, hence all measured values derive from the observations of the measuring instrument belong to a normal distribution (Gupta, 2012). According to this author, to perform a good uncertainty analysis it must be evaluated first the quality of the individual mean of each sample and then the quality of the variances. After this, the uncertainties can be determined, knowing that there are two types of uncertainties: the systematic and the random uncertainty.

The systematic uncertainty means that every time that a measurement is taken under the exact same conditions twice, the results are the same. For the random uncertainty, it is the other way around, e.g., under the same conditions we have different results.

In the measurements performed, there are two main sources of uncertainty:

- the uncertainty that comes from the free stream velocity, which is associated with the calibration of the wind tunnel (systematic uncertainty) and the random uncertainty coming from the stability of the free stream velocity;
- the uncertainty on the velocity measured with hot wire anemometer.

As it was mentioned before, in Section 3.1, the calibration of the wind tunnel was performed previously to this work by Zapata (2017). This author had estimated that the random uncertainty was 0.5% of the free stream velocity. Therefore, this uncertainty, associated with the wind tunnel, is not going to be analysed.

For the microphone antenna, the uncertainty is mainly coming from the calibration procedure, and this process, is still under investigation. Therefore, is not possible to present an uncertainty analysis for this technique.

According to the Lecture Series taught by Christophe Schram about “Data Acquisition and Processing” at VKI, a confidence interval of 95% and a maximum relative uncertainty of 1% can be chosen to perform the analysis of the jet mean velocity profile. According to this author, if the turbulence intensity of the jet mean velocity profile is 10%, the number of samples (N) required must be higher than 1,500. If the turbulence intensity is 20%, N must be higher than 6,000 samples. The analysis performed by this author, for the statistical estimation of the number of samples can be analysed in Figure 4.1 (Schram, 2017).

$$\bar{x} + 1.96 \frac{\sigma_x}{\sqrt{N}} - \left( \bar{x} - 1.96 \frac{\sigma_x}{\sqrt{N}} \right) < 0.01 \bar{x}$$

$$N > \left( \frac{3.92 \sigma_x}{0.01 \bar{x}} \right)^2 \simeq 15 \times 10^4 (T.I.)^2$$

$T.I. = 10\% \rightarrow N > 1500$   
 $T.I. = 20\% \rightarrow N > 6000$

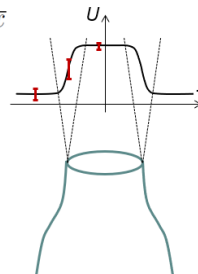


**Figure 4. 1** - Uncertainty on jet mean velocity profile (Schram, 2017).

For the uncertainty analysis performed, the same principle was used for the calculation of the minimum number of samples. However, the confidence interval chosen is 99% for a maximum relative uncertainty of 0.1%. Redoing the calculations, for a turbulence intensity of 10%, N must be higher than  $2.67 \cdot 10^5$ , and for 20% of turbulence intensity, N must be higher than  $1.07 \cdot 10^6$ .

With the confidence interval defined, the number of samples required can be calculated for each measurement, distinguishing between the calibration and the main measurements. Table 4.1 shows the parameters used to calculate the number of samples obtained for the hot wire anemometer calibration and for the measurements.

For the calibration, the sampling time was 3 seconds ( $N = 1.54 \cdot 10^5$ ), however in the data post-processing it was used only 1 second that corresponds to  $5.12 \cdot 10^4$  samples, once the value converged.

**Table 4. 1** - Parameters used for the hot wire measurements.

Variable	Calibration	Main measurements
Sampling frequency, Hz	51,200	51,200
Sampling time, s	1	60
Number of samples (N)	$5.12 \cdot 10^4$	$3.017 \cdot 10^6$

For the main measurements, with a 99% confidence interval and 0.1% uncertainty, it is observed that the number of samples acquired are higher than the minimum requirement ( $1.07 \cdot 10^6$  samples).

The sources of uncertainty for hot wire measurements come essentially from: the temperature correction,  $\delta E_{corr}^2$ , that is applied in the data post-processing (described in Section 3.2.2), the velocity measured with the hot wire anemometer,  $\delta u_{tot}^2$ , and the conversion analogue to digital (CAD),  $\delta U_{CAD}^2$ .

Is important to mention, that, there is a systematic uncertainty associated with the measurement of temperature and voltage that was neglected.

When performing an uncertainty analysis, the relation between the different components that bring uncertainty to the measurements should be done. In this work this was not performed, therefore, the uncertainty presented can be overestimated.

The final formulation to quantify the total uncertainty associated with the results for the velocity profiles can be calculated using Equation 4.1. The description to calculate each term from Equation 4.1, is in Appendix I.

$$\delta Total \left[ \frac{m}{s} \right] = \sqrt{\delta u_{tot}^2 + \delta E_{corr}^2 + \delta U_{CAD}^2} \quad (4.1)$$

The representation of the uncertainty associated to each measurement can now, be performed. In Figure 4.2 it is possible to visualize the results for the velocity profiles with the uncertainty for ZPG at Inlet position. In Appendix I, the results for the other conditions can be analysed. For the different sources of uncertainty, the one that contribute the most is the uncertainty associated with the voltage correction  $\delta E_{corr}^2$ . As an example, the uncertainties values for  $\delta E_{corr}$  range from 0.212 to 0.109 m.s<sup>-1</sup>, and the uncertainty values

for the  $\delta u_{tot}$  range from 0.0269 to 0.0489  $\text{m}\cdot\text{s}^{-1}$ , from the higher height to the bottom plate respectively.

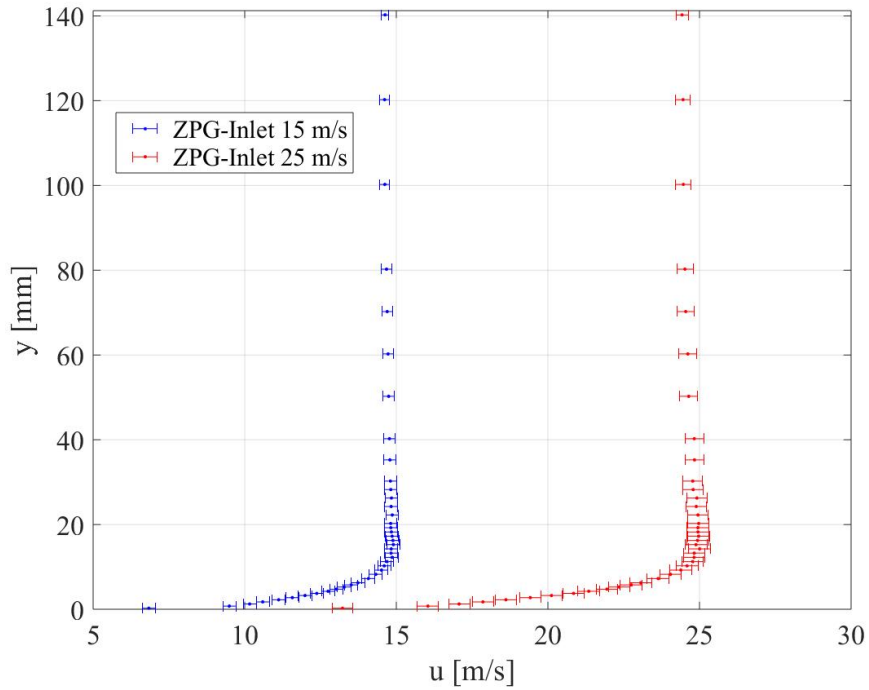


**Figure 4. 2** - Velocity profiles for 15 and 25  $\text{m}\cdot\text{s}^{-1}$  for ZPG at the Inlet position, including the estimated uncertainty.

## Section 5 – Results and discussion

This section will be divided in three subsections, first it will be presented the results for hot wire anemometer, including calibration and measurements. Afterwards, it follows a subsection with the microphone antenna results, and then the results for wall pressure models, including hot wire anemometer and microphone antenna comparison. The final subsection is dedicated to the results for PIV.

For each step, the description of the calibration and measurements procedure are explained in Section 3. All the post-processing was performed using MATLAB.

### Section 5.1 – Hot wire anemometer

As it was explained in Section 3.2.2, the first step was to perform the pressure transducer calibration. In Figure 5.1, it follows the calibration result for this equipment. The coefficients obtained for the linear regression are going to be feed into the subsequent post-processing of the hot wire anemometer.

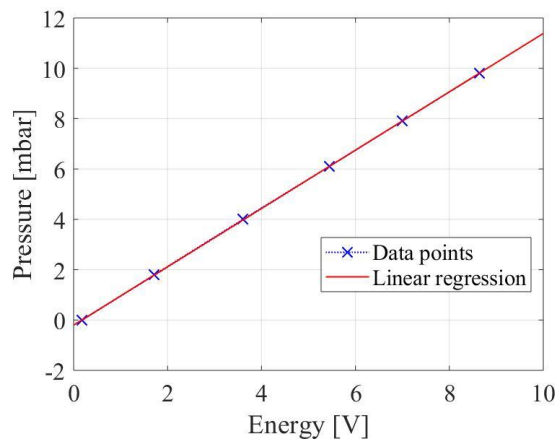


**Figure 5.1** - Results for the pressure transducer calibration.

Since the hot wire anemometer measurements were performed in different days, there is a need to perform a calibration for each day before proceeding to the measurements, once the fluid conditions change during the day (ambient pressure and temperature). It is presented only one result for the calibration, once the other ones follow the same principle (Figure 5.2).

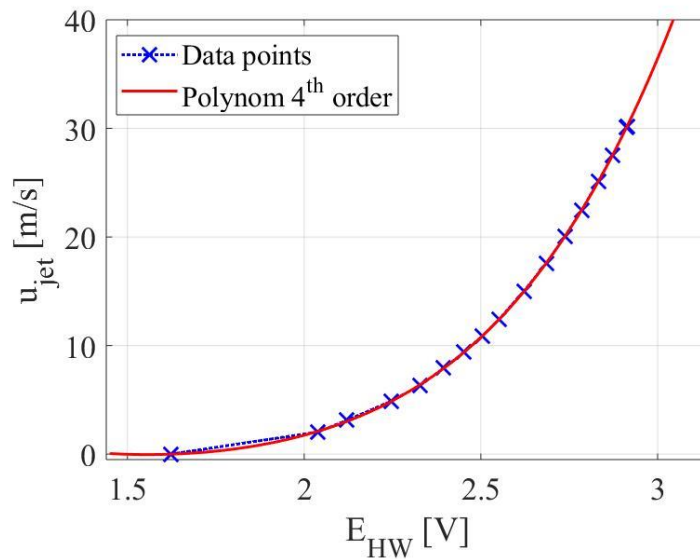


**Figure 5. 2** - Hot wire anemometer calibration results including temperature correction.

To understand the importance of the temperature correction, in Appendix III it follows, one of the calibration curves with and without this correction.

The measurements with hot wire anemometer were performed to obtain the velocity profiles and the characteristics of the turbulent boundary layer (TBL) with height, e.g. from the bottom (closest to the wall as possible) until 140 mm from the initial height of the wind tunnel.

The type of measurements performed are presented in Table 3.2, where ten conditions were accomplished. Using theodolite WILD-N3 and the Johnson block of 3 mm, Table 5.1 shows the closest distance placement for the hot wire from the bottom wall of the wind tunnel.

**Table 5. 1** - Distances measured with theodolite WILD-N3 for the hot wire position.

<b>Closest distance from the bottom wall <math>y_0</math> [mm]</b>	
<b>ZPG</b> – Inlet - 15/25 $m.s^{-1}$	0.243
<b>ZPG</b> – Station 1 - 25 $m.s^{-1}$	0.219
<b>ZPG</b> – Station 2 - 25 $m.s^{-1}$	0.300
<b>FPG</b> – Station 1 - 15/25 $m.s^{-1}$	0.260
<b>APG</b> – Station 2 - 15/25 $m.s^{-1}$	0.278



For ZPG at the Inlet, in Figure 5.3 the rescale velocity profile for 15 and 25 m.s<sup>-1</sup>, is represented, and in black colour, the wind tunnel velocity. It is observed, that the velocity measured with the hot wire anemometer is almost the same as the velocity of the wind tunnel.

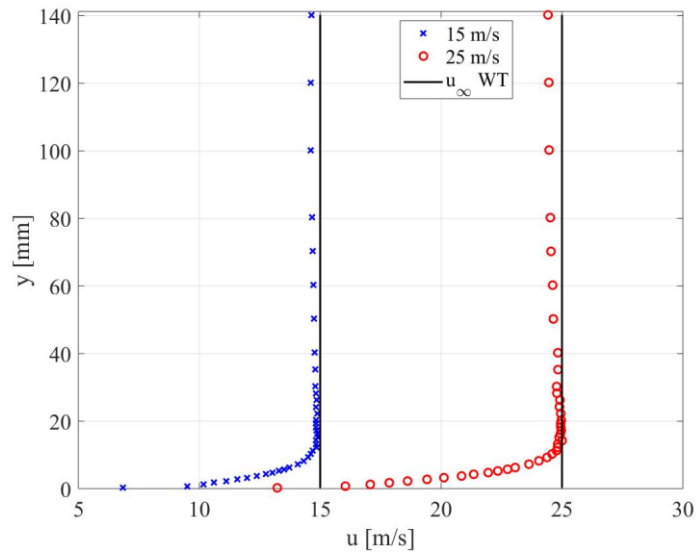


**Figure 5. 3** - Rescale velocity profiles for ZPG at inlet.

For ZPG at Station 1 and Station 2, only the measurements for 25 m.s<sup>-1</sup> were performed as it follows in Figure 5.4. It is clearly observed that, the free stream velocity measured increases when compared to the wind tunnel velocity, due to the BL thickness increase with the distance from the inlet. This increase of BL thickness and velocity also can be observed between Station 1 and Station 2.

For FPG at Station 1 (Ramp 1), Figure 5.5 represents the rescale velocity profiles for 15 and 25 m.s<sup>-1</sup>, where, the FPG is characterized with a bigger increase of the velocity, when compared with ZPG, once there is a decrease of the flow passage area.

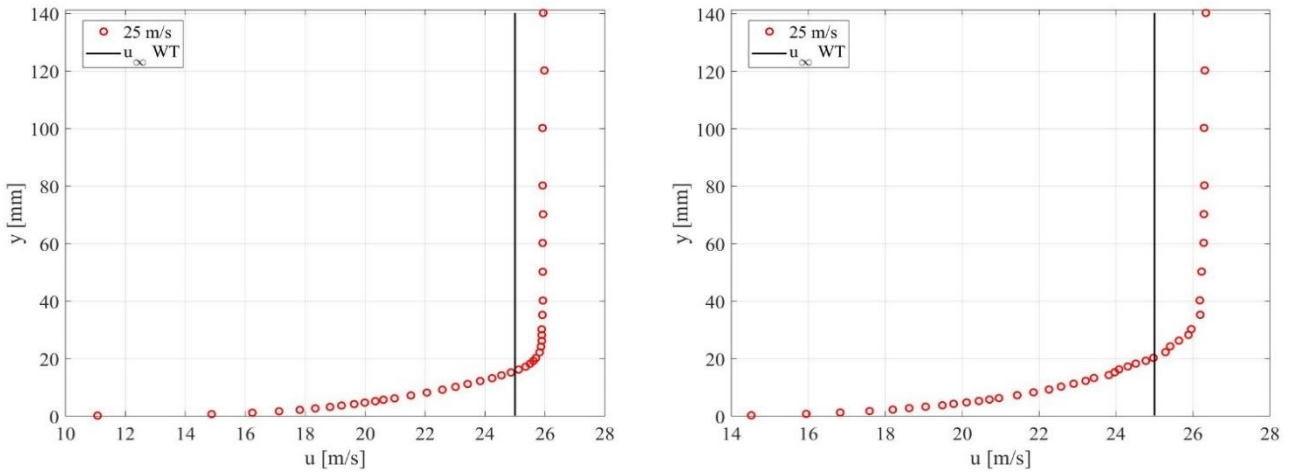


**Figure 5. 4** - Rescale velocity profiles for ZPG at Station 1 (left) and at Station 2 (right) for 25 m.s<sup>-1</sup>.

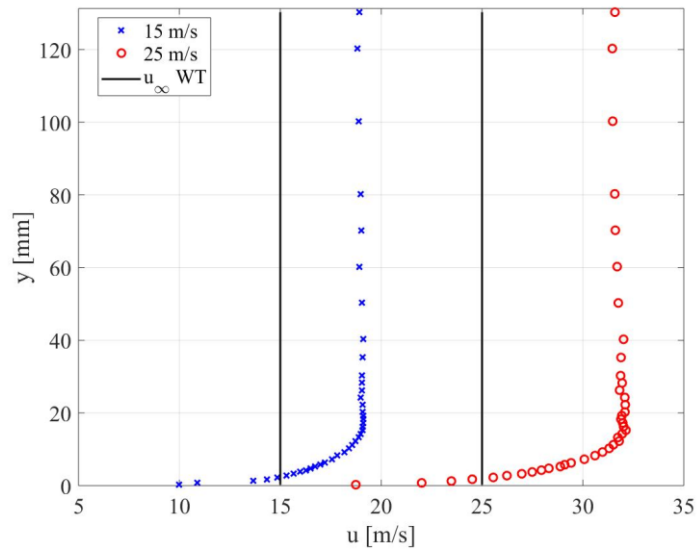


**Figure 5. 5** - Rescale velocity profiles for FPG at Station 1 for 15 and 25 m.s<sup>-1</sup>.

For Ramp 2, there are two conditions: a variable PG at Station 1 and an APG at Station 2. The characteristics of the BL for the measurements obtained for Station 1 are not going to be calculated, since the free stream velocity is variable, however the velocity profile behaviour at this station can be observed in Figure 5.6. It is observed a decreasing of velocity and an increase of the thickness of BL between Station 1 and 2.

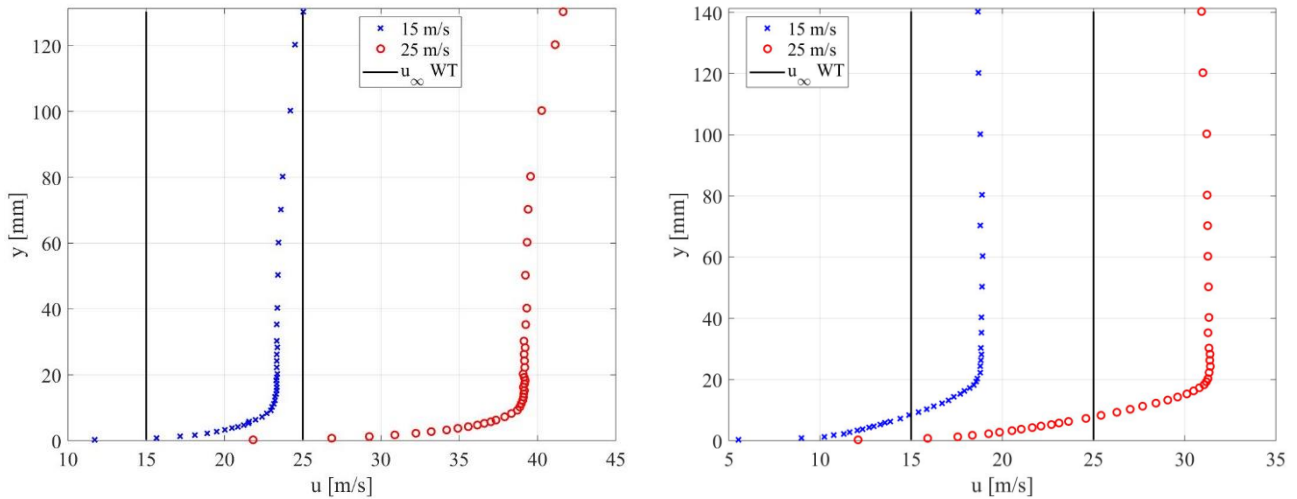


**Figure 5. 6** - Rescale velocity profiles for Station 1 (left) and Station 2 (right) with Ramp 2 for 15 and 25  $\text{m.s}^{-1}$ .

The BL velocity profile can be approximated using the  $(1/7)^{\text{th}}$  profile for fully turbulent flow. In Figure 5.7 this law for 15 and 25  $\text{m.s}^{-1}$ , for the different pressure gradients in study, is represented. For the velocities, with FPG the profiles fix well with this law, while, for ZPG-Inlet and APG, some differences below the  $(1,1)$  are observed.

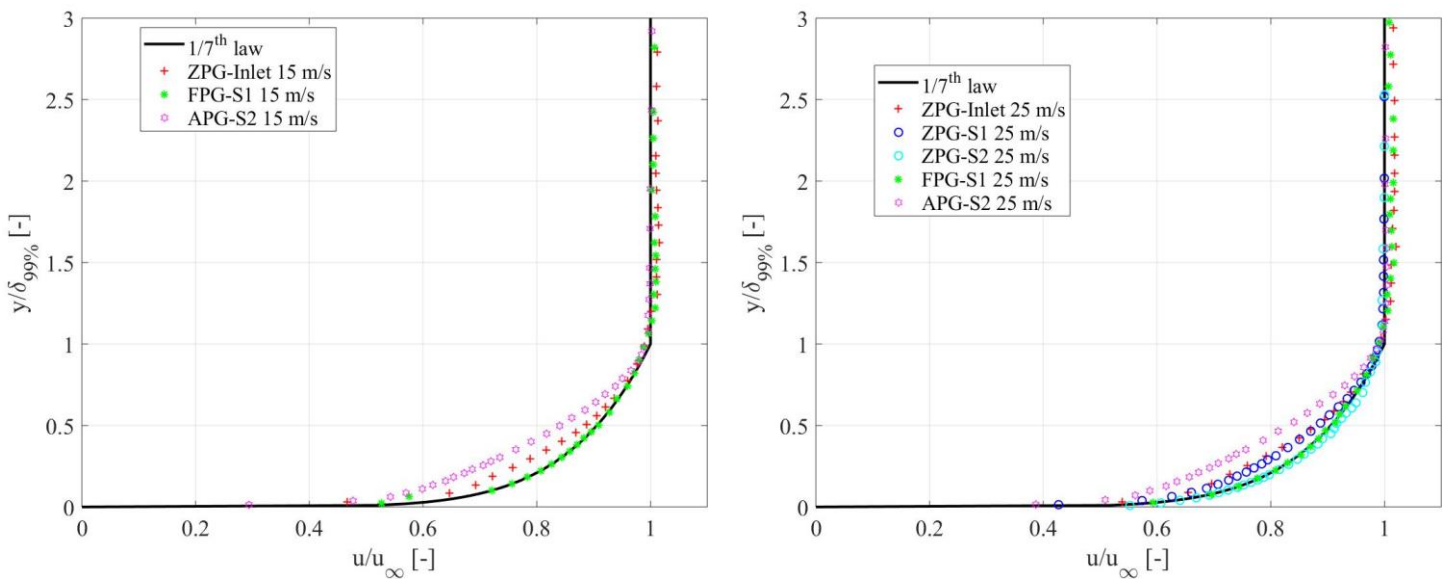
In Figure 5.8, the Spalding law is represented for the conditions in study, and it is observed that, for the “Log Region” the measurements have a similar behaviour to this law.

Figure 5.9 presents the turbulence intensity as a function of the height. A typical behaviour of turbulence intensity for all the measurements is observed, with exception of FPG and ZPG. At lowest heights, closer to the bottom wall of the wind tunnel, the turbulence intensity is higher. In almost all the conditions, a peak can be observed characteristic of the boundary layer behaviour: laminar region, transition region and turbulent region. After this point, until the higher values of height, a decreasing of turbulence intensity is observed down to the stabilization below 1% turbulence intensity.

It is also observed that the turbulence intensity for all the conditions is below 8%. However, the first two points for 15 m.s<sup>-1</sup> under FPG are not in a good agreement. This situation could be due to some interference that had happen during the measurements. Once is not possible to identify the cause, to correct this situation the measurements for this condition should be repeated to analyse the origin of the problem.

In Figure 5.10, the longitudinal turbulence spectra for the conditions in study are presented. As described in Section 2.1, the turbulence spectra were calculated assuming the Taylor's frozen turbulence hypothesis. For both spectrums, the results for the frequency under 100 Hz and above 10<sup>4</sup> Hz are not representative, once the hot wire anemometer is not capable to capture the velocity fluctuations. Analysing this figure, it is verified that higher energies are associated to low frequencies, and small energies are associated to higher frequencies.

For 15 m.s<sup>-1</sup>, it is observed higher values of turbulent energy for APG and lower values for ZPG. The same behaviour can be observed for 25 m.s<sup>-1</sup>. As expected, the turbulent energy under different pressure gradients is higher for higher velocities.



**Figure 5. 7** - 1/7th law profile for 15 and 25 m.s<sup>-1</sup> under pressure gradients.

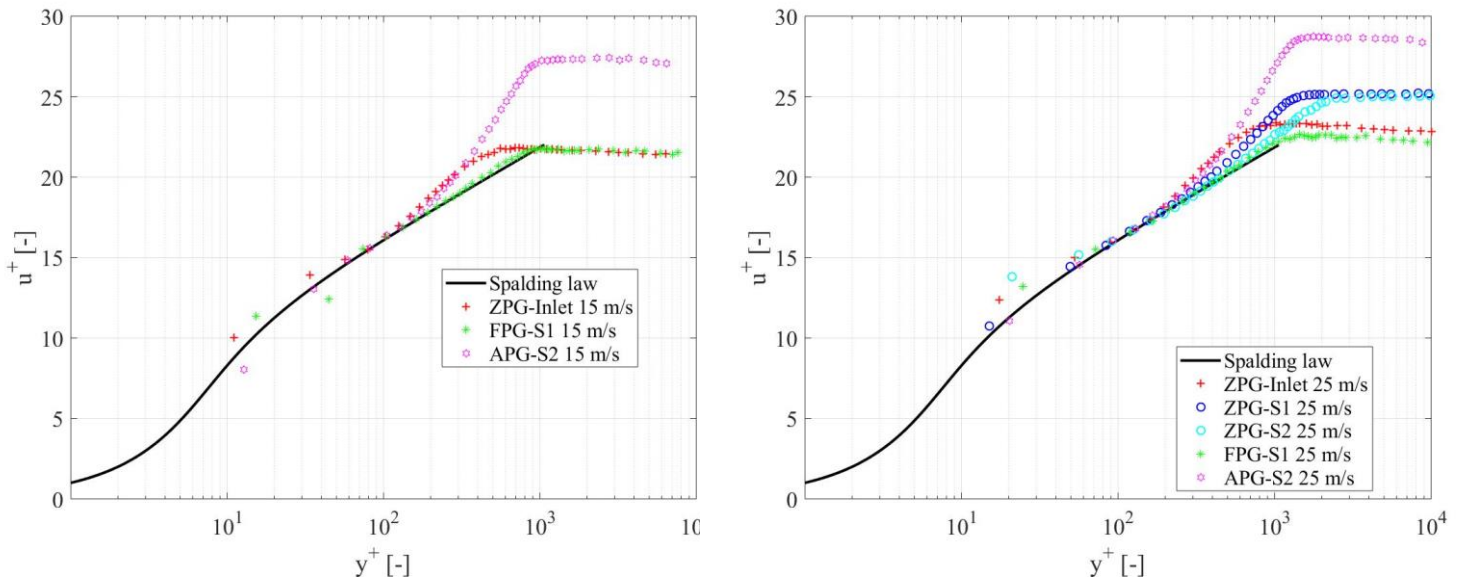


Figure 5. 8 - Spalding law for 15 and 25 m.s<sup>-1</sup> under pressure gradients.

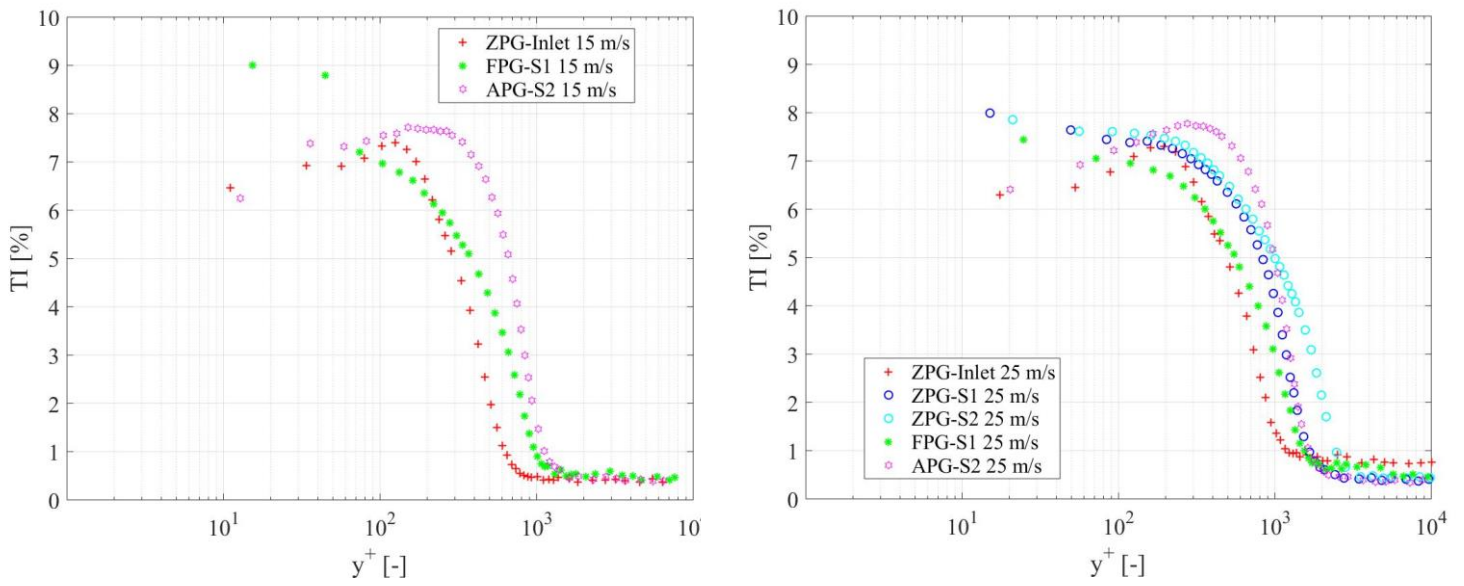
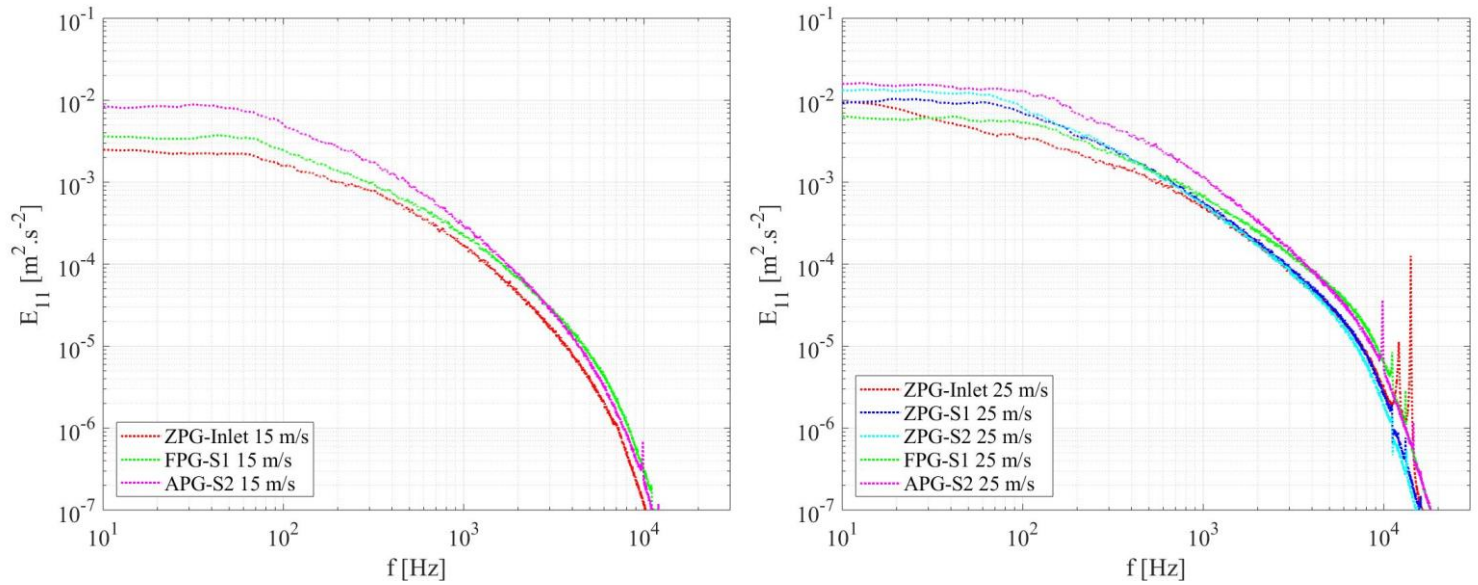


Figure 5. 9 - Turbulence intensity (%) for 15 and 25 m.s<sup>-1</sup> under pressure gradients.



**Figure 5.10** - Turbulence spectra for 15 (left) and 25 (right)  $\text{m}\cdot\text{s}^{-1}$  under pressure gradients.

Applying the mathematical formulation described in Section 2.1, the parameters used to characterize the BL can be calculated. The results can be observed in Table 5.2. As expected, for ZPG, as the distance from the inlet increases, the free stream velocity and the BL thickness increase. Between FPG and APG at different stations, the free stream velocity is similar. However, at Station 2 with APG the BL thickness is higher.

The shape factor is between around 1.4 and 1.5, characteristic of a TBL, for all the measurements. The wall shear stress and the friction velocity are higher for FPG than APG or ZPG.

**Table 5. 2** - Boundary layer characterization under velocity and pressure gradients.

		<b>ZPG</b>				<b>FPG</b>		<b>APG</b>	
		<b>Inlet</b>		<b>Station 1</b>	<b>Station 2</b>	<b>Station 1</b>		<b>Station 2</b>	
		<b>15 m/s</b>	<b>25 m/s</b>	<b>25 m/s</b>	<b>25 m/s</b>	<b>15 m/s</b>	<b>25 m/s</b>	<b>15 m/s</b>	<b>25 m/s</b>
<b><math>u_\infty</math></b>	m/s	14.67	24.52	25.94	26.29	18.94	31.59	18.86	31.25
<b><math>\delta_{99\%}</math></b>	m	9.41E-03	8.93E-03	2.00E-02	3.17E-02	1.25E-02	1.02E-02	2.06E-02	1.78E-02
<b><math>\delta^*</math></b>	m	1.51E-03	1.44E-03	3.03E-03	3.85E-03	1.69E-03	1.34E-03	4.08E-03	3.61E-03
<b><math>\theta</math></b>	m	1.03E-03	9.95E-04	2.19E-03	2.92E-03	1.20E-03	9.67E-04	2.68E-03	2.40E-03
<b><math>H</math></b>	-	1.47	1.45	1.39	1.31	1.41	1.39	1.52	1.50
<b><math>C_f</math></b>	-	4.33E-03	3.81E-03	3.16E-03	3.20E-03	4.31E-03	4.04E-03	2.68E-03	2.45E-03
<b><math>\tau_w</math></b>	Pa	0.5653	1.389	1.271	1.303	0.9331	2.431	0.5806	1.457
<b><math>u_\tau</math></b>	m/s	0.6824	1.070	1.030	1.051	0.8790	1.419	0.6897	1.093
<b><math>Re_0</math></b>	-	1007	1628	3780	5126	1519	2038	3374	5010
<b><math>\Delta</math></b>	-	6.23	6.20	6.60	8.23	7.40	7.61	5.04	4.93

### Section 5.2 – Power spectral density

The microphone antenna measurements were performed for almost the same conditions as for the hot wire anemometer measurements (with exception of the inlet position). The objective is to compare the results obtained between these two techniques.

As explained before, the data post-processing was accomplished by Professor Christophe Schram. Therefore, in this section only the results for the power spectral density,  $\Phi_{pp}(\omega)$ , for the different conditions are going to be presented. The mathematical description of how to calculate this variable is in Section 2.2.

During the post-processing, it was verified that the results were only valid for frequencies between 100 and 15,000 Hz. Therefore, the spectrums will only be represented for this range.

It was also verified that: the calculation of the free stream velocity was not the same from the center of the antenna when compared to the lateral. To verify this situation, it was programmed to perform PIV. However, due to technical issues and because of the short period, these measurements were not possible to perform.

To obtain the spectrum for the power spectral density,  $\Phi_{pp}(\omega)$ , for Goody and Rozenberg models, the results for the boundary layer characterization, obtained from hot wire anemometer were applied. The mathematical description for these models was described in Section 2.3.

Theoretically, for ZPG ( $\beta_c = 0$ ), the results for Goody and Rozenberg model should be the same. However, this was not verified when applying the mathematical formulation described in Section 2.3. Before presenting the results with the hot wire anemometer and microphone antenna, this situation will be study for ZPG at Station 2. It was chosen Station 2, once the TBL can be considered as fully developed at this position.

First, I had rewritten the Goody model (Equation 2.26) with the displacement thickness (Equation 5.1), knowing that  $\Delta = \delta/\delta^*$ . In Table 5.2, the values for the different conditions of this variable are presented. This model was compared with the Rozenberg model (Equation 2.29), where it was verified that the two models did not match, especially for higher frequencies (Figure 5.11).

$$\frac{\Phi_{pp}(\omega) u_{\infty}}{\tau_w^2 \delta^*} = \Delta \frac{3.0 \left(\frac{\omega \Delta \delta^*}{u_{\infty}}\right)^2}{\left[\left(\frac{\omega \Delta \delta^*}{u_{\infty}}\right)^{0.75} + 0.5\right]^{3.7} + \left[C_3 \left(\frac{\omega \Delta \delta^*}{u_{\infty}}\right)\right]^7} \quad (5.1)$$

This can be due to the definition of the constants applied in the Rozenberg model. Different values were changed in the parameters and changing the parameter  $A_2$  makes the Goody model be almost the same as the Rozenberg model for ZPG (Equation 5.2). The results can be observed in Figure 5.11.

$$A_2 = \min\left(3, \frac{19}{\sqrt{R_T}}\right) + 5 \quad (5.2)$$

For this specific case (ZPG with  $25 \text{ m.s}^{-1}$ ), the change of this value had worked. The fact of dealing with experimental data can be one of the causes for the discrepancies observed.



However, it must be kept in mind that the parameter applied can change depending on each case study. Indeed, Dr. Julien Christophe, Research Engineer at VKI, had performed this test for  $15 \text{ m}\cdot\text{s}^{-1}$  and concluded that the value should be 4 instead of 5 in Equation 5.2. Therefore, the wall pressure models need further investigation to improve the application of these models for other conditions.

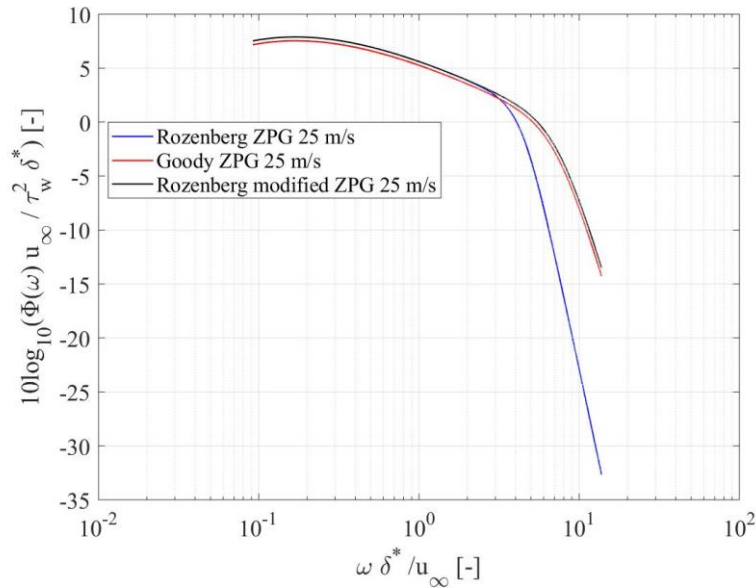


**Figure 5. 11** - Comparison between the Goody model and Rozenberg model.

In Figure 5.12 it follows the results for the 16 microphones in the center of the antenna for  $0^\circ$  rotation, with comparison with the Goody model (in black), using as an input the results from hot wire anemometer, for ZPG at Station 1 (left) and Station 2 (right).

For Station 1, the results obtained with microphone have the same behaviour and are a similar match to the results obtained with hot wire anemometer. The differences observed, are most probably related with the calibration process, something that is still in improvement.

For Station 2, the behaviour of the results is similar, however, there is a difference between these results. This situation can be due to the calibration process, that is still under investigation, or associated with the calculation of one of the parameters in the y-axis. For future work it would be advised to perform the calculation of the parameter  $C_f$  with another technique, to analyse if this difference observed is related to that.

Unfortunately, is not possible to compare the results obtained with microphone antenna for APG and FPG due to the short period to post process the data. Therefore, the validation of this results needs to be accomplished in the future.

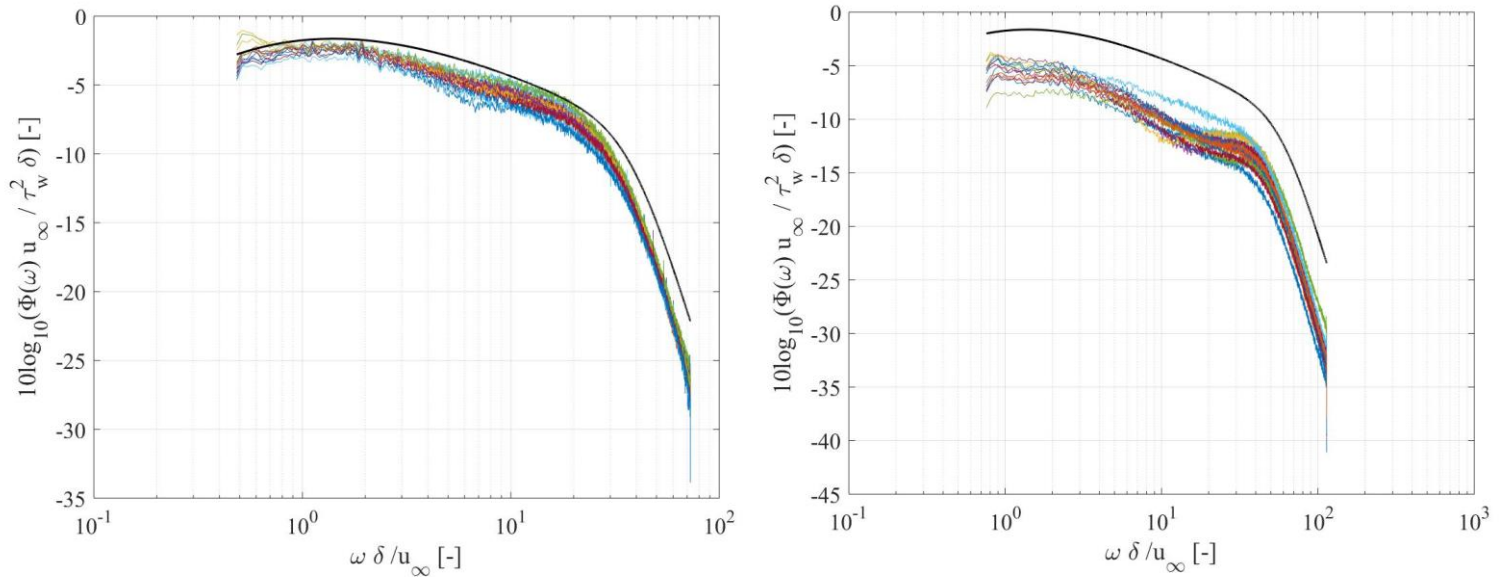


**Figure 5.12** - Comparison of the results between the microphone antenna results and the Goody model (black) for ZPG at Station 1 (left) and Station 2 (right) for 25 m.s<sup>-1</sup>.

### Section 5.3 – Particle image velocimetry

The results for this section consist essentially in presenting the best configuration of the parameters obtained with the parametric study to improve the quality of the measurements, for the work of Gian Luca Gori and Simão Nóbrega and to understand their single effect.

The data post-processing of PIV was performed with DaVis 8.2.2. To estimate the quality of the test measurements, it should be use the signal to noise ratio parameter (SNR), but DaVis do not give this value. Therefore, instead of using this parameter, it was used the “peak ratio” parameter. According to the software manual, the peak ratio  $Q$ , is defined as:

$$Q = \frac{P1-min}{P2-min} > 1 \quad (5.3)$$

where,  $min$  is the lowest value of the correlation plane and  $P1$  and  $P2$  are the peak heights of the first and second highest correlation peak (Figure 5.13). Thus, the peak ratio calculated with Equation 5.3 is the relative ratio, relative to the common correlation background to

compensate, e.g. a general image background level or background noise. If there is no second highest peak, the peak ratio is set to 100.

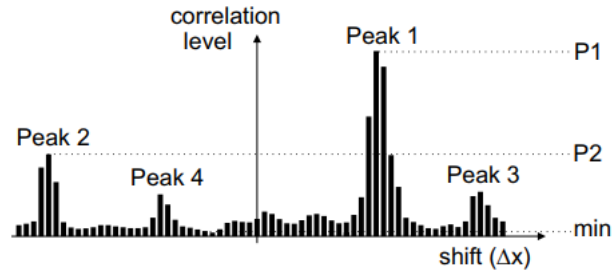


Figure 5.13 - Definition of peak ratio according to DaVis software manual.

The calibration plate used is characterized with a distance between points of 5 mm and a diameter of 2 mm. For the post-processing of the calibration plate, the software is able to detect the position of all the dots (Figure 5.14), where it put them in a straight line applying a 3<sup>rd</sup> order polynomial function (Figure 5.15).

The background image was used to subtract to the measurement images (e.g. the different conditions for the parametric study), to reduce the background noise.

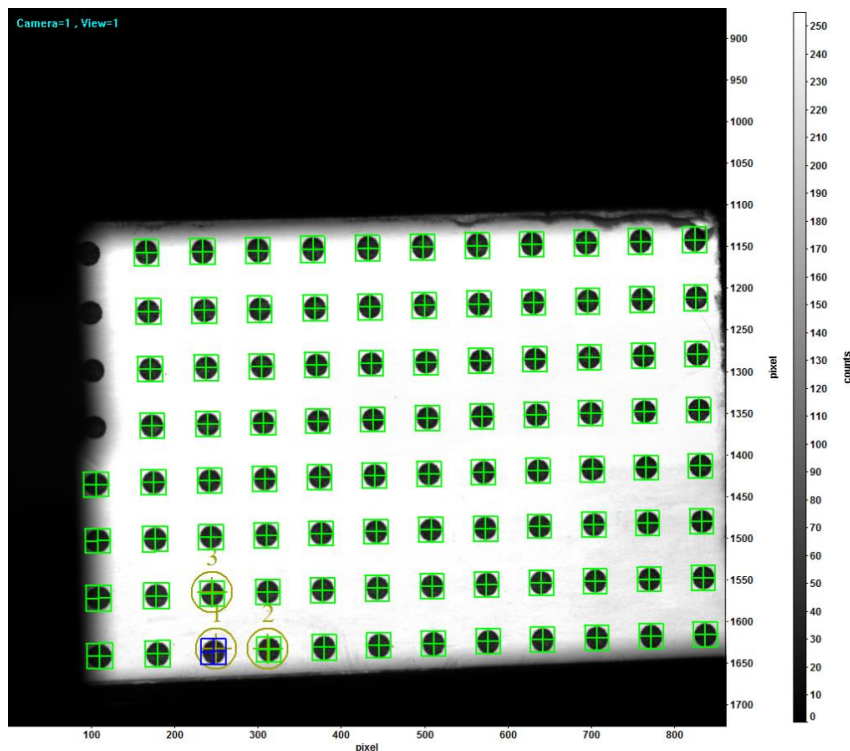


Figure 5.14 - Identification of the points from the calibration plate with DaVis.

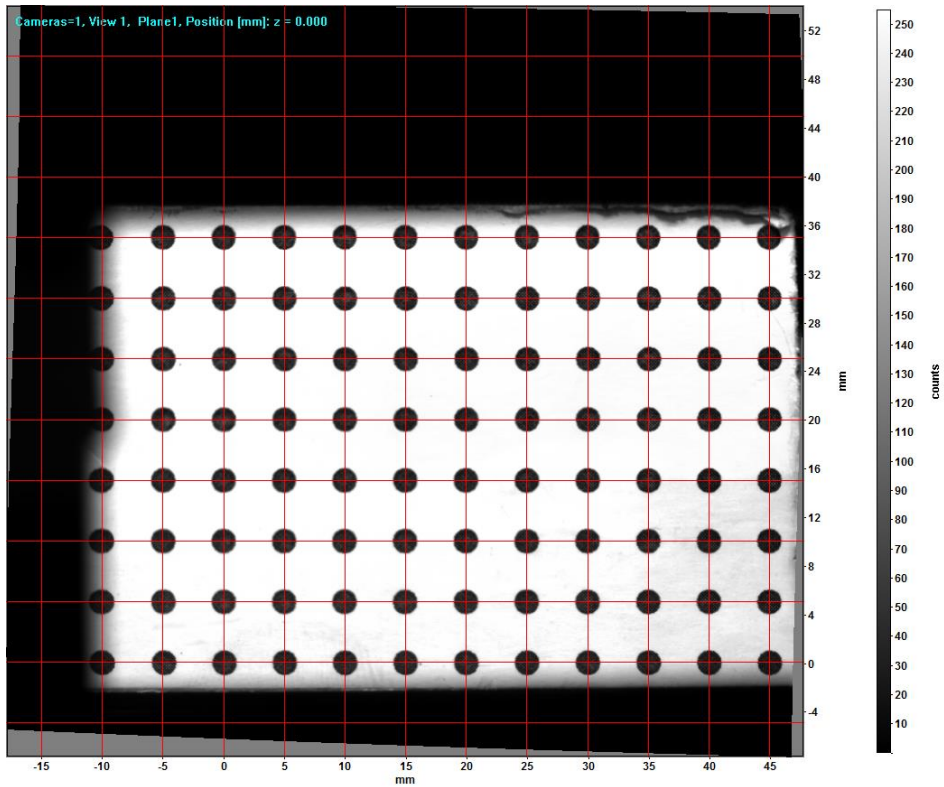


Figure 5.15 - Result for the calibration plate.

In Table 5.3 is presented the results of peak ratio for the different test measurements performed.

Table 5.3 - Peak ratio results for the different parameters.

<b>Concentration</b>	Low	75.562
	Medium	80.885
	High	79.118
<b>Q-Switch + activation time [μs]</b>	670	80.414
	700	81.248
	730	79.934
	760	77.557
<b>Aperture</b>	2.8	79.904

	4	75.152
	5.6	77.652
	8	75.872
	11	71.862
<b>Separation time [<math>\mu</math>s]</b>	180	73.568
	220	73.387
	300	75.798
	340	75.743
	260	75.152

Analysing the values in Table 5.3, and the images taken with the PIV camera, the best configuration is: a concentration of particles between the “high” and “medium” levels (Figure 6.15), a Q-Switch delay of 700  $\mu$ s, an aperture of 4 and a separation time between 300 and 340  $\mu$ s. In Figure 5.15, the reflection of the bottom plate is probably due to the material used in the wind tunnel.

It was chosen as best parameter, an aperture of 4 and not 2.8, because the focus of the images in the upper part and sides was not good enough with 2.8. The fact of obtaining a higher peak ratio for 2.8 of aperture is related with the higher intensity of light, where the particles are better distinguished, but the focus decrease. When analysing the peak ratio for the apertures, it is observed a decreasing until the 4 and increasing again for the 5.6. This result should be analysed carefully, because the images taken for the different apertures show a better result for the aperture 4.

Knowing that the acquisition time since the trigger of the first flashlamp until Q-Switch is 500  $\mu$ s (activation time) and that the Q-Switch can range from 170 until 370  $\mu$ s, it means that having a Q-Switch delay of 700  $\mu$ s, it means that the Q-Switch is 200  $\mu$ s, meaning that the operation the operation of the laser intensity is occurring in the right side of the gaussian

curve for the laser intensity, characterized as being in the range for the optimum laser operation.

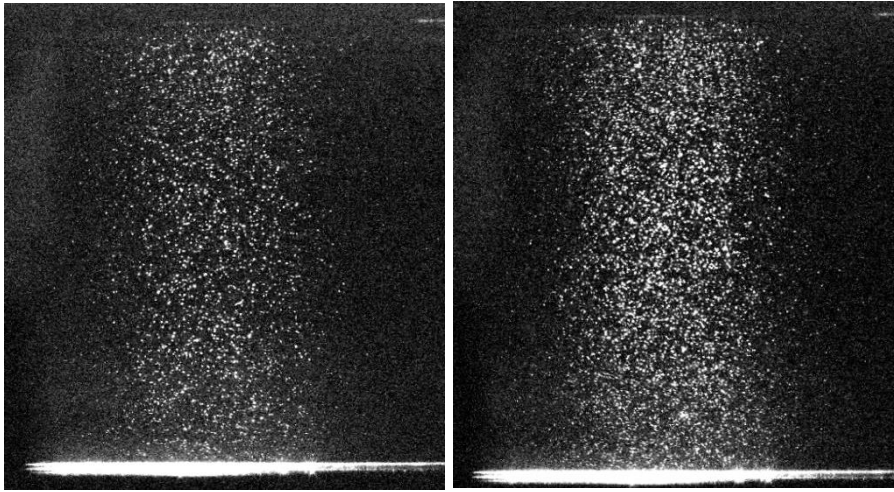


**Figure 5. 16** - Images of the particles concentration for medium (left) and high (right).

In Section 3.4, a first approach for the separation time obtained was  $260 \mu\text{s}$ , however, after the parametric study it was observed that, a separation time between  $300$  and  $340 \mu\text{s}$  is the optimum configuration. The accuracy of PIV measurements can be increased by increasing the separation time between the exposures at least within certain limits. However, for high values of separation time the measurement noise increases (Raffel et al., 2007). According to Antal and Tagadó (2010), a typical value for the separation time is  $300 \mu\text{s}$ .

## Section 6 – Urban atmospheric boundary layer

This subsection aims to introduce a literature review about the subject of fluid dynamics to environmental applications, specifically, atmospheric applications.

The field of fluid dynamics study liquids and gases that are in rest or motion, with the objective to determine the effects that they produce on the boundaries defining them, or, alternatively, the action that those boundaries produce on them (Oliveira and Lopes, 2016). Fluid dynamics have a wide variety of applications, ranging from the aerodynamics, aerothermodynamics and aeroacoustics of spacecraft, to turbomachinery for their propulsion and for other applications such as energy conversion, to environmental aspects like dispersal of airborne particles, aerosols or gases in the atmosphere and in urban areas, to industrial applications involving two-phase flows, nano-particles, heat and mass transfer including cryogenic applications, or to the flow of air and aerosols in human lungs (VKI, 2016).

Regarding environmental applications, the basic principles of fluid dynamics can be used to establish criteria necessary for simulation of the Atmospheric Boundary Layer (ABL) by the Boundary Layer (BL) formed in a wind tunnel (Cemak, 1973).

### Section 6.1 – Atmospheric boundary layer

According to Stull (1988), the earth's surface is a boundary on the domain of the atmosphere, where the transport processes modify the lowest 100 to 3000 m of the atmosphere, creating what is called the boundary layer (BL) or atmospheric boundary layer (ABL) and the remaining part of the troposphere is called the free atmosphere (Figure 6.1).

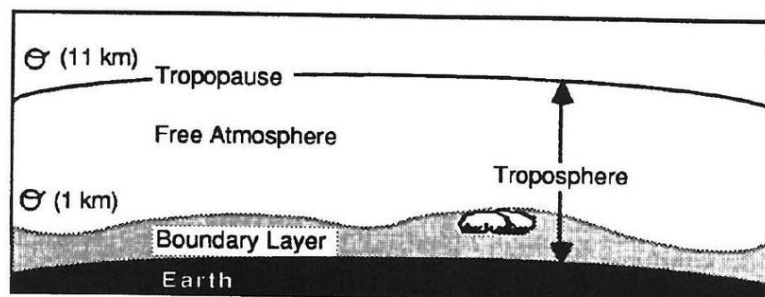


**Figure 6.1** - Schematic representation of the troposphere division into free atmosphere and boundary layer (Stull, 1988).

The ABL can be defined as the “part of the troposphere that is directly influenced by the presence of the earth's surface and responds to surface forcings with a timescale of about an

hour or less". These forcings can be: frictional drag, heat transfer, pollutant emissions, evaporation and transpiration and terrain that can cause flow modification (Stull, 1988).

The thickness of the ABL is variable in time and space and can range from hundred meters to a few kilometers. A key characteristic to take into consideration to define the ABL is the diurnal temperature over land. The diurnal temperature variation is not caused by direct forcing of solar radiation on the ABL, because little solar radiation is absorbed in the ABL. Most is transmitted to the ground where typical absorptivities are of the order of 90%, resulting in absorption of much of the solar energy. It is the ground that warms and cools in response to the radiation, which in turn forces changes in the ABL via transport processes (e.g. turbulence).

Over oceans, the ABL depth varies relatively slowly in time and space, and a slowly varying sea surface temperature means a slowly varying forcing into the bottom of the ABL. Therefore, most changes in ABL depth over oceans are caused by synoptic and mesoscale processes of vertical motion and advection of different air masses over the sea surface (Stull, 1988).

When the characteristic Reynolds number of a fluid motion exceeds a critical value, the state of the motion becomes turbulent, where, in the atmosphere, these conditions prevail usually in the ABL, which is the atmospheric region of greatest interest to meteorology. This variable is the greatest interest once it is one of the important transport processes.

Usually turbulence consists of many different size eddies superimposed on each other, where the relative strengths of these different size eddies define the turbulence spectrum. The turbulence of a BL is mostly generated by forcings from the ground, such as: solar heating of the ground during sunny days causes thermals of warmer air to rise (large eddies); frictional drag on the air flowing over the ground causes wind shears to develop, which frequently become turbulent; obstacles like trees and buildings deflect the flow causing turbulent wakes adjacent to and downwind of the obstacles.

Other characteristics that can be important to define the BL are: friction, dispersion, winds and vertical transport. Therefore, according to Stull (1988), the definition of the BL includes a statement about one-hour time scales, where this does not imply that the BL reaches an equilibrium in that time, just that alterations have at least begun.



Air flow or wind can be divided into three broad categories, mean wind, turbulence and waves. The turbulence and waves can exist in the BL, separately or in the presence of any others. The transport of quantities (moisture, momentum and pollutants) is dominated in the horizontal by the mean wind and in the vertical by turbulence.

Therefore, mean wind is responsible for very rapid horizontal transport or advection. Waves are frequently observed in the nighttime BL and transport little heat, humidity, and pollutants. However, waves are effective transporting momentum and energy. These waves can be generated locally by mean-wind shears and by mean flow over obstacles, and can also be propagate from some distant sources (e.g. thunderstorm, explosion, etc.) (Stull, 1988).

A common approach for studying either turbulence or waves is to split variables such as temperature and wind into a mean part and a perturbation part. The mean part represents the effects of the mean temperature and mean wind, while the perturbation part can represent either the wave or the turbulence effect that is superimposed on the mean wind (Stull, 1988).

The ABL has a huge impact on human beings directly and indirectly (via its influence on the rest of the weather), and the following list presents some examples (Stull, 1988):

- “People spend most of their lives in the ABL”;
- “Daily weather forecasts of dew, frost, and maximum and minimum temperatures are really ABL forecasts”;
- “Pollution is trapped in the ABL”;
- “Fog occurs within the ABL”;
- “Turbulent transport of momentum down through the ABL to the surface is the most important momentum sink for the atmosphere”;
- etc.

According to World Health Organization (WHO, 2016), clean air is a basic requirement of human health and well-being. However, air pollution, both indoor and outdoor, is recognized as a threat to human health, even at low doses, since it is associated with increase of mortality and morbidity worldwide.

The emission of air pollutants can have two different sources, anthropogenic and natural, and they may be either emitted directly (primary pollutants) or formed in the atmosphere

(secondary pollutants). Estimates of the health impacts related to exposure to air pollution indicate that PM<sub>2.5</sub> concentrations in 2014 were responsible for about 428,000 premature deaths originating from long-term exposure in Europe (EEA, 2017). Following the WHO predictions 3.7 million of people have died prematurely in 2012 due to ambient air pollution, caused by the burning of solid fuels (WHO, 2014), while the most recent Global Burden of Disease study estimates that air pollution, indoor and outdoor combined, was the cause of 5.5 million premature deaths globally in 2013 (URL 5).

Air pollution keeps having significant impacts on human health of the European population, especially in urban areas, once around 75% of population live in these areas (URL 2). The pollution levels are often high, because of the poor dispersion conditions and high density of pollution sources (Hertel et al., 2001). It also has considerable economic impacts, cutting lives short, increasing medical costs and reducing productivity through working days lost across the economy. The most serious pollutants in Europe in terms of harm to human health are particulate matter (PM), NO<sub>2</sub> and ground-level O<sub>3</sub> (EEA, 2017).

According to the OECD (2016), global air pollution related healthcare costs are projected to increase from USD 21 billion in 2015 to USD 176 billion in 2060. In 2016, the annual number of working days lost, which affect labour productivity, was around 1.2 billion at the global level, and by 2060 it is projected to be 3.7 billion (OECD, 2016).

According to EEA (2017), effective action to reduce the impacts of air pollution requires a good understanding of its causes: i) how pollutants are transported and transformed in the atmosphere, ii) how the chemical composition of the atmosphere changes over time, and iii) how they affect humans, ecosystems, the climate, and subsequently society and the economy. Several policies, plans and programmes have been implemented to reduce air pollution to prevent the effects on human health. In this sense, Air Quality Directive (Directive 2008/50/EC) establishes several objectives that must be fulfilled by the European Member States.

Therefore, the experimental and numerical techniques that are applied in fluid dynamics (e.g. hot wire anemometer, PIV, computational fluid dynamics (CFD), etc.) can be extremely useful for the research of the ABL. This type of study can be accomplished for different scales (global, regional, mesoscale and local scale) depending on what is the problem in

analyse, but with the aim of improving the air quality to protect human health and ecosystems.

Finally, the ABL, has a very close relation with human activity (Sládek et al., 2004), and the development and maintenance of the ABL plays a key role in the distribution of atmospheric constituents, especially in a polluted urban area, where the ABL has a direct impact on the concentration and transformation of pollutants (Pino et al., 2004).

The study and understanding of the urban boundary layer (UBL) and the interactions that it has with human activities is highly important, once it has a huge influence on human's well-being.

### Section 6.2 – Urban boundary layer

The term urban boundary layer (UBL) is used when dealing with the part of the atmosphere in which most of the population lives (Barlow, 2014). The UBL can be divided in two sub-layers: the mixed-layer and the surface layer (SL) (Figure 6.2). The characteristics of the flow in the UBL are associated with the large scale, inhomogeneous roughness which characterises the city centre (Ricciardelli and Polimeno, 2006).

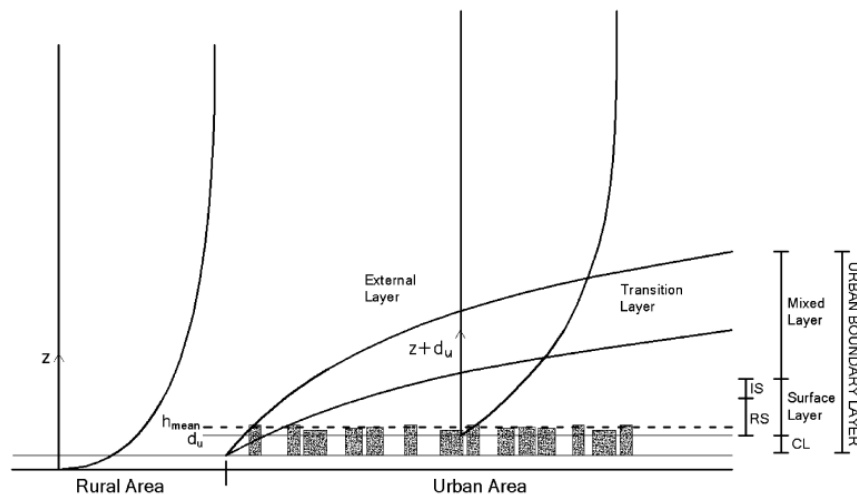


Figure 6. 2 - Wind flow layers in the Urban Boundary Layer (UBL) (Ricciardelli and Polimeno, 2006).

The surface layer (SL) extends up to an elevation of approximately 10% of the total depth of the boundary layer (BL). In the SL, the flow is affected by the local geometry, i.e. the

one-point characteristics of the flow can be quite different from their spatially averaged values. The SL can be separated in the inertial sublayer, roughness sublayer and canopy layer (CL) (Oke, 2006).

The characteristics of the flow in the roughness sublayer are dependent on the building arrangement. In this case, is common to use the following two parameters: uniformity of the building height and the building aspect ratio (ratio of the average building height to the average street width ( $H/W$ )), where the last one can have three different types of behaviour (Ricciardelli and Polimeno, 2006):

- Isolated roughness flow:  $H/W < 0.3$  the aerodynamics of the isolated building dominates;
- Wake interference flow:  $0.3 < H/W < 0.65$  the aerodynamics interference between buildings take place;
- Skimming flow:  $H/W > 0.65$  the case of densely distributed, medium to high rise buildings.

Regarding the last type (skimming flow), a defined average canopy height ( $h_{mean}$ ) can be found, which separates the surface layer into an upper part (inertial sublayer and roughness sublayer) and a lower part, termed canopy layer (CL). According to Ricciardelli and Polimeno (2006), in the case of skimming flow, a displacement height  $d_u$  is found, which is the elevation at which the mean wind speed profile tends to zero. The value of  $d_u$  is in the range of  $2/3 \cdot h_{mean}$  to  $3/4 \cdot h_{mean}$ , even though larger values of  $0.92 \cdot h_{mean}$  have been found from full-scale measurements.

Within the roughness sublayer, the flow is highly spatially dependent (Figure 6.3), where the turbulence can dominate the mean flow and has different characteristics from the flow in the inertial sublayer, where the turbulence is homogeneous, and fluxes vary little within height (Barlow, 2014).

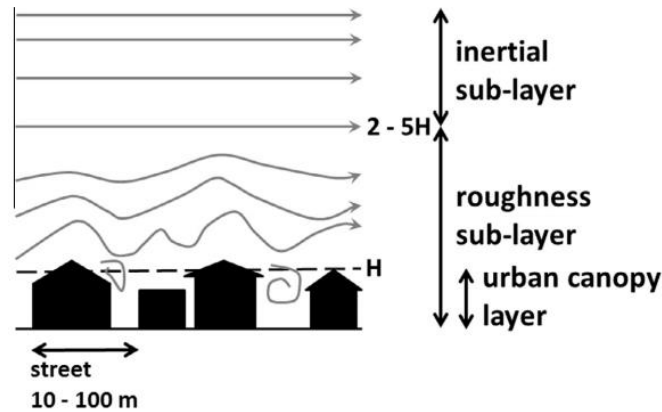


**Figure 6. 3** - Schematic diagram of roughness sublayer, inertial sublayer and canopy layer. Grey arrows indicate streamlines and dashed line indicates mean building height,  $H$  (Barlow, 2014).

The canopy layer (CL) is defined as the layer up to mean roof height (Barlow, 2014). In the CL, the flow is almost completely dominated by street geometry and building and obstacles height distribution and little affected by the characteristics of the flow in the upper layers. It is important to know and understand the flow characteristics in the CL, which influences (Ricciardelli and Polimeno, 2006):

- The analysis of the pollutants diffusion;
- The evaluation of the wind comfort at pedestrian level;
- The characterization of the wind loading of small to medium size structures in the urban environment.

Besides the vertical influence that characterizes the different sub-layers with height, in the UBL, horizontal scales can also be defined: street (10-100 m), neighbourhood (100-1000 m) and city (10-20 km). According to Barlow (2014), these can be interpreted as scales on which the urban morphology becomes heterogeneous.

Barlow (2014) states that, the UBL structure is determined not only by urban surface characteristics, but also by mesoscale thermal circulations, mesoscale referring to a scale of 10-100 km.

By day and with weak synoptic forcing (i.e. low wind and sunny conditions) buoyant up-draughts over the hotter urban surface can induce an urban thermal circulation. Coastal cities are subject to sea/land breezes due to regional scale land-sea temperature contrasts. The

urban thermal circulation may even enhance the sea breeze due to stronger up-draughts over the warmer urban surface.

Similarly, cities in mountainous terrain may experience up-slope flow due to solar heating of the slopes and down-slope flow due to the density currents at night. In flat terrain at night, a regional scale low level jet may be generated due to the stable rural surface layer and may interact with the nocturnal UBL.

In all cases except for the urban thermal circulations, the urban area does not drive the flow, and the UBL structure will be modified due to processes acting not at city but at regional scale.

Summarizing, the forcing, which drives the evolution of the ABL, are the heat and moisture surface fluxes that accounts for 70% and the entrainment flux, i.e., warmer and dryer air that enters in the ABL from the free atmosphere. These two forcing mechanisms critically depend on some mesoscale process, such as sea breeze or mountain drainage (Pino et al., 2004).

### **Section 6.3 – *Outdoor pedestrian comfort***

According to Stathopoulos (2004), the outdoor human comfort in an urban climate may be affected by a wide range of parameters, including:

- wind speed;
- air temperature;
- relative humidity;
- solar radiation;
- air quality;
- human activity;
- noise;
- clothing level;
- age;
- etc.

The quality of open urban spaces has received a lot of attention in recent years, and there is a broad recognition that microclimate conditions contribute to the quality of life in cities, both from the economic as well as from the social viewpoint (Stathopoulos, 2004).

When developing a study in an urban area, depending on the objectives of that study, all the variables that can affect human comfort have to be analysed, including the relation with each other. In the literature review of this report, only the wind speed and air quality are going to be described, although the other parameters are important and should be taken into consideration, when performing outdoor pedestrian comfort research.

Several criteria have been developed in the wind engineering community to evaluate only the wind induced mechanical forces on the human body and the resulting pedestrian comfort and safety. According to Stathopoulos (2004), there are significant differences among the criteria used by various countries and institutions to establish threshold values for tolerable and unacceptable wind conditions even if a single parameter, such as the wind speed is used as criterion. The main difference is in the assumption of the duration that is necessary for a certain uncomfortable wind speed to become problematic (Adamek et al., 2017).

In this report, only one methodology is going to be presented, the “Beaufort scale”, however there are other ones, such as, the ones applied by Adamek et al. (2017), Weerasuriya et al. (2018), etc.

When a study about pedestrian winds (Adamek et al., 2017) and air quality (Amorim et al., 2013b) is performed, the following information is needed:

- Meteorological data of specific location to determine the probability of effects;
- Aerodynamic information (for example, interaction between building and wind, or the effects of vegetation, etc.);
- Emissions of pollutants;
- Concentrations of pollutants in the air;
- Geography;
- Comfort criterion.

The wind affects comfort through pressure effects and particle transport. The different effects that wind can cause (e.g. resistance to walking, buffeting of the body, carrying objects, etc.), begin at different wind speeds. Their threshold velocities suggest the onset of

various types of discomfort and perhaps the basis for some wind comfort criteria (Arens and Ballanti, 1977).

To characterize the effects of the wind on human comfort is common to use the Beaufort scale (Table 6.1).

Another characteristic to take in consideration about the wind at pedestrian levels, is the turbulence, which is perceived as a varying velocity, as eddies. The intensity of turbulence for any given wind speed varies from place to place but tends to be greater in urban or built-up surroundings than in open countryside (Arens and Ballanti, 1977).

Therefore, the properties of an approaching wind such as its wind speed, turbulence intensity, and direction are important for evaluating the pedestrian-level wind field in an urban area. Thereby, when a wind flow with high ambient speed strikes a building, it tends to generate windy areas around it near the ground, causing discomfort. On the other hand, highly intense turbulence has advantages, for example, it increases the velocity of the horizontal wind component near the roof of a building, strengthening the street-canyon vortex, facilitating the removal of air pollutants from a street canyon (Weerasuriya et al., 2018).

**Table 6. 1** - Summary of wind effects according to Beaufort scale (Arens and Ballanti, 1977).

Beaufort number	Description	Wind (m.s <sup>-1</sup> )	Effects
0	Calm	0	Calm.
1	Light air	0 - 1	No noticeable wind; direction shown by smoke.
2	Light breeze	2 - 3	Wind felt on face; newspapers become difficult to read.
3	Gentle breeze	4 – 5	Wind extends light flag; hair is disturbed; clothing flaps.
4	Moderate breeze	6 – 7	Dust, dry soil, and paper raised; rain and sleet driven; hair disarranged.
5	Fresh breeze	8 – 10	Force of wind felt on body; drifting snow becomes airborne; limit of agreeable wind on land.
6	Strong breeze	11 – 13	Umbrellas hard to use; difficulty walking and standing; wind noise in ears unpleasant; windborne snow above head height (blizzard).
7	Near gale	14 – 16	Strong inconvenience felt when walking.
8	Gale	17 – 20	Generally, impedes progress; great difficulty with balance in gusts.
9	Strong gale	21 – 24	People blown over by gusts; slight structural damage occurs; slate blown from roofs.
10	Storm	25 - 28	Seldom experienced on land: trees broken or uprooted; considerable structural damage occurs.



The effects of obstacles on outdoor air quality and wind comfort depend on the shape, size and orientation of a building, as well as, its interaction with the surrounding buildings (Fan et al., 2017).

Making the relation with air quality, when the wind velocity is low, uncomfortable conditions and insufficient removal of traffic exhaust gases is dominant, while with high wind velocity leads to uncomfortable or even dangerous conditions for pedestrians, but this condition promote pollutant dispersion. Some type of buildings or street configurations (e.g. high-rise buildings or narrow street canyons) may induce strong winds, which cause discomfort and dangerous conditions (Fan et al., 2017). This problem aggravates in deep street canyons, where tall buildings are lining along narrow streets with considerable amount of airborne pollutants being emitted by vehicles (Fan et al., 2017) and residential wood combustion (Borrego et al., 2010).

The effect of the vegetation can also be taking into consideration in these studies, since it modifies the wind turbulent flow dynamics and have influence over the dispersion of pollutants and, consequently influencing air quality management (Amorim et al., 2013b).

Within the urban space, the scale typically used in this type of studies is a local scale. There are two types of tools that can be used: experimental approaches and numerical modelling simulation. As mentioned previously, the experimental approaches are conducted in wind tunnels, with the application of similar conditions as in the urban space in study, where it is used advanced experimental techniques, such as, hot wire anemometer, microphone antenna, particle image velocimetry, etc., to perform the research. To conduct the numerical simulations of the turbulent flow dynamics and the air quality modelling are accomplished using Computational Fluid Dynamics (CFD) models (Amorim et al., 2013a).

CFD models rely in time-dependent numerical simulations and are very useful to well describe turbulent structures with complex geometries, but they have the disadvantage of being very time consuming due to the required accuracy of spatial and temporal discretization, requiring high computation power (Juvé et al., 2015).

Direct Numerical Simulation (DNS) and Large Eddy Simulations (LES) are time-dependent Navier-Stokes computations, which provide a three-dimensional solution. According to Juvé

et al. (2015), in DNS, the numerical mesh must resolve all the turbulent scales from the largest ones to the ultimate Kolmogorov scale, where viscosity effects become dominant. In LES, only the most energetic scales are resolved, and the influence of smaller scales are typically modelled using a turbulent viscosity approach. LES are an intermediate technique between the direct simulation of turbulent flows and the solution of the Reynolds-averaged equations (Piomelli, 2018).

Therefore, DNS is exact as no modelling of turbulence is needed, but extremely demanding in terms of computational power and thus limited to relatively low Reynolds number flows, whereas LES is less demanding and thus can be applied to flows that are more realistic.

Beside these techniques, steady-state Reynolds Averaged Navier Stokes (RANS) and unsteady RANS (URANS) computations are performed routinely and can estimate accurately the global flow parameters at a reasonable computational cost (Juvé et al., 2015). However, these techniques, are a statistical approach of the eddies, describing the evolution of the mean quantities (Piomelli, 2018).

According to Piomelli (2018), recently, hybrid methods have become more widely applied, especially for the simulation of massively separated flows; the most widespread of these methods being the Detached-Eddy Simulation (DES). In DES the attached BL is modelled using the unsteady RANS approach. After separation, the LES approach is used. This allows the calculation to capture the instability of the shear layer, and the development of the coherent structures in the wake, with more accurate prediction of the unsteady forces and of the sound emission than can be obtained by steady or unsteady RANS computations.

The use of CFD has been increasing over time related to several topics including air quality management, for example, to study the aerodynamic effects of trees on urban air pollution dispersion (Amorim et al., 2013b), pedestrian level wind assessment (Adamek et al., 2017), wind comfort (Fan et al., 2017), etc.

## **Section 7 – Conclusions and recommendations**

This section aims to presents the main conclusions of the work performed at VKI, and in Section 7.2 it follows some recommendations for future work.

### **Section 7.1 – Conclusions**

This internship had two main objectives consisting in gain experience for the application of several experimental techniques applied in the field of fluid dynamics, through the application of the objectives of a research project like TUMULT.

One of the objectives of this project consisted in the investigation of the TBL wall pressure fluctuations with and without pressure gradients. Therefore, to perform this investigation, the experimental techniques hot wire anemometer and microphone antenna were applied. The TBL was investigated under zero, favourable and adverse pressure gradients for 15 and 25 m.s<sup>-1</sup>.

The TBL characterization and the quantification of wall pressure fluctuations with hot wire anemometer and microphone antenna was successfully performed for ZPG, once due to the short period, it was not possible to post-process the data for APG and FPG measured with microphone antenna. The quantification performed allows the improvement of a database with the results for the TBL research under pressure gradients.

It was successfully performed an uncertainty analysis for the hot wire anemometer technique; however, the relation between the different sources of uncertainty should had been done. This was not performed due to the short period. From this analysis, it was concluded that the main source of uncertainty comes from the temperature correction applied to the voltages measured with hot wire anemometer. This temperature correction had to be applied, since during the day the temperature of the laboratory ranged approximately 9 °C, some days even more.

Furthermore, the results obtained with hot wire anemometer were included in a paper, accepted for the proceedings of the AVIATION 2018 Conference that had occur between 25 and 29 of June in Atlanta, with the title “Development of a test rig for the measurement of turbulent boundary layer wall pressure statistics”.

Another experimental technique learned during this internship was PIV. The application of this technique was performed under the supervision of Gian Luca Gori and Simão Nóbrega, a PhD and Research master students, respectively, from VKI. A parametric study for the variables seeding concentration, separation time, Q-Switch delay and aperture was successfully performed. These results allowed the analysis of each parameter, and the choice of the optimum configuration to perform the measurements with PIV for the work of Gori and Nóbrega.

To relate the field of fluid dynamics, and the experience gained at VKI, with the field of environmental engineering, in this report it was also included a literature review, regarding the urban atmospheric boundary layer, in Section 6.

Beside the objectives described previously, during the internship, it was possible to follow three courses lectured at VKI namely: “Introductory course to OpenFoam”, “OpenFoam general programming” and “Large Eddy Simulation – Theory and Applications”.

Doing an internship at VKI, had allow me to develop several skills related with experimental research, but also with numerical applications. Beside this, doing an internship in a foreign country, had allow me to improve language skills, like the English as well as being more sensitive for the French and Dutch. Several soft skills were also acquired.

In conclusion, the objectives established for this internship were successfully achieved, despite some changes that had to be made, when facing some constraints. Finally, doing an internship in a foreign country is something that is advised for other students, once it will provide a great improvement of several skills.

## **Section 7.2 – Recommendations**

Regarding the wall pressure models, it was verified that the Goody model was not compatible with the Rozenberg model, for ZPG. This situation was analysed in this work; however, it needs further investigation, in order to obtain a correct approach with the end of applying in different conditions.

The calculation of the parameter  $C_f$  needs further investigation, to determine how the wall shear stress and shear velocity changes, in order to determine what is the best alternative. In this work it was applied the Bradshaw method.

Since the microphone antenna used is a recent technique at the VKI, its application had allowed the analysis to take a better look to the calibration process and post-processing to perform further improvements for next applications, by my supervisor and advisor from VKI.

## References

- Adamek, K., Vasan, N., Elshaer, A., English, E. and Bitsuamlak, G., 2017. *Pedestrian level wind assessment through city development: A study financial district in Toronto*. Sustainable Cities and Society, Vol. 35, pp. 178-190.
- Amorim, J. H., Valente, J., Cascão, P., Rodrigues, V., Pimental, C., Miranda, A. I. and Borrego, C., 2013a. *Pedestrian Exposure to Air Pollution in Cities: Modeling the Effect of Roadside Trees*. Advances in Meteorology Vol. 2013, 7 pp.
- Amorim, J. H., Rodrigues, V., Tavares, R., Valente, J. and Borrego, C., 2013b. *CFD modeling of the aerodynamic effect of trees on urban air pollution dispersion*. Science of the Total Environment, Vol. 461-462, pp. 541-551.
- Antal, H. I. and Tagadó, T., 2010. *PIV System Synchronization at VKI*. Environmental and Applied Fluid Dynamics department, von Kármán Institute for Fluid Dynamics.
- Anthoine, J., Arts, T., Boerrigter, H. L., Carbonaro, M., Degrez, G., Dénos, R., Fletcher, D., Olivari, D., Riethmuller, M. L., Van den Braembussche, R. A., 2009. *Measurement Techniques in Fluid Dynamics – An Introduction*. von Karman Institute for Fluid Dynamics, 3rd revised edition.
- Arens, E. and Ballanti, D., 1977. *Outdoor Comfort of Pedestrians in Cities*. Environmental Impact Planning Corporation, San Francisco, California.
- Barlow, J. F., 2014. *Progress in observing and modelling the urban boundary layer*. Urban Climate, Vol. 10, pp. 216-240.
- Borrego, C., Valente, J., Carvalho, A., Sá, E., Lopes, M. and Miranda, A.I., 2010. *Contribution of residential wood combustion to PM10 levels in Portugal*. Atmospheric Environment, Vol. 44, pp. 642-651.
- Cermak, J. E., 1973. *Fluid-mechanics applications to problems of wind forces on structures and air-pollution*. Colorado State University, Proceedings of the 13th Midwestern Mechanics Conference: Development in Mechanics, Vol. 7.
- Chevalier, F. and Audoly, C., 2015. *Turbulent Flow-Induced Self Noise and Radiated Noise in Naval Systems – An Industry Point of View*. Flinovia – Flow Induced Noise and Vibration Issues and Aspects, Switzerland.
- EEA, 2017. *Air quality in Europe – 2017 report*. European Environment Agency, Luxembourg.
- Fan, M., Chau, C. K., Chan, E. H. W. and Jia, J., 2017. *A decision support tool for evaluating the air quality and wind comfort induced by different opening configurations for buildings in canyons*. Science of the Total Environment, Vol. 574, pp. 569-582.
- Goody, M., 2002. *An empirical spectral model of surface-pressure fluctuations that includes Reynolds number effects*. AIAA - American Institute of Aeronautics and Astronautics, 8th AIAA/CEAS Aeroacoustics Conference Exhibit, pp. 2565.
- Gori, G. L., 2018. *LIF Temperature field Measurement for Internal Forced Convection Blade Cooling*. Turbomachinery and Propulsion Department, von Karman Institute for Fluid Dynamics.
- Gupta, S. V., 2012. *Measurement uncertainties – Physical parameters and Calibration of Instruments*. Springer, Berlin.

- Juvé, D., Berton, M. and Saize, E., 2015. *Spectral Properties of Wall-Pressure Fluctuations and Their Estimation from Computational Fluid Dynamics*. Flinovia – Flow Induced Noise and Vibration Issues and Aspects, Switzerland.
- Maxit, L., Berton, M., Audoly, C. and Juvé, D., 2015. *Discussion About Different Methods for Introducing the Turbulent Boundary Layer Excitation in Vibroacoustic Models*. Flinovia - Flow Induced Noise and Vibration Issues and Aspects, Switzerland.
- Musker, A. J., 1979. *Explicit expression for the smooth wall velocity distribution in a turbulent boundary layer*. AIAA - American Institute of Aeronautics and Astronautics, Volume 17, pp. 655-657.
- OECD, 2016. *The economic consequences of outdoor air pollution*. Organisation for Economic Co-operation and Development Publishing, Paris.
- Oke, T. R., 2006. *Initial guidance to obtain representative meteorological observations at urban sites*. World Meteorological Organization, Canada.
- Oliveira, L. A. and Lopes, A. G., 2016. *Mecânica dos Fluidos*. Lidl – Edições Técnicas, 5th Edition.
- Özahi, E., Çarpınlioğlu, M. Ö. and Gündoğdu, M. Y., 2010. *Simple methods for low speed calibration of hot-wire anemometers*. Flow Measurement and Instrumentation, Vol. 21, pp. 166-170.
- Pino, D., de Arellano, J. V., Comerón, A., Rocadenbosch, F., 2004. *The boundary layer growth in an urban area*. Science of the Total Environment, Vol. 334-335, pp. 207-213.
- Piomelli, U., 2018. *Large Eddy and Direct Simulation of Turbulent Flows*. Lecture Series 2018-03: Large Eddy Simulation – Theory and Applications. von Karman Institute for Fluid Dynamics.
- Plate, E. J., 1982. *Engineering meteorology – Fundamentals of Meteorology and Their Application to Problems in Environmental and Civil Engineering*. Elsevier Scientific Publishing Company, Amsterdam. Vol. 1.
- Raffel, M., Willert, C., Wereley, S. and Kompenhans, J., 2007. *Particle Image Velocimetry – A Practical Guide*. Springer, 2nd Edition.
- Ricciardelli, F. and Polimeno, S., 2006. *Some characteristics of the wind flow in the lower Urban Boundary Layer*. Journal of Wind Engineering and Industrial Aerodynamics, Vol. 94, pp. 815-832.
- Rozenberg, Y. and Robert, G., 2012. *Wall Pressure Spectral Model Including the Adverse Pressure Gradient Effects*. AIAA - American Institute of Aeronautics and Astronautics, Volume 50, pp. 2168-2179.
- Schram, C., 2003. *Aeroacoustics of subsonic jets: prediction of the sound produced by vortex pairing based on particle image velocimetry*. Eindhoven: Technische Universiteit Eindhoven.
- Schram, C., 2017. *DAP – Data Acquisition and Processing*. von Karman Institute for Fluid Dynamics, Lecture Series.
- Schram, C., 2018. *Turbulent Boundary Layer models – literature review*. von Karman Institute for Fluid Dynamics, Private Communication.
- Schram, C. and Van de Wyer, N., 2018. *An optimized microphone array for the measurement of turbulent boundary layer wall pressure wavenumber-frequency spectra*. Aviation 2018 Conference, Atlanta.

- Sládek, I., Kozel, K., Jaňour, Z. and Gulíková, E., 2004. *On the mathematical and numerical investigation of the atmospheric boundary layer flow with pollution dispersion*. Proceedings of the International Conference on Urban Wind Engineering and Building Aerodynamics – COST Action C14 – Impact of Wind and Storm on City Life and Build Environment, von Karman Institute, Session C.9.
- Stathopoulos, T., 2004. *Wind effects on people*. Proceedings of the International Conference on Urban Wind Engineering and Building Aerodynamics – COST Action C14 – Impact of Wind and Storm on City Life and Build Environment, von Karman Institute, Session B.1.
- Stull, R. B., 1988. *An Introduction to Boundary Layer Meteorology*. Kluwer Academic Publishers, The Netherlands.
- Van de Wyer, N., Zapata, A., Nogueira, D. and Schram, C., 2018. *Development of a test rig for the measurement of turbulent boundary layer wall pressure statistics*. Proceedings of the AVIATION 2018 Conference, 25-29 June, Atlanta.
- VKI, 2016. *Annual Report 2016, 60th anniversary 1956 – 2016*. von Karman Institute for Fluid Dynamics, Belgium.
- Weerasuriya, A. U., Tse, K. T., Zhang, X. and Li, S. W., 2018. *A wind tunnel study of effects of twisted wind flows on the pedestrian-level wind field in an urban environment*. Building and Environment, Vol. 128, pp. 225-235.
- WHO, 2014. *Burden of disease from Ambient Air Pollution for 2012, Summary of results*. World Health Organization, Geneva.
- WHO, 2016. *WHO Expert Consultation: Available evidence for the future update of the WHO Global Air Quality Guidelines (AQGs)*. World Health Organization, Copenhagen.
- Zapata, A., 2017. *Measurement and modelling of turbulent wall pressure in a boundary layer*. Project Report 2017-29, von Karman Institute for Fluid Dynamics, Belgium.
- URL 1: <https://www.vki.ac.be/> (consulted in 01/11/2017).
- URL 2: <https://www.eea.europa.eu/themes/urban/intro> (consulted in 03/02/2018).
- URL 3: <http://www.brighthub.com/multimedia/audio/articles/114495.aspx> (consulted in 06/03/2018).
- URL 4: <http://www.healthdata.org/infographic/global-burden-air-pollution> (consulted in 09/04/2018).



## Appendix I – Uncertainty analysis results

The temperature correction applied in the calibration procedure. Equation 4.6 points out the formula used to correct the voltage measured with hot wire anemometer. To calculate the uncertainty associated with this correction, the Taylor expansion is applied and Equation AI.1 shows the result.

$$\delta E_{corr}^2 = \left( \frac{\partial E_{corr}}{\partial E_{out}} \delta E_{out} \right)^2 + \left( \frac{\partial E_{corr}}{\partial T_w} \delta T_w \right)^2 + \left( \frac{\partial E_{corr}}{\partial T_{out}} \delta T_{out} \right)^2 \quad (\text{AI. 1})$$

The uncertainty associated with the hot wire temperature,  $\delta T_w$ , is calculated applying the Taylor expansion to Equation 4.5. The result follows in Equation AI.2.

$$\delta T_w^2 = \left( \frac{\partial T_w}{\partial E_1} \delta E_1 \right)^2 + \left( \frac{\partial T_w}{\partial E_2} \delta E_2 \right)^2 + \left( \frac{\partial T_w}{\partial T_1} \delta T_1 \right)^2 + \left( \frac{\partial T_w}{\partial T_2} \delta T_2 \right)^2 \quad (\text{AI. 2})$$

The uncertainty associated with the voltage,  $\delta E_i$  is mainly associated with the conversion analog to digital (CAD). This uncertainty is calculated, knowing that the voltage resolution of the CAD is 16 bits cards with a  $\pm 5$  V acquisition card. There is also an uncertainty associated with the LabView programme, but this one was neglected.

Performing all the derivatives, the final form for Equation AI.1 is given by Equation AI.3. The values for  $E_{out}$  and  $T_{out}$  correspond to the voltages and temperatures for 15 and 25 m.s<sup>-1</sup>. Therefore  $\delta E_{corr}^2$  is the uncertainty that corresponds to the voltage correction for the velocities 15 and 25 m.s<sup>-1</sup>.

$$\begin{aligned} \delta E_{corr}^2 [V] = & \left( \sqrt{\frac{T_w - T_{ref}}{T_w - T_{out}}} \delta U_{CAD} \right)^2 + \left[ \frac{E_{out} \left( \frac{1}{T_w - T_{out}} - \frac{T_w - T_{ref}}{(T_w - T_{out})^2} \right)}{2 \sqrt{\frac{T_w - T_{ref}}{T_w - T_{out}}}} \right]^2 \times \\ & \left[ \left( \frac{2 E_2^2 E_1 (T_2 - T_1)}{(E_2^2 - E_1^2)^2} \delta U_{CAD} \right)^2 + \left( \frac{2 E_1^2 E_2 (T_1 - T_2)}{(E_2^2 - E_1^2)^2} \delta U_{CAD} \right)^2 + \left( -\frac{E_2^2}{E_2^2 - E_1^2} \delta T_1 \right)^2 + \right. \\ & \left. \left( -\frac{E_1^2}{E_2^2 - E_1^2} \delta T_2 \right)^2 \right] + \left[ \frac{E_{out} (T_w - T_{ref})}{2 (T_w - T_{out})^2 \sqrt{\frac{T_w - T_{ref}}{T_w - T_{out}}}} \right]^2 \end{aligned} \quad (\text{AI. 3})$$

In Equation AI.3, the values applied for  $T_{out}$  and  $E_{out}$  correspond to the values measured with the hot wire measurements, while the other parameters come from the calibration.

The result obtained from Equation AI.3 is expressed in volts, therefore it is necessary to convert this one to  $m.s^{-1}$ . To perform this, Equation AI.4 is applied.

$$\delta E_{corr}^2 \left[ \frac{m}{s} \right] = \left( \frac{du}{dV} \right)^2 \delta E_{corr}^2 [V] \quad (AI. 4)$$

where  $\frac{du}{dV}$  is the derivative of the 4<sup>th</sup> order polynomial that was applied in the calibration of the hot wire anemometer.

The uncertainty associated with the velocity measured by the hot wire anemometer can have two main sources:

- The systematic uncertainty,  $\delta u_{jet}$ , coming from the calibration of the hot wire anemometer;
- The random uncertainty,  $\delta u_{HW,rand}$ , coming from the number of samples acquired.

The total uncertainty for the velocity measured,  $\delta u_{tot}$  can be written as it is expressed on Equation AI.5.

$$\delta u_{tot}^2 = \delta u_{jet}^2 + \delta u_{HW,rand}^2 \quad (AI. 5)$$

The random uncertainty can be neglected, once the number of samples was high.

As mentioned in Section 4, it was considered that the total pressure in the settling chamber is equal to the static pressure,  $p_s$ , where the static pressure is about 99,3% of the total pressure. Therefore, the jet velocity can be calculated using Equation AI.6.

$$u_{jet} = \sqrt{\frac{2p_s R_s T_\infty}{p_\infty}} \quad (AI. 6)$$

where,  $R_s$  is the specific gas constant,  $T_\infty$  and  $p_\infty$  are the ambient temperature and pressure, respectively.

Applying the Taylor expansion, the uncertainty for the velocity of the jet on the calibration nozzle is expressed as (Equation AI.7):

$$\delta u_{jet}^2 = \left( \frac{\partial u_{jet}}{\partial p_s} \delta p_s \right)^2 + \left( \frac{\partial u_{jet}}{\partial T_\infty} \delta T_\infty \right)^2 + \left( \frac{\partial u_{jet}}{\partial p_\infty} \delta p_\infty \right)^2 \quad (\text{AI. 7})$$

Knowing that the water manometer used to calibrate the pressure transducers have 0.05 mmH<sub>2</sub>O precision, the static pressure can be rewritten as a function of mmH<sub>2</sub>O,  $h_w$ , and the relation between the pressure and voltage is linear (Equation AI.8), where  $a_1$  and  $a_2$  are the coefficients obtained for a linear regression,  $\rho_w$  is the water density and  $g$  the Earth's gravitational acceleration.

$$p_s = h_w \rho_w g = a_1 E + a_2 \quad (\text{AI. 8})$$

The uncertainty associated with the static pressure is related with the CAD and the calibration (systematic uncertainty). Applying the Taylor expansion to Equation AI.9, the following equation is obtained.

$$\delta p_s^2 = \left( \frac{\partial p_s}{\partial E} \delta E \right)^2 + \left( \frac{\partial p_s}{\partial a_1} \delta a_1 \right)^2 + \left( \frac{\partial p_s}{\partial a_2} \delta a_2 \right)^2 \quad (\text{AI. 9})$$

The uncertainty associated with  $a_1$  is related with the linear fit, therefore  $\delta a_1 = \sigma_E$ . Reorganizing equation AI.7, the uncertainty for  $a_2$  can be calculated using Equation AI.10.

$$\delta a_2^2 = \left( \frac{\partial a_2}{\partial h_w} \delta h_w \right)^2 - \left( \frac{\partial a_2}{\partial a_1} \delta a_1 \right)^2 + \left( \frac{\partial a_2}{\partial E} \delta E \right)^2 = (\delta h_w \rho_w g)^2 \quad (\text{AI. 10})$$

Now that all the variables are defined, the final form to calculate the systematic uncertainty coming from the hot wire anemometer calibration is given by Equation AI.11.

$$\delta u_{tot}^2 = \delta u_{jet}^2 = \frac{R_s T_\infty}{2 p_\infty p_s} (\rho_w g \delta h_w)^2 + \frac{R_s p_s}{2 p_\infty T_\infty} \delta T_\infty^2 + \frac{p_s R_s T_\infty}{p_\infty^3} \delta p_\infty^2 \quad (\text{AI. 11})$$

In Equation AI.11, the values applied come from the calibration points. Now, this uncertainty associated to the velocities ranging from 0 m.s<sup>-1</sup> until 30 m.s<sup>-1</sup> from the calibration need to be applied to the measurement points. To do this, a 4<sup>th</sup> order polynomial was calculated with the velocity uncertainty as a function of the calibration velocity  $\delta u_{tot} = f(u_{cal})$ .

After obtaining this relation, the polynomial is applied to the velocities from the measurements, obtaining the uncertainty associated with the calibration for each measured point.

In Table AI.1, the uncertainties variables and other constants used in the Equations above can be observed.

**Table AI. 1** - Uncertainties and other constants.

<b>Variable</b>	<b>Value</b>
$\delta h_w$	$5 \cdot 10^{-5} \text{ m}$
$\delta T_\infty,$ $\delta T_1,$ $\delta T_2$	0.1 K
$\delta p_\infty$	10 Pa
$\delta E_i = \delta U_{CAD}$	$1.53 \cdot 10^{-4} \text{ V}$
$T_{ref}$	289.15 K
$R_s$	$287 \text{ J} \cdot \text{kg}^{-1} \cdot \text{K}^{-1}$

It follows the results of uncertainty for the velocity profiles for the other pressure gradients analysed in this report.

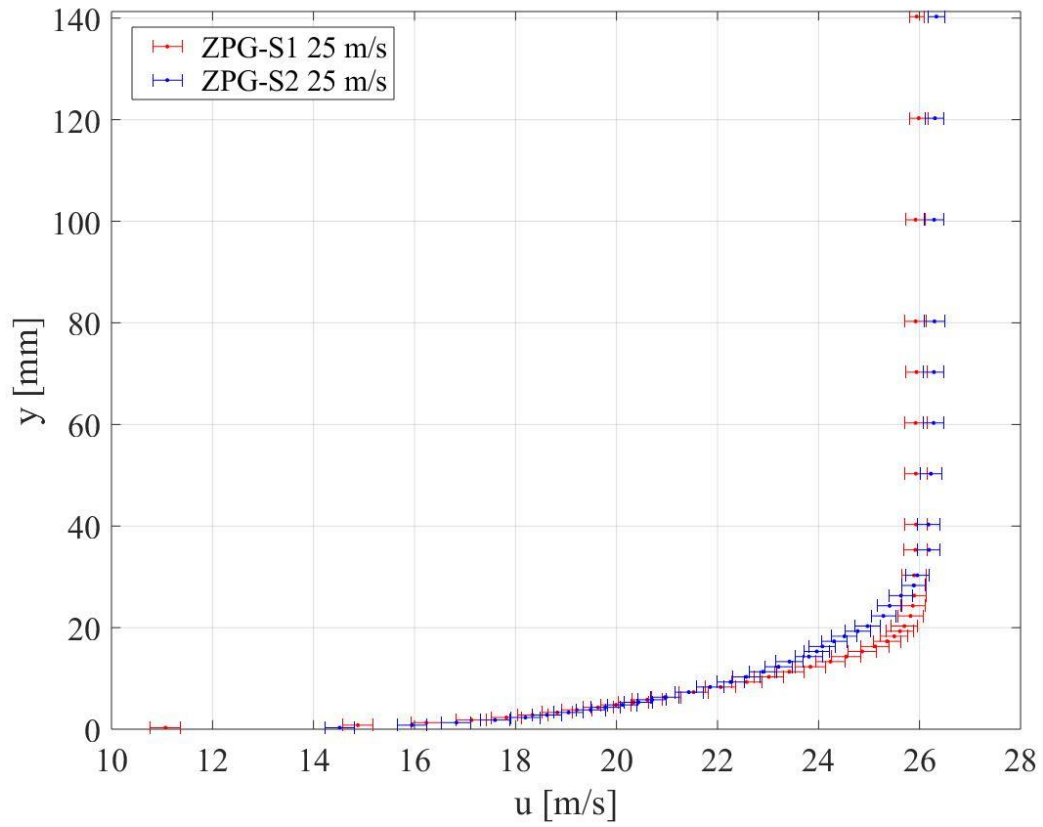


**Figure AI. 1** - Velocity profiles for  $25 \text{ m}\cdot\text{s}^{-1}$  for ZPG at the Station 1 and 2 respectively, including the estimated uncertainty.

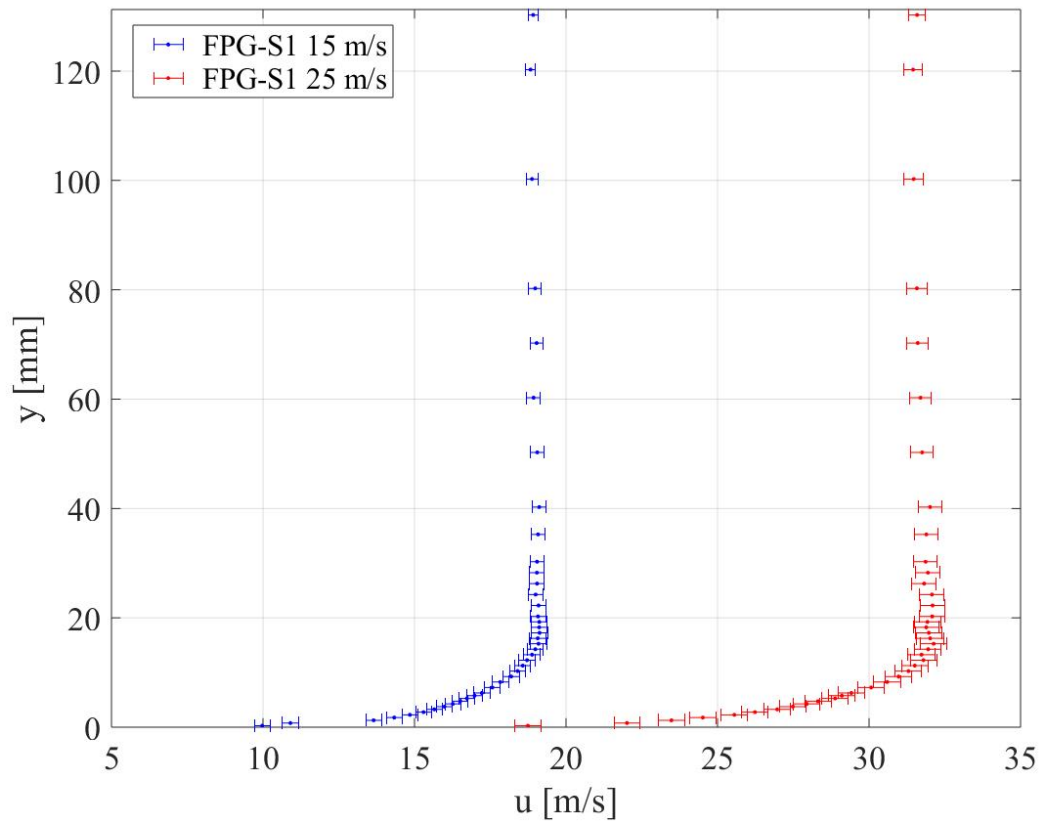


**Figure AI. 2** - Velocity profiles for 15 and 25 m.s<sup>-1</sup> for FPG at Station 1, including the estimated uncertainty.

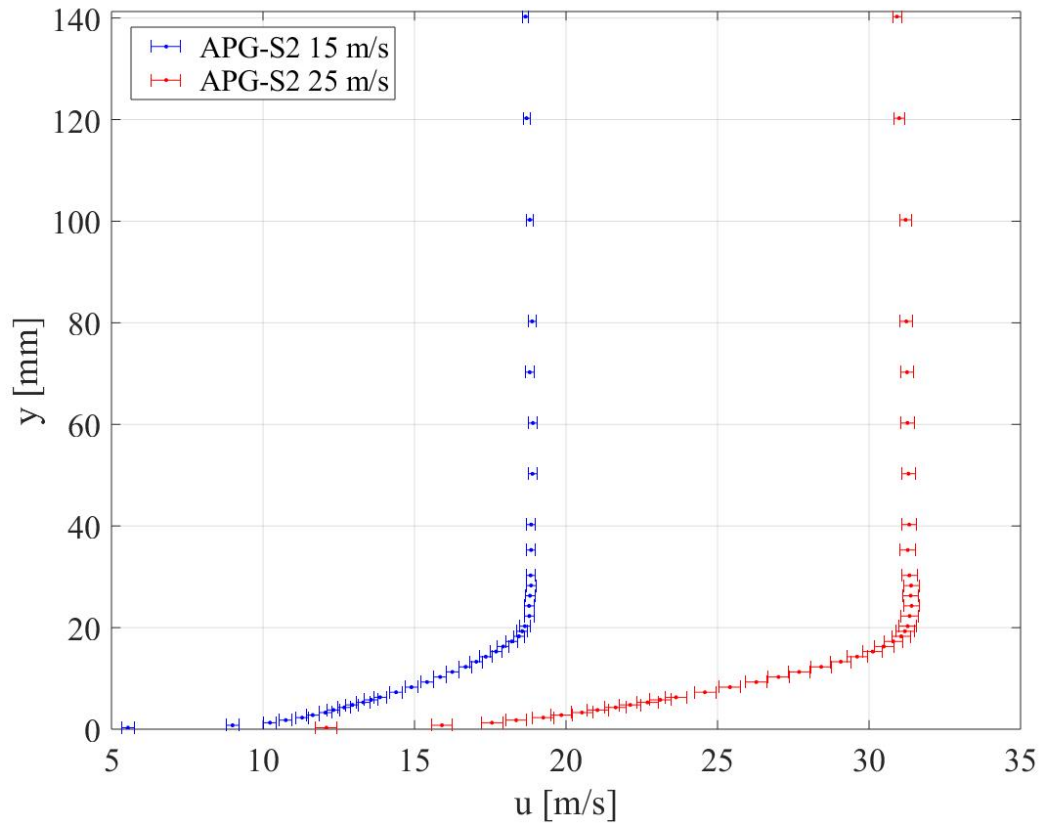


**Figure AI. 3** - Velocity profiles for 15 and 25  $\text{m}\cdot\text{s}^{-1}$  for APG at station 2, including the estimated uncertainty.

## Appendix II – PIV system synchronization

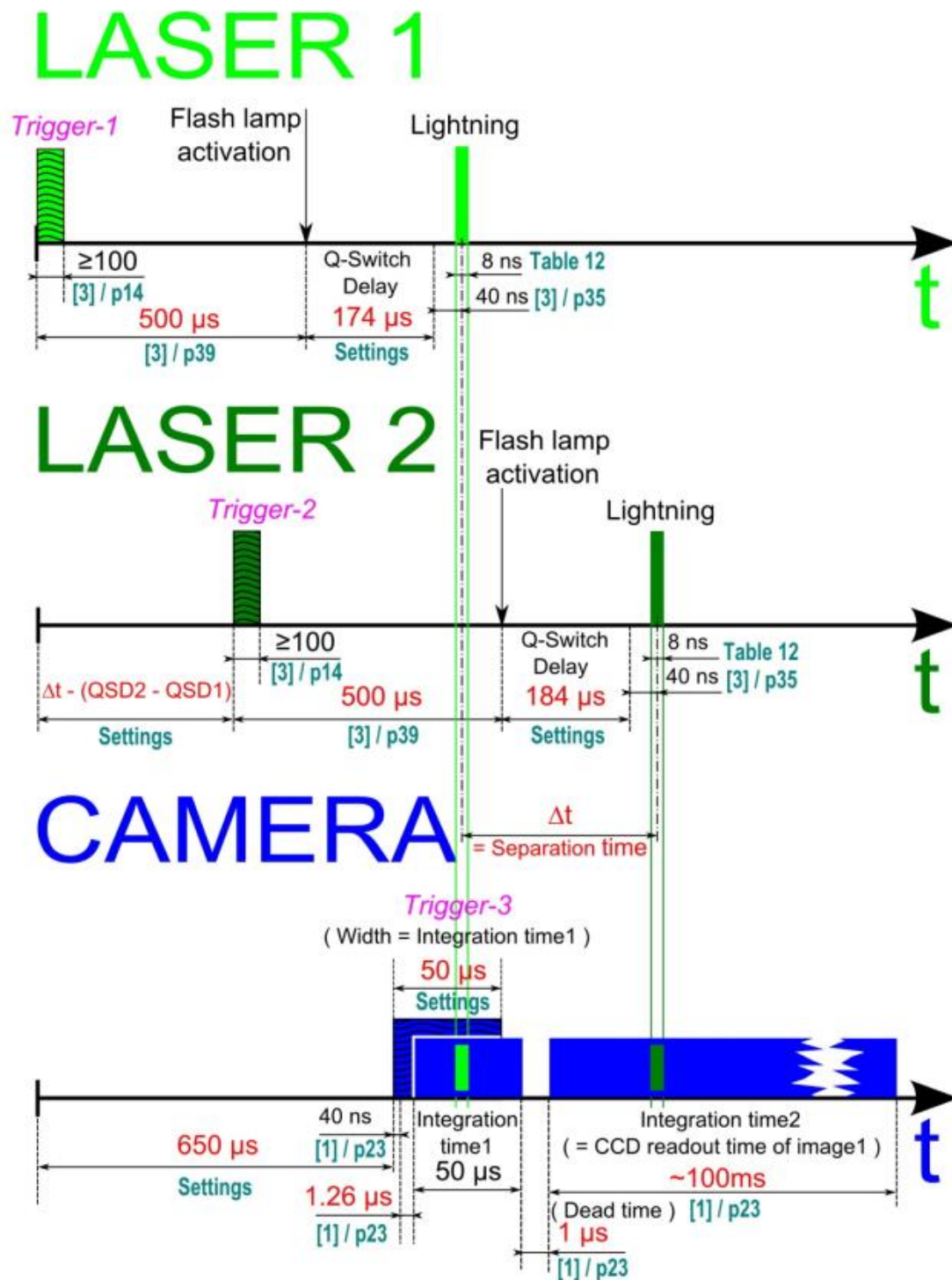


Figure AII. 1 - Timing diagram for the PIV synchronization (Antal and Tagadó, 2010).



## Appendix III – Effect of temperature correction

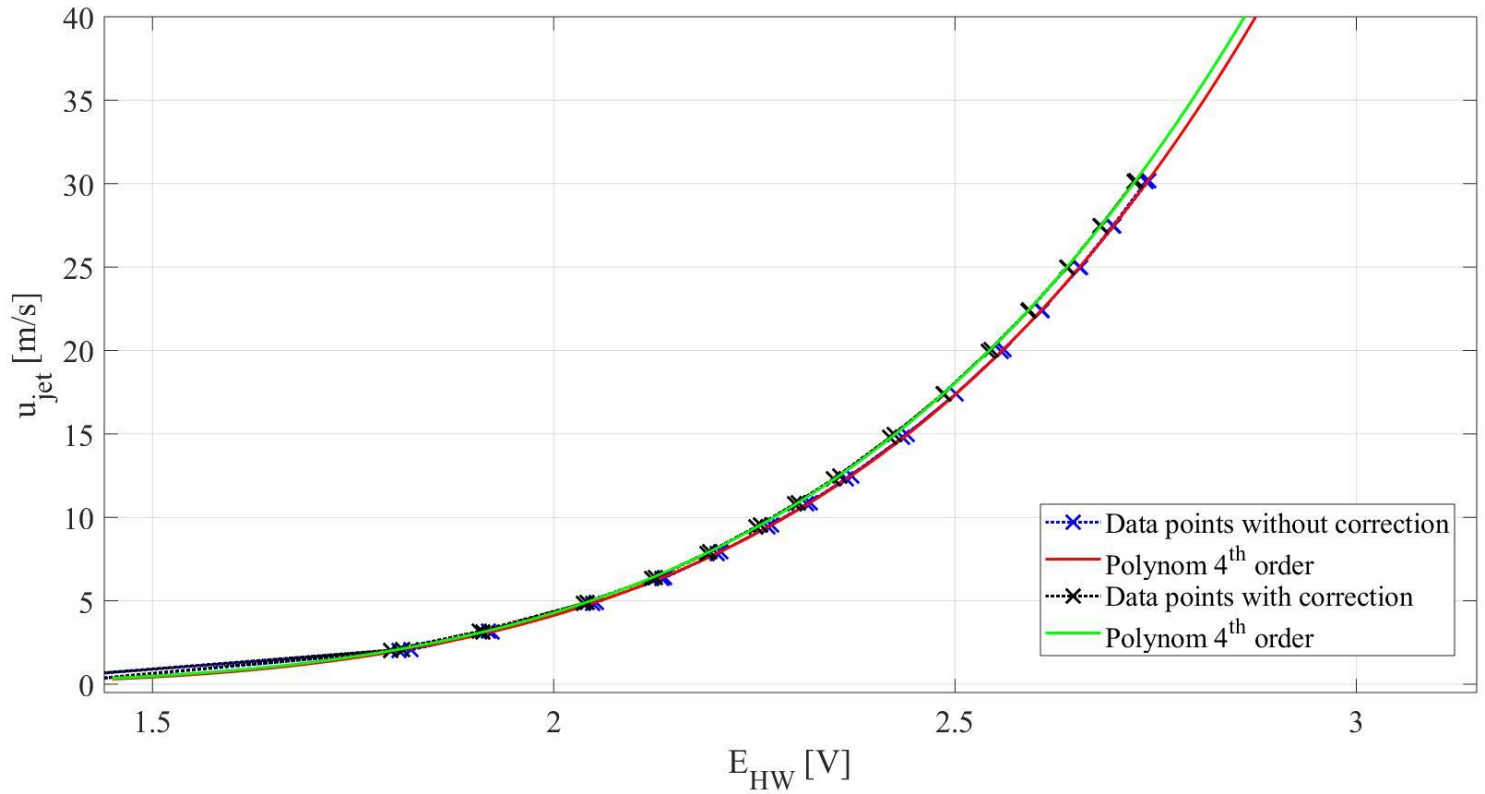


Figure AIII. 1 - Effect of the temperature correction applied to the measured data with hot wire anemometer.